# High Energy Density Physics with Intense Ion and Laser Beams

Annual Report 2003

July 2004

Coordination and editorial works:  Karin Weyrich (GSI Darmstadt)

## Editorial

Intense heavy ion beams and lasers and pulsed power devices are the research tools, which are most commonly used to achieve high energy density states in matter. This report covers the progress of the field in 2003. Since over 20 years the international community of high energy density physics takes the opportunity to meet very early in the year in the Austrian alpine village of Hirschegg to discuss the results and the progress. The emphasis of this meeting has shifted from inertial fusion and inertial fusion driver issues to basic physics problems of high energy density matter. This transition is also reflected and documented in the annual issues of this report. Lasers now play a key role in the generation and diagnostic of warm dense matter and high energy density states. Laser plasmas from ultra intense laser radiation has also turned out to be a powerful source of intense particle beams from electrons to protons and even heavy ions. The new PHELIX laser system is also intended to be a tool to study the properties of intense laser plasma generated particle beams. The laser program at GSI has reached a couple of milestones last year, since all the components of the LLNL Nova laser which were shipped to GSI were integrated into the system, and the commissioning of the 2-pass main amplifier was started. Moreover a first experiment was successfully carried out. In this experiment a transient, collisionally excited x-ray laser in Ni-like zirconium was demonstrated at a wavelength of 22 nm.

For many years GSI was the only accelerator laboratory in Germany that was engaged in plasma physics and high energy density physics. Meanwhile DESY at Hamburg, with the VUV-FEL user facility also entered this field. The high intensity short wavelength radiation of this facility is able to generate small samples of matter and to achieve high matter temperature and extreme pressure on a very short time scale. Thus intense heavy ion beams and intense short wavelength photons are excellent tools for high energy density physics and they complement each other. The VUV-FEL facility is described in one contribution of this report. The community is ready to use heavy ion beams, laser beams and the VUV-FEL for their research projects and the whole field will certainly benefit from the diversity of intense radiation sources that are available.

The future accelerator facilities project at GSI, which is now called FAIR (**F**acility for **A**ntiproton and **I**on **R**esearch), also was a focus point for the activities in 2003. In October a workshop was held at GSI to discuss the future physics program at FAIR, and a large scientific community demonstrated their interest in high energy density physics with the intense heavy ion beams provided by the new accelerator facility. The plasma physics contribution to this workshop is summarized in a short chapter with three contributions.

GSI is charged to keep in touch with the development of inertial fusion activities worldwide. In the framework of these activities GSI scientists participated in the Inertial Fusion Science and Applications conference held 2003 in Monterey and they send a representative to participate in the IAEA coordinated research program on elements of power plant design for inertial fusion in Vienna.

I want to thank all colleagues for submitting their contributions, which gives us the opportunity to demonstrate the widespread interest in this research field.

Darmstadt, July 2004 Dieter H.H. Hoffmann

# Contents

# 1 THE PLASMA PHYSICS EXPERIMENTAL PROGRAM

## 1.1 Laser Plasma Physics

## 1.2 Plasma Spectroscopy

## 1.3 Beam Interaction Experiments

## 1.4 Atomic and Radiation Physics

## 1.5 Pulsed Power Applications

# Status of PHELIX Laser Program

S. Borneis[1], R. Bock[1], E. Brambrink[1, 2], H. Brand[1], C. Bruske[1], J. Caird[3], R. Fuchs[1], E. W. Gaul[1], W. Geithner[1], S. Götte[1], C. Häfner[1], T. Hahn[1], W. Heddrich[4], H. M. Heuck[1,5], D.H.H. Hoffmann[1,2], D. Javorkova[1], H. - J. Kluge[1], Th. Kühl[1], S. Kunzer[4], R. Lotz[1], T. Merz[1,2], P. Neumayer[1], D. Reemts[1], M. Roth[1,2], S. Samek[6], G. Schaumann[1,2], F. Schrader[1], W. Seelig[2], C. Spielmann[7], R. Stenner[1] A. Tauschwitz[1], R. Thiel[1], D. Ursescu[1], P. Wiewior[7], U. Wittrock[5]

[1]GSI Darmstadt, Germany; [2]Technische Universität Darmstadt, Germany; [3]Lawrence Livermore National Laboratory, USA; [4]Fachhochschule Darmstadt, Germany; [5]Fachhochschule Münster, Germany; [6]Jagiellonian University, Krakow, Poland; [7]Julius Maximilian Universität Würzburg, Germany

One of the most important milestones of the PHELIX laser program was reached in January 2003, when the required Nova laser components from Lawrence Livermore National Laboratory (LLNL) arrived at GSI. The basis for the transfer was the agreement between the Department of Energy of the United States of America (DOE) and the Federal Ministry of Education and Research of the Federal Republic of Germany (BMBF) to cooperate in energy research, science and technology and development. Within the agreement which was signed on February 20, 1998 the basic science of dense plasma physics using intense ion and laser beams will be explored.

Fig. 1 shows photos of the dismantling and shipping in LLNL and the arrival of the components at GSI.

*Figure 1: Transfer of Nova components from LLNL to GSI.*

About two thirds of the equipment from LLNL consisted of pulsed power components. Since these parts had been stored in Livermore under open sky for years they required extensive cleaning and refurbishment. Especially the 12 racks containing the ignitron switches had to be totally rebuilt. At the end of 2003 the capacitor bank including the ignitron switches, power supplies and dump system for the double pass amplifier and the booster amplifier were installed and the section required for the double pass was tested successfully using internal dummy loads instead of the flash lamps of the amplifiers. To ensure protection of the high voltage power supplies from possible transients in the discharge circuit we developed mechanical high voltage switches which disconnect the power supply from the capacitor bank after the completion of the charging cycle and which will also be used to distribute the PILC pulse (Pulsed Ionization Lamp Check). Thirty of these switches were manufactured in house and are now in routine operation. In addition all high voltage connections between the capacitors, high current switches and amplifiers were installed. This allowed the testing of a total number of 100 flash lamps required for the double pass amplifier. These tests were performed in the clean room 10,000 environment of the laser bay before they were installed in the refurbished Nova amplifier housings. For the capacitor and flash lamp tests the discharge currents of the ten circuits that are connected to one amplifier were monitored in parallel. For these tests a new PXI digitizer system with 60 differential channels was set up which will be part of the final PHELIX shot monitoring system. The pulsed power capacitor room and its installations are shown in Fig. 2 together with an inset of the view of the controls console.

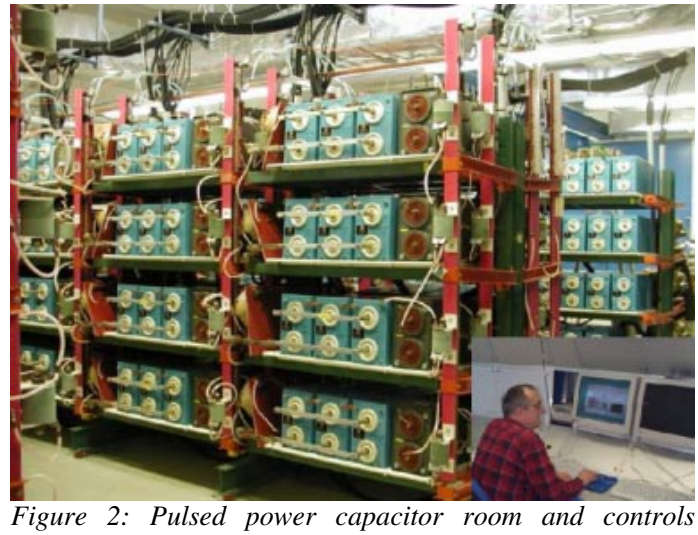

*Figure 2: Pulsed power capacitor room and controls console*

The high amount of stored electrical energy and the related safety hazard as well as the high capital investment of the laser subsystems translate into demanding primary requirements for the PHELIX Control System (PCS). The powerful framework of the PCS was developed by the ECOS group of GSI [1].The application layer of the PCS will provide the safe operation of a high-energy shot of PHELIX which requires the remote control and supervision of a large number of devices and subsystems. In 2003 the design development of the PCS was started and allowed us to replace the preliminary manual mode of operation that was used for the first test experiments of the pulsed power of the Nova amplifiers.

In preparation of the commissioning of the 2-pass main amplifier, which is planned for 2004, the PHELIX engineering team disassembled the opto-mechanical Nova and pre-amplifier hardware, cleaned it and verified the cleanliness level of a clean room 100 environment prior to

reassembly. The 2-pass amplifier consists of a total of five 31.5 cm diameter disk amplifiers; four of them are equipped with laser glass and fully operational. The beam line of the folded 2-pass amplifier including the 90- degree turning mirrors and their housing are fully sealed and are flushed with nitrogen to avoid degradation of the optics. The alignment of the laser chain was carried out with the help of a 10 W cw Nd:YLF alignment laser. Fig. 3 is a photo of the aligned and sealed 2-pass amplifier.

*Figure 3: PHELIX 2-pass amplifier section. The beam line is sealed and flushed with nitrogen*

To transport the beam to the experimental areas the design and drawings for the Z6 beam line were started in 2003 and were 90% completed. The set-up of the hardware is in progress. All required components are ordered, most of them are already delivered. Completions of the electric installations, re-building of the ion beam line are additional significant milestones on our road to the first PHELIX experiments at Z6.

An important step towards first laser experiments with PHELIX was the commissioning of the pre-amplifier [2], recompression of amplified pulses to a power level of well above 10 TeraWatt and its successful application as a pump source for a transient collisionally excited x-ray laser [3]. The architecture of the pre-amplifier, shown in fig. 4, follows the design of the Livermore PW front-end [4]. The pre-amplifier provides pulses of up to 8 J, if the stretched fs-front-end beam is amplified. The integration of the system into the final control system and the completion of the engineering effort to further improve the stability and reliability of the system is planned for 2004.

Important for reaching with PHELIX high power densities of the order of $10^{21}$ W/cm$^2$ the improvement of the wave front quality of the laser beam is of crucial importance. As a first step towards the improvement of the beam quality we have integrated a first closed loop adaptive optics system at the end of the pre-amplifier. The system was purchased from the Laboratory of Adaptive Optics of the Russian Academy of Sciences [5]. The concept is described in more detail in a separate contribution in this report [6]. In addition to the anticipated increase of the repetition rate of the pre-amplifier the main goal is the pre-compensation of the aberrations of the main amplifier. In addition to the actively deformable bimorph mirror we have laid out the 0-degree mirror of the 2-pass main amplifier as a static wave front corrector. The concept of introducing a controlled amount of aberrations on a mirror that will cancel the aberrations of the laser chain by deforming a standard mirror with micrometers was successfully demonstrated in Rutherford at the Vulcan laser [7].

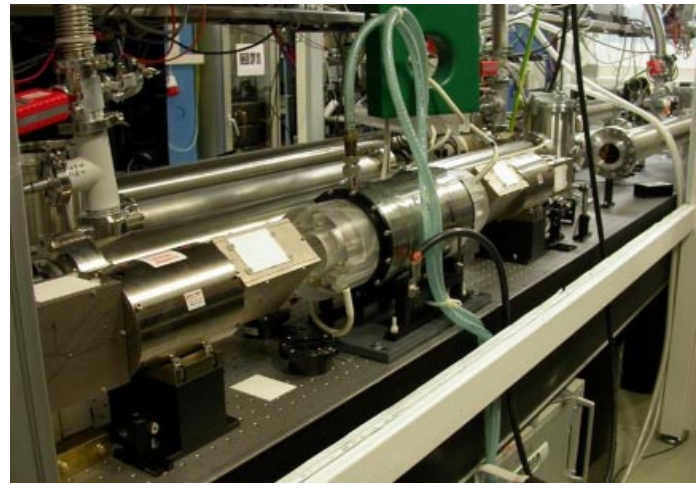

*Figure 4: View of pre-amplifier of the 45 mm diameter rod amplifier which was designed and built by LLNL*

For the final recompression of the high-energy pulse the main technical challenge is the damage threshold of the compression gratings. The emerging technology of multi-layer dielectric (MLD) gratings offers a significant improvement as compared to gold coated gratings. The large aperture compression gratings had been expected by the end of the year, however delivery was delayed due to recent advancements in the technology. The delivery is expected towards autumn 2004.

The MLD grating based Petawatt compressor necessitates a new pulse stretcher using the same groove density as the compressor gratings. The ray trace modelling of the new stretcher was performed and the grating already delivered. The design goal is to stretch pulses by 250 ps/nm and a transmitted bandwidth of 16 nm.

For the characterization of the fs-pulses an experimental setup was built to perform SPIDER (Spectral Phase Interferometry for Direct Electric field Reconstruction) [8]. This technique allows to obtain full information of a short pulse laser and therefore to unambiguously recover the temporal pulse shape. It will be an important tool for the optimisation of the chirped pulse amplification system.

## References

[1] D. Beck et al.: to be published in Nucl. Instr. Meth. A

[2] C. Häfner, PhD thesis, University of Heidelberg, Germany (2003)

[3] P. Neumayer, PhD thesis, TU Darmstadt, Germany (2003)

[4] B. C. Stuart et al.: Opt. Lett., vol. 22 (4), 242-244, 1997

[5] http://www.laser.ru/adopt/home.htm

[6] H. M. Heuck et al.: this report

[7] Annual report Central Laser Facility 1997/1998, p. 153

[8] S. Kunzer, diploma thesis, FH Darmstadt, Germany (2003)

# Beam diagnostics and adaptive optics for PHELIX

H.-M. Heuck[1], S. Borneis[2], E. Gaul[2], C. Häfner[2], A. Kudriaschow[4], T. Kühl[2], P. Wiewior [3], and U.Wittrock[1]

[1]University of Applied Science Münster, Stegerwaldstr. 39, 48565 Steinfurt, Germany
[2]Gesellschaft für Schwerionenforschung mbH, Planckstr. 1, 64291 Darmstadt, Germany
[3]Julius Maximilian Universität, Am Hubland, 90074 Würzburg, Germay
[4]Russian Academie of Sciences, Svyatoozerskaya Str. 1, Shatura, 140700 Russia

PHELIX (Petawatt High Energy Laser for Heavy Ion Experiments) is designed to be a versatile laser capable of supplying a few Kilojoule, ns pulses as well as Petawatt level, fs pulses to the experiments. To achieve a focal spot size close to the diffraction limit it is required to optimize the beam quality of PHELIX. Spatial wave front aberrations increase the spot diameter in the focal plane. In addition they result in undesired optical path differences of the laser beam within the grating compressor, which lead to an increased pulse duration [1] and thus lower peak power.

The NOVA amplifiers exhibit mainly three different types of wave front aberrations: static aberrations, pump shot aberrations and long term thermal aberrations. The main purpose of the adaptive optics system is to correct for the thermo-optical aberrations in the main amplifier, in order to maintain the beam quality for the next shot without having to wait close to 10 hours as required for a complete return to the initial conditions.

The adaptive optics system comprises an actively controlled bimorph adaptive mirror and a static deformable HR-mirror in the main amplifier. The bimorph adaptive mirror consists of a dielectric coated glass substrate that is attached with its backside to a stack of two piezo discs. The piezo discs themselves are coated with 31 electrodes. In addition to the actively controlled bimorph mirror in the pre-amplifier, the retro reflecting mirror of the double pass amplifier can be deformed by four micrometer screws. This will allow the correction of astigmatism which is expected to be the major aberration with the disc amplifiers. This concept was successfully demonstrated at the VULCAN laser in the Rutherford Appleton Laboratory.

The bimorph mirror is placed in the relay image plane of the laser rods and represents the object plane for the transport telescopes of the double pass section in the main amplifier. The maximum achievable deformation of this mirror is about 6 $\lambda$. This allows the mirror to correct the aberrations that arise in the pre-amplifier and, in the near future, to pre-correct for aberrations in the main amplifier. Behind a leaky mirror at the end of the pre-amplifier a Shack-Hartmann wave front sensor is installed. With this wave front sensor and an automatic control program, a closed loop operation for the pre amplifier is realized.After the calibration of the close-loop adaptive mirror setup, we successfully demonstrated the optimization of the pre-amplifier. The laser was fired two times with a delay of five minutes between each shot to introduce thermal aberrations into the amplifier. During the second shot the wave front was measured and inverse surface of the adaptive mirror was calculated. Figure 1 shows the optical path difference over the entire surface for the adaptively controlled amplifier and for the free running system. The correction system proofed to be capable of improving the Strehl ratio by a factor of three. Here, as expected for the rod amplifier, the major part of the thermal aberrations is in the defocus term. To measure beam properties in the double pass amplifier, a middle-of-chain sensor is installed behind the retro reflecting mirror and in addition an end-of-chain sensor will be installed at the exit of the amplifier. A telescope corrected for spherical aberrations is used for down collimating the beam in both sensors in a way. The reduced beam is guided to a near and far field measurement and a Shack-Hartman sensor. For pre-correction of aberrations of the disc amplifier with the actively controlled adaptive mirror this Shack-Hartmann sensor can be used to close the control loop. The expected aberrations are in the magnitude of a few waves and appear mostly in the astigmatism term. With the actively controlled adaptive mirror and the static deformable mirror it should be possible to increase the repetition rate dramatically and concurrently increase the brightness.

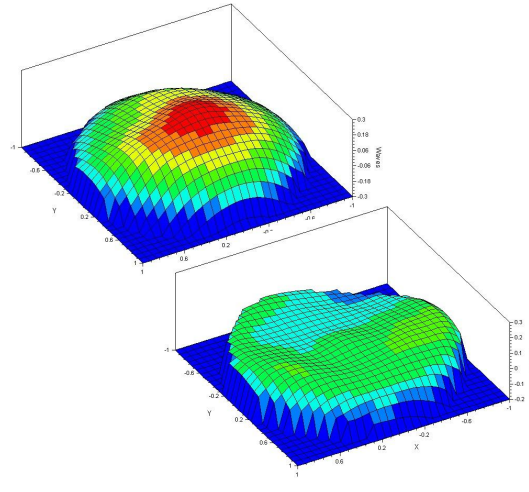

Figure 1: Wave front of a fs-pulse amplified with the pre-amplifier without (top) and with (bottom) the closed loop adaptive correction.

## References

[1] H.-M. Heuck, C. Häfner, P. Wiewior, E. Gaul, S. Borneis, T. Kühl, and U. Wittrock, *Waverfront measurement and adaptive optics at the phelix laser*, Proceedings of the 4th International Workshop on Adaptive Optics for Industry and Medicine, 2003.

# Development of a resistive target heating system for laser-acceleration of heavy ions

E. Brambrink[1], P. Audebert[2], A. Blazevic[1], T.E. Cowan[3], J. Fuchs[3], M. Geißel[1], M. Hegelich[4], S.Karsch[5], H. Ruhl[3], T. Schlegel[1], J. Schreiber[6] and M. Roth[1]

[1]Darmstadt University of Technology, Germany; [2]LULI, Paliseau, France; [3] University of Reno, USA; [4] LANL, USA; [5]RAL, Didcot, Great Britain; [6]MPQ Garching, Germany

The acceleration of ions with ultra-intense lasers is a fast developing research field of the recent years. Especially the generation of intense, high quality beams with energies up to 60 MeV has a wide range of applications due to the unique beam properties, such as radiography and isochoric heating. These protons are generated in a process which is called Target Normal Sheath Acceleration (TNSA) [1]. Hot electrons, which are produced in the relativistic laser plasma interaction, propagate through the target. When the first electrons reach the rear side and escape, the remaining positive charge leads to an electrostatic field, which confines the other electrons. In this electron sheath a high electrostatic field in the order of $10^{12}$ V/m is created, which immediately ionises the atoms due to field ionisation. Normally, there are impurities on the target surface, such as water or oil, which contain hydrogen and other atoms beside the target material. The ions and protons are accelerated in the electric field, where protons are accelerated the most due to their charge over mass ratio. As the protons are running in front of the other ions species, they are shielding the electric field from these ions. Therefore, independent of the target material, one always gets energetic protons and less energetic ions.

For the acceleration of heavy ions it is necessary to remove the hydrogen containing contaminations on the target surface. In this case it is possible to get energetic ions. This has been proven for light ions, such as flourine and carbon. Thereby energies up to 5 MeV/u have been measured [2]. The acceleration of heavy ions is not only important for practical applications, it gives also information about the strength of the accelerating field, as the appearance or absence of a charge state gives limits for the electric field.

For reproducible acceleration of heavy ions and well defined experimental conditions it is important to remove the hydrogen reliably. One possibility, which reaches this conditions is the resistive heating of the target to more than 1000°C for several minutes. All hydrogen containing materials either evaporate at this temperature or crack up. A critical issue of the heating system and the targets is, that they have to survive these high temperatures for a certain time without evaporating the bulk material into vacuum chamber.

To realize such a target heating system thin tungsten targets, which are coated with thin layers of other material, such as carbon or $CaF_2$, are used. Of course, this material has to have a melting point, which is high enough to survive the heating.

The tungsten target itself is a strip with a typical thickness of 10µm-50µm and a width of 1 mm. This strip then is clamped with the electrical connectors onto an insulator plate.

To prevent the evaporation of material during the heating of the target, we used only ceramics as insulator, stainless steel and copper. No part of the device is glued. The cables, which deliver the current to the target, have to be without insulation on the last centimeters.

The target is heated typically with around 20 W, which leads to a bright white glowing target. Due to the low resistitance of the target a current of 10-20 A is necessary. To remove the hydrogen a heating time of 3 minutes is sufficient. If required by the experimental conditions the heating time can be much longer. Times of two hours without destruction or failures of the system have been demonstrated.

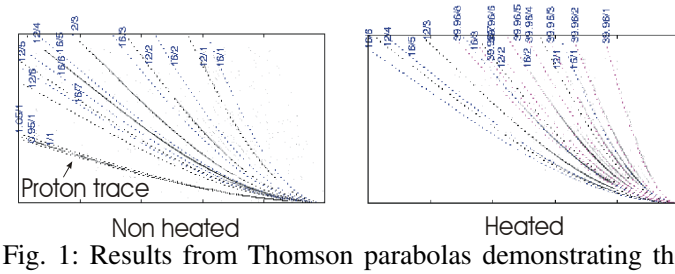


Fig. 1: Results from Thomson parabolas demonstrating the successful removing of the protons

The elimination of the hydrogen by the heating system is very efficient. Fig. 1 shows the traces of different ion species in the Thomson parabola for a heated and an unheated target. With heating no protons can be seen in the figure 1. Instead the intensities and energies of the heavier ions are increased significantly.

On addition to the removal of the hydrogen it is also planned to eliminate other impurities like oxygen and carbon, which can not be evaporated due to their high melting point. In this case a laser of low intensity is used to ablate these materials from the surface directly before (some µs) the experiment.

For applications it will be necessary to run the heating system at a high repetition rate as this lasers will work with a continuous target which is moving at a high speed. Target heating in the described way is not possible for this setup. In this case heating with microwaves is proposed, which could heat the target without electric connectors.

## References

[1] S. C. Wilks et al., *Phys. Plasma* **8**,542 (2001)

[2] M. Hegelich et al., *Phys. Rev. Lett.*, **89**, 085002 (2002)

# SPIDER diagnostic for short pulse characterization at PHELIX

S. Kunzer[1], E. W. Gaul[2], W. Heddrich[1], Th. Kühl[2], P. Neumayer[2], C. Spielmann[3], P. Wiewior[2,3]

[1]FH Darmstadt, Schöfferstr. 3, 64295 Darmstadt, Germany; [2]Gesellschaft für Schwerionenforschung mbH, Planckstr.1, 64291 Darmstadt, Germany; [3]Julius Maximilian Universität, Würzburg, Am Hubland, 97074 Würzburg, Germany

To reach laser powers at the Petawatt level at PHELIX the technique of chirped pulse amplification (CPA) is used, where an originally short laser pulse is stretched in time by over several orders of magnitude and is recompressed close to its original duration after amplification. This requires a reliable diagnostics of the recompressed ultra-short pulse.

The SPIDER (Spectral Phase Interferometry for Direct Electric field Reconstuction) [1] is one of the techniques capable to provide the full information on an ultra-short laser pulse. In contrast, standard autocorrelation techniques can give the temporal pulse duration only, and under the assumption of the temporal pulse shape.

SPIDER is a self referencing variant of spectral interferometry, where the ultra-short pulse interferes spectrally with its own, delayed in time replica. The resulting interference pattern is measured by a spectrometer. By shifting the center frequency $\omega_0$ of one of the two pulses by an amount $\delta\Omega$, information of the spectral phase is encoded in fringe shifts and can be recovered by a direct non-iterative (inversion) numerical algorithm. Shifting the center frequency is achieved by frequency mixing with a third pulse which is linearly chirped in time. This way the two pulses are up-converted with two different frequencies. The chirped pulse can be obtained by sending a portion of the original pulse through a compact stretcher.

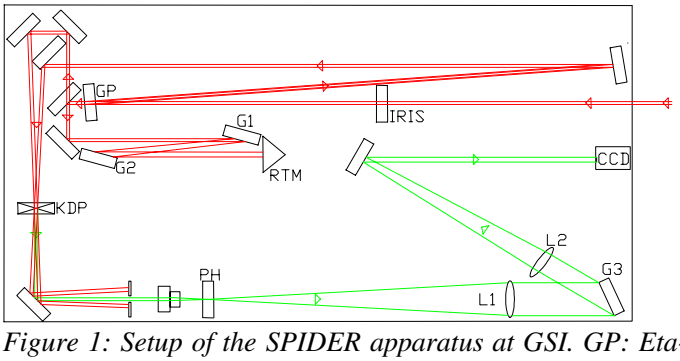


*Figure 1: Setup of the SPIDER apparatus at GSI. GP: Etalon, G1,2: stretcher gratings, RTM: roof top mirror, G3: spectrometer grating, KDP: non-linear crystal, PH: pinhole,L1,L2: lenses, CCD: camera*

The CPA pulses from the PHELIX laser ($\lambda = 1054$ nm) exhibit a bandwidth $\Delta\lambda$ between 4 nm and 7 nm, depending on the pulse energy. Upon recompression this corresponds to pulse durations of 400 fs to 300 fs. For these kind of pulses the parameters for the SPIDER were chosen to $\tau = 20$ ps and $\delta\Omega = 9\times10^{-4}$ fs$^{-1}$.

The PHELIX SPIDER set-up is shown in Fig. 1. Two pulses are generated by reflection off the two sides of an uncoated glass plate (BK7, 2 mm thickness). The time delay $\tau$ between the two interfering pulses is 20 ps. It has to be large enough to obtain a reasonable number of interference fringes within the pulses' spectrum. On the other hand the sampling rate of the interferogram must fulfil the Nyquist criterion.

The transmitted portion of the pulse is used to generate the chirped pulse. The frequency shift $\delta\Omega$ has to be small enough to provide multiple sampling of the spectral phase (Whittaker-Shannon theorem), while with too small a frequency shift a noise problem arises. The two quantities are related by $\delta\Omega = \pi/\Phi_2$ where $\Phi_2$ is the group velocity dispersion (the second derivative of the spectral phase of the chirped pulse at the central frequency). The required $\Phi_2 = 2\times10^7$ fs$^2$ is reached in a standard double-pass grating stretcher consisting of two parallel gratings (1800 lines/mm, incidence angle 75°) with a separation of 200 mm. The pulses are overlapped in a 2 mm thick type-I KDP crystal.

The polarization of the up-converted signal is rotated by a periscope and the beam is focused by a 4x microscope objective through a 10 micron pinhole. The pinhole constitutes the entrance aperture for the spectrometer. It uses a 2400 lines/mm holographic grating (25×25mm$^2$) under 25° angle of incidence. The beam from the pinhole is expanded to >5 cm diameter to overfill the spectrometer grating. A 600 mm focal length lens images the pinhole onto the CCD camera chip (760x580 pixel). The camera is synchronized to the laser pulses.

Fig. 2 shows a typical interferogram obtained from the device in a single shot. For reconstruction of the spectral phase from a SPIDER interferogram a software developed at the University of Würzburg was adapted to read the interferograms provided from the SPIDER at GSI. The software is written in LabView, performs the complete SPIDER algorithm and provides a user-friendly graphical interface.

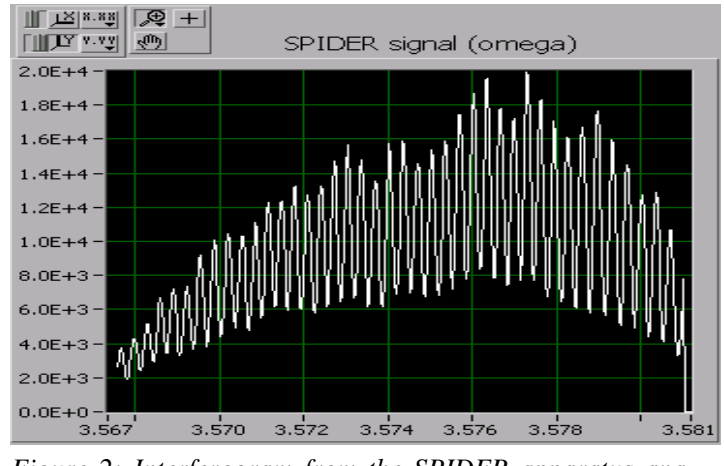


*Figure 2: Interferogram from the SPIDER apparatus analysed by the SPIDER software from Univ. of Würzburg.*

## References

[1] C. Iaconis, I.A. Walmsley, Optics Letters **23**, 792 (1998)

# Transient collisionally excited x-ray laser in nickel-like zirconium at PHELIX laser facility

P. Neumayer[1,2], D. Ursescu[1,3], T. Kuehl[1,3], K. Cassou[4], A. Klisnick[4], D. Ros[4], S. Borneis[1], E. Gaul[1], W. Geithner[1], C. Haefner[1], P. Wiewior[1,5], and W. Seelig[2]

[1]Gesellschaft fuer Schwerionenforschung mbH, Planckstr. 1, D-64291 Darmstadt, Germany; [2]TU Darmstadt, Institut fuer Angewandte Physik, Schlossgartenstr. 7, 64289 Darmstadt; [3]Johannes-Gutenberg-Universitaet Mainz, Germany; [4]LSAI/LIXAM, Bâtiment 350, Université Paris XI, 91405 Orsay, France; [5]Universitaet Wuerzburg, Germany

*Abstract*

A transient collisionally pumped X-ray laser (XRL) driven by the infrared pulses from the PHELIX laser preamplifier at GSI has successfully been put into operation. Strong lasing at 22 nm has been observed in nickel-like zirconium. Experimental data from the optimization of the XRL energy output support the conclusion that inverse Bremsstrahlung plays a key role in the pumping mechanism.

Laser induced fluorescence spectroscopy in lithium-like heavy ions can be performed using narrow bandwidth light pulses with a few $\mu$J of energy in the XUV spectral region [1]. Such pulses are routinely produced in the scheme of transient collisional excitation (TCE) x-ray laser , which was first demonstrated by Nickles et al. [2]. In this scheme, saturated output can be obtained with a few J of pulse energy from the pumping laser (see e.g. [3]). A laser pulse with an energy of a few J and ns duration is focused to a line onto a solid target, creating a line-shaped plasma with a high abundance of nickel-like ions. A high intensity short ($\sim$ ps) infrared laser pulse - produced by the technique of ,,chirped pulse amplification" (CPA) - heats the plasma rapidly to a high temperature which leads to a short lived (transient) population inversion. A bright, partly coherent XUV-pulse is emitted from the end of the plasma column by amplified spontaneous emission. Due to the short life time of the transient gain [4], the pumped region has to travel with the amplified radiation, which is achieved by so called travelling wave excitation [5].

At GSI, a high intensity/high energy laser system (PHELIX) is under construction [6]. The CPA front-end together with the preamplifier and pulse compressor are well suited for pumping a TCE XRL. The front-end delivers stretched pulses of $>$ 50 mJ with a bandwidth of $\sim$ 7 nm. The preamplifier consists of three flashlamp pumped Nd:Glass rods (with 2x 19 mm and 45 mm diameter) which amplify the pulses further to an energy of several J. The pulse compressor, in a double folded single grating arrangement, is entirely housed in a vacuum chamber and is designed to compress pulses of up to 15 J to durations below 400 fs. Pulses up to 10 TW peak power have been achieved. Without the use of adaptive optics for the wave front correction the repetition rate is limited by the cooling time of the three heads to one shot every 6 minutes .

For pumping the XRL we have used 5-6 Joule pulses; 20 % of the pulse energy are split off by a beam splitter and remain uncompressed to form the prepulse. After being delayed in an optical delay line the prepulse is injected into the target chamber and focused by means of a cylindrical lens to a line focus (80$\mu$m $\times$ 10mm) to create the preplasma.

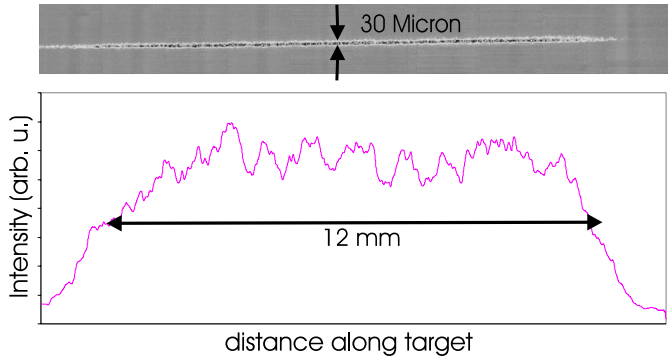


Figure 1: Line focus image and longitudinal intensity distribution for the infrared laser, obtained with the parabolic mirror

The remaining 80 % of the pulse are injected into the pulse compressor. After compression the pulse is transported under vacuum into the target chamber. A single on-axis parabola, tilted at an incidence angle of 22 degrees, is used to generate a line focus of 30$\mu$m 100$\mu$m width and over a length of 10 mm (fig. 1). The off-axis geometry intrinsically leads to a travelling wave excitation along the line focus with a close to the optimum speed of 1.4 c where c is the speed of light. The delay between the prepulse and the compressed pulse was set to 0.7 ns.

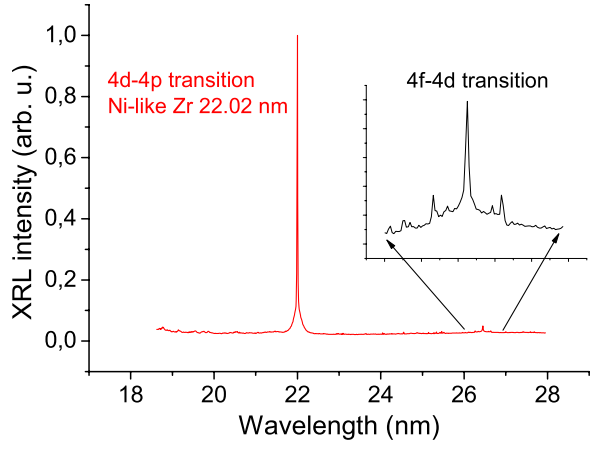


Figure 2: Typical spectrum of the Ni-like zirconium laser, corrected for the Al-filter transmission

The main diagnostics was an XUV flat-field Hitachi

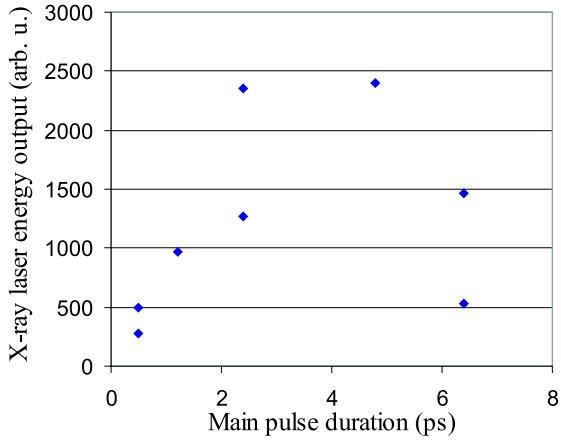


Figure 3: Energy output from the Ni-like zirconium laser for different main pulse durations at the same pumping energy

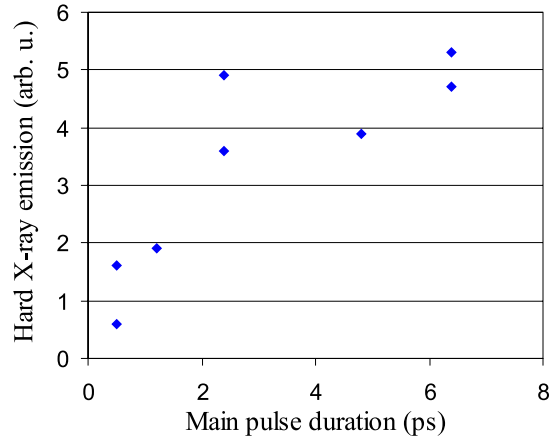


Figure 4: Integrated hard X-ray emission from the Ni-like zirconium plasma for different main pulse durations at the same pumping energy

grating spectrometer, monitored with a Princeton XUV CCD camera, with a resolution of about 0.01 nm/pixel.

The time integrated keV emission of the plasma was observed using a so called cross-slit camera. It provided a full length side view of the plasma with a transverse resolution of 10$\mu$m. This helps to control the overlap of the two infrared pulses along the whole length of the plasma line.

Using a zirconium target of 4.5 mm length and a total energy of 3 Joule on target, strong lasing are obtained from the 4d-4p transition in nickel-like zirconium at a wavelength of 22.02 nm (56 eV) as well as the self photo pumped 4f-4d transition at 26.46 nm in a highly reproducible spectrum (fig. 2). The corresponding intensities of the pre-pulse and of the short pulse were $2 \cdot 10^{11}$ W/cm$^2$ and $8 \cdot 10^{14}$ W/cm$^2$, respectively. In the absence of either the prepulse or the short pulse, no line emission is observed. Still we observed the lasing transition line with ten times less intensity for the pre-pulse.

During the experiment short pulse durations of 0.4, 1.2, 2.4, 5 and 6.4 ps (see fig. 3) were used while keeping the total pulse energy constant to within 12 %. An optimum with respect to the XRL output intensity was obtained for a duration of the short pulse $\sim$ 2.4 to 5 ps for which the output of the XRL was about four times higher than for the the shortest possible pulse duration of 0.4 ps (fig. 3). Similar findings are reported e.g. in [3], however, no explanation has been given so far for this effect. Here, in addition we evaluated the brightness of the images taken by the cross slit camera for these shots (fig. 4). A strong increase of the intensity in the images from the plasma emission can be observed. The camera is protected by a thin aluminium filter which transmits mainly radiation with photon energies above 500 eV. Therefore the camera gives a qualitative estimation of the total amount of keV radiation emitted from the laser plasma and thus an image of the hot regions of the plasma. This suggests that higher temperatures are achieved using longer pulses of the same energy. Although the measurements are time-integrating and the increase in emission time could play a role [7], we propose that the reduction of inverse Bremsstrahlung absorption contributes strongly to this behavior. At conditions typical for TCE XRL, i.e. temperatures of a few tens of eV for the XRL pre-plasma and laser intensities between $10^{14}$ and $10^{15}$ W/cm$^2$ in the short pulse the process of inverse bremsstrahlung absorption strongly decreases with increasing intensity [8]. The decrease of XRL output signal for even longer pulses can be attributed to over-ionization of the Nickel-like ions. Further investigation for comparison of the theoretical model with the experiments will follow in 2004.

In conclusion we presented a new XRL system capable of routinely producing XUV-pulses at a wavelength of 22 nm at a repetition rate of 1 shot per 6 minutes. A novel short pulse focusing geometry has been used for the first time. Besides being inexpensive and easy to use, it provides a near optimum intrinsic travelling wave velocity of 1.4 $c$. The observed optimum output for the short pulse duration, in combination with the images of the keV plasma emission can be explained by a decreased inverse bremsstrahlung absorption at higher laser intensities.

## References

[1] S. Borneis et al., Hyperfine Interactions **127,** (2000) 537.

[2] P.V. Nickles, V.N. Shlyaptsev, M. Klachnikov, M. Schnürer, I. Will, and W. Sandner, Phys. Rev. Lett. **78,** (1997) 2748.

[3] J. Dunn, Y. Li, A.L. Osterheld, J. Nilsen, J.R. Hunter, and V.N. Shlyaptsev, Phys. Rev. Lett. **84,** (2000) 4834.

[4] A. Klisnick, et al.Phys. Rev A **65,** (2002) 033810.

[5] A. Klisnick, et al. J.O.S.A. B **17,** (2000) 1093-7.

[6] PHELIX-Proposal, GSI-Report **GSI-98-10,** (1998).

[7] Y. Abou-Ali, et al. Optics Comm. **215,** (2003) 397

[8] L. Schlessinger and J. Wright, Phys. Rev. A **20,** (1979) 1934.

# VUV-FEL User Facility at DESY

E. Plönjes
HASYLAB, Deutsches Elektronen-Synchrotron DESY, Hamburg, Germany

The free electron laser (FEL) at the TESLA Test Facility (TTF) at DESY achieved first self amplified spontaneous emission (SASE) in the vacuum-ultraviolet in early 2000 [1]. In 2001, SASE FEL gain up to saturation was reached between 80 –120 nm [2, 3]. During an on-going upgrade which will be completed at the end of 2004, the VUV-FEL at DESY is transformed into a full user facility with five experimental stations using the FEL beam alternately [4, 5]. Expected FEL parameters are summarized in Table 1. Three experimental stations use the direct SASE FEL beam and are equipped with focusing mirrors providing spot sizes of approximately 100 or 10 μm. Two experimental stations are served by a high resolution monochromator for experiments requiring a spectral bandwidth narrower than the natural FEL bandwidth of ~ 0.5 %. The plane grating monochromator has a resolution of 80000-10000 while providing a wide tuning range from 10 eV to 1 keV.

The exponential amplification process of a SASE FEL starts from spontaneous emission of the electron beam [6]. Hence, individual radiation pulses differ in intensity, temporal structure, and spectral distribution. Extensive characterization of the FEL beam [1-3, 7, 8] as well as a first set of experiments on the interaction of such VUV radiation with cluster beams [9] and surfaces [10] was carried out during TTF Phase 1 and showed that exploitation of the unique FEL properties requires suitable pulse-resolved diagnostic tools.

A FEL intensity monitor has to cover the full spectral range from 6 to 120 nm as well as a very large dynamic range from spontaneous undulator emission to SASE in saturation. For that purpose, an absolutely calibrated gas-monitor detector based on photoionisation of noble gases at low target densities has been successfully tested during TTF Phase 1 [12]. Currently, the gas-monitor detector is upgraded with split electrodes allowing time-resolved determination of the horizontal and vertical beam position. In addition, a 15 m long windowless noble-gas-filled section of the beam tube with adjacent differential pumping units will be used as a means to attenuate the FEL radiation intensity without changing the FEL beam characteristics.

The spectral distribution of individual FEL pulses will be determined online by a variable-line-spacing (VLS) grating spectrometer serving the three “SASE beamlines” [11]. One of the plane mirrors in the FEL beam distribution system will be replaced by the VLS grating which reflects most of the radiation in zeroth order to the experiment and disperses only a small fraction in first order for spectral analysis.

The degree of spatial coherence of FEL radiation is very high [8], but it varies slightly with the degree of saturation. Also, beamline optics will affect the wavefront propagation. Therefore, tools to measure and eventually to correct the wavefront are developed to provide a uniform intensity distribution in the focal spot on the sample and to achieve smallest spot sizes for high-brightness applications.

The short X-ray pulse duration of typically 100 fs or potentially shorter is one of the most attractive features of linear accelerator (linac) based free electron lasers. To exploit these ultrafast pulses in two-colour pump-probe experiments, the FEL is complemented by an optical laser system. The optical laser comprises a Ti:Sa oscillator and an optical parametric amplifier pumped by a high-power Nd:YLF laser which is based on the design of the photocathode laser of the linac injector. This concept was chosen because it provides a great deal of flexibility for later upgrades in terms of tuning range, pulse duration and average output power. The most demanding task of the project is the synchronization of FEL and laser, including beam and signal transport over long distances and the development of suitable diagnostics for pulse duration and exact phase control between the FEL and the optical laser pulses.

Alternatively, an autocorrelation setup using grazing incidence plane mirrors will be integrated into a beamline for FEL pulse duration measurements. Also, single-colour pump-probe experiments or, using suitable filters, a combination of first and third harmonic FEL radiation will be possible, allowing ultimate time resolution independent of the pulse timing [13].

**TABLE 1. Expected parameters of the VUV FEL at DESY.**

| | |
|---|---|
| **Electron beam** | |
| Energy | 0.2 – 1 GeV |
| Number of bunches per train | up to 7200 in 800 μs |
| Repetition rate | 1 - 10 Hz |
| Bunch charge | 1 nC |
| **FEL radiation** | |
| Wavelength | 120 – 6 nm |
| Pulse energy | 0.1 – 1mJ |
| Pulse duration (FWHM) | 30 – 400 fs |
| Peak power | 0.3 - 2.8 GW |
| Spectral width (FWHM) | ~0.5 % |
| Spot size at undulator exit (FWHM) | 1.4 – 0.14 mm |
| Angular divergence (FWHM) | 170 – 24 μrad |
| Peak brillance | 1x $10^{28}$ – 3x$10^{30}$ photons/sec/mrad$^2$/mm$^2$/0.1 %bw |

## References

[1] J. Andruszkow et al., Phys. Rev. Lett. 85 (2000) 3825
[2] V. Ayvazyan et al., Phys. Rev. Lett. 88 (2002)104802
[3] V. Ayvazyan et al., Eur. Phys. J. D 20 (2002)149
[4] K. Tiedtke et al., Proceedings of the SRI 2003, San Francisco, CA, U.S.A. 2003
[5] http://www-hasylab.desy.de/facility/fel/
[6] E. L. Saldin, E. A. Schneidmiller, and M. V. Yurkow, “The Physics of Free Electron Lasers”, Springer , Berlin (1999)
[7] R. Treusch et al., Nucl. Instr. and Meth. A 445 (2000) 456
[8] R. Ischebeck et al., Nucl. Instr. and Meth. A 507 (2003) 175
[9] H. Wabnitz et al., Nature 420 (2002) 482
[10] A. Andrejczuk et al., HASYLAB An. Rep. 1 (2001) 117
[11] R. Reininger et al., Proceedings of the SRI 2003, San Francisco, CA, U.S.A. 2003
[12] M. Richter et al., Appl. Phys. Lett. 83 (2003) 2970
[13] J. Feldhaus et al., Nucl. Instr. Meth. A 507 (2003) 435

# Space Resolved Study of Laser Produced Plasmas

G. Rodríguez Prieto[1,2], M. Schollmeier[1], F.B. Rosmej[3], O. Rosmej[1], Y. Maron[4], and D. H. H. Hoffmann[1,2]

[1]GSI Darmstadt; [2]TU Darmstadt; [3]PIIMA, Université de Provence et CNRS, Marseille; [4]Weizmann Institute of Science, Rehovot

The study of plasma accelerated ions is an important topic nowadays [1]. The acceleration of ions is produced for electric fields caused by plasma density gradients. So a diagnostic of the plasma density and temperature is necessary. It is frequently achieved using spectroscopic methods with the light from He-like and Li-like plasma ion transitions emitted in the soft x-ray region, 1-1000 $\mathring{A}$ wavelength range[2]. Most of these experiments were done without

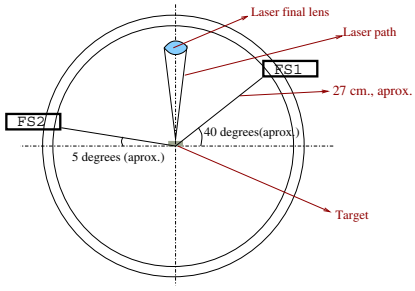


Figure 1: Target Chamber Experimental Setup

spatial resolution, so the distribution of plasma parameters cannot be achieved. Therefore schemes with spatial resolution were developed and used successfully like the **F**ocusing spectrograph with **S**pherical dispersive element and **S**patial **R**esolution (FSSR)[3]. The images are recorded on x-ray films. In experiments done at GSI, to examine the presence of accelerated ions in low energy laser plasmas, space resolved studies with FSSR were successful. Two spectrometers, the labeled FS1 and FS2 in fig. 1 were focused on their Rowland circle. The horizontal axis in the film corresponds to the wavelengths and the vertical to the plasma displacement respect to the initial target surface(fig. 2). The plasma is produced by nhelix laser shots

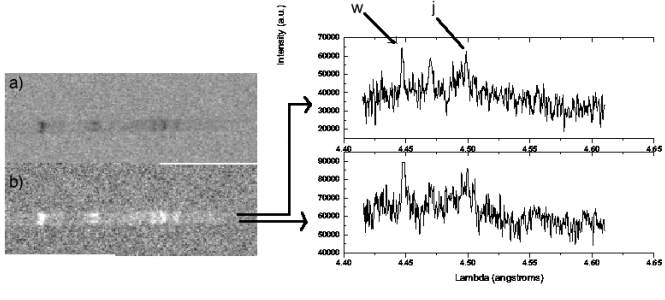


Figure 2: Films; a) raw and b) enhanced with the spectra at two different positions

(Maximum energy 100 J, full width half maximum of the laser pulse 15 ns and $\lambda = 1.064$ nm) on massive (thickness 1-2 mm) plane Polyvinyl chloride targets perpendicular to the laser beam. The plasma light emission from chlorine ions was detected. After scanning the films, some image treatment had to be done (see fig. 2). From the enhanced image, spectra at different positions with respect to the target were extracted. The intensity ratio between the *1s2l3l' transitions*, $j(1s^2 2p\ ^2P_{3/2} - 1s2p^2\ ^2D_{5/2})$ and $k(1s^2 2p\ ^2P_{1/2} - 1s2p^2 {}^2D_{3/2})$ He-chlorine satellites is presented in fig. 3. This ratio has a strong dependence on the temperature. The temperature ratios are rather constant

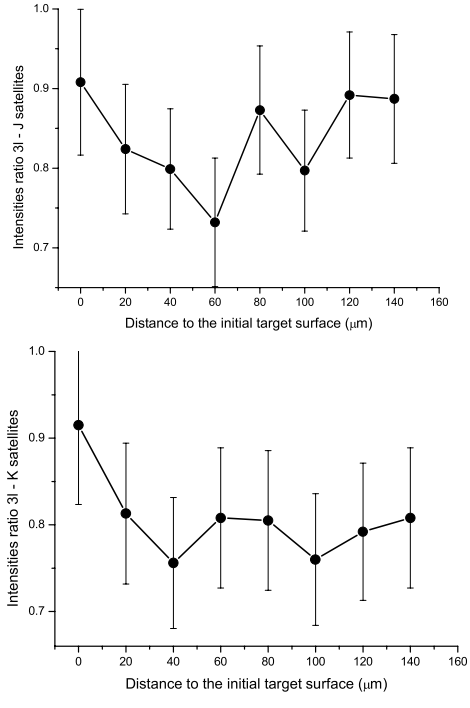


Figure 3: Intensity ratio of 3l'-j and 3l'-k satellites

within the error bars. The temperature follows also this distribution[4]. Two possibilities arise to explain this flat temperature distribution. Either the temporal integration produces this effect, or the sensitivity to the temperature of the diagnostic method is low then the variations in temperature are not visible.

## References

[1] F.B. Rosmej et al., JETP, **94,1** (2002) 60-72
[2] C. De Michelis and M. Mattioli, Nucl. Fus. **21,6** (1981) 677-754.
[3] A. Ya. Faenov et al., Physica Scripta. **50** (1994) 333-338.
[4] O. Renner et al., Appl. Phys. Lett. **79** (2001) 177

# Investigation laser-produced chlorine plasmas for x-ray scattering experiments

M. Schollmeier[1], G. Rodríguez Prieto[1,2], F.B. Rosmej[3], T. Schlegel[2], Y. Maron[4], and D.H.H. Hoffmann[1,2]
[1]TU Darmstadt; [2]GSI Darmstadt; [3]PIIMA, Université de Provence et CNRS, Marseille; [4]Weizmann Institute, Rehovot, Israel

For future investigations of strongly coupled plasmas with electron temperature above the Fermi temperature, $N_e$ near solid density and the electron-electron coupling paramter $\Gamma_{ee} > 1$, there is a need for new diagnostics. This matter has such a low temperature, that emission spectroscopy is not possible and probing with visible or UV-light is also impossible as it cannot penetrate the plasma due to the corresponding low critical electron density. One possibility to elude this problem is spectrally resolved x-ray scattering, which can be realized by the kilojoule PHELIX-laser as the driver for the x-ray source. Spectrally resolved x-ray scattering potentially provides both electron density and temperature from the red-shifted line-wings of the scattered radiation [1]. For these purposes it is important to know the underlying satellite structure in this wings.

A future probing beam could be the $He_\alpha$-resonance line of chlorine with a wavelength of $\lambda = 0.4444$ nm. A high-reflectivity Bragg-crystal spectrometer is needed to resolve this scattered radition. Here highly oriented pyrolytic graphite (HOPG, $2d = 6.708$ Å) [2] seems to be a good candidate. Due to its rocking-curve the spectral resolution of the crystal is about 500. Unfortunately one cannot resolve the dielectronic structure that is underlying the probing $He_\alpha$-transition radiation.

To investigate the influence of these satellites on the spectrum of the source and to calibrate this spectrometer we used a focusing spectrometer with spatial resolution (FSSR) [3] with a spherically bent mica crystal ($2d = 19.915$ Å, $R = 150$ mm, $\lambda/\Delta\lambda$ up to 10000) in a FSSR-1D scheme. The x-rays were recorded with Kodak DEF-5 films. With this set-up one can get the characteristics of the source with high spectral resolution and determine experimentally the blended transitions of the HOPG-spectrum.

We used the chlorine $He_\alpha$-line to calibrate a newly developed flat HOPG-spectrometer with the FSSR. The radiation was produced by illuminating massive PVC targets with the NHELIX laser beam (Nd:YAG, energy up to 140 J in 14 ns). The spectrometers were placed at a distance of 22.7 cm (FSSR) and 13.6 cm (HOPG) on opposite sides of the target at an angle of $\approx 10°$ according to the surface.

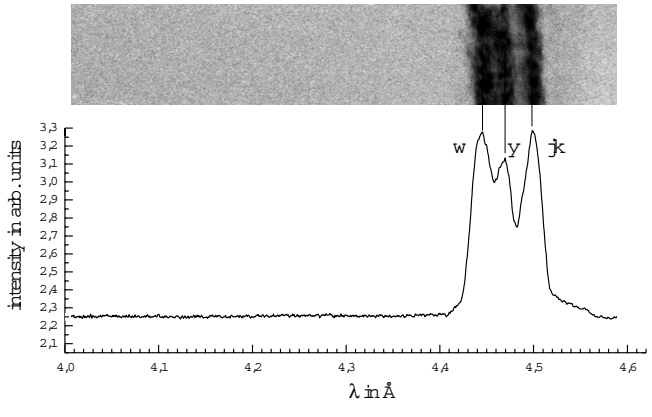


**Fig. 1:** Spectrum of one single shot. The upper image is the HOPG-spectrum on the film, the lower image the intensity-trace over the entire width of the film.

Fig. 1 shows the image and spectrum of the HOPG-spectrometer. The laser energy of the shot was 64 J. The image was digitized with a high-resolution drum-scanner (Eurocore HI-SCAN). On the image one can see the resonance-line $w$, intercombination line $y$ and the $jk$-satellites. Due to the mosaic spread of the crystal of 0.4°, the lines are not sharp and look a little bit blurred. The densitogram of the image is shown below. Despite the $jk-$line, the dielectronic satellites of $He_\alpha$ are not resolved. In contrast to this, the satellites in the FSSR-spectrum in fig. 2 are very good resolved. By using the imaging property of the FSSR and the magnification $M = \cos[2(90-\vartheta)] = 0.59$ with the Bragg-angle $\vartheta = 63.2°$ of Cl-$He_\alpha$, the size of the radiating region is determined to $z = 320$ $\mu$m.

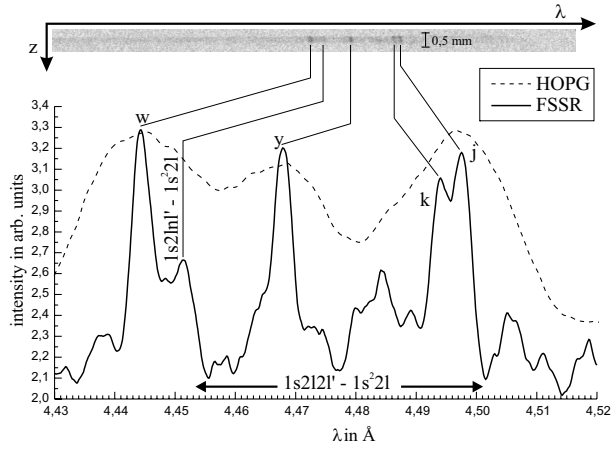


**Fig. 2:** The same shot as Fig. 1. The upper image shows the recorded FSSR-spectrum on the film, the lower image the intensity-trace. For comparison the HOPG-spectrum is plotted in dashed lines.

According to the high density of the plasma, the resonance line is optically thick and the determination of the electron temperature needs modelling which is currently under development.

With regard to future scattering experiments we are able to produce a nearly point-like high-brilliant x-ray source that emits a narrow band of x-rays with a spectral width (FWHM) of $\Delta\lambda = 0.07$ Å. Unfortunately the amount of produced photons will not be enough for real scattering experiments using the NHELIX-laser as a driver. As showed in ref. [4] the number of probe photons in an optimised experiment using a framing-camera with MCP is $10^4$ for the laser-energy of 5 kJ, scaling with the laser-energy $E^2$. This explains why one needs the PHELIX-laser for scattering experiments on warm dense matter.

## References

[1] S.H. Glenzer *et. al.*, Phys. Rev. Lett. **90**, 175002 (2003)
[2] A.W. Moore, Chem. and physics of carbon, Vol. 11, p. 69
[3] A.Ya. Faenov *et. al.*, Phys. Scr. **50**, pp. 333-338 (1994)
[4] O.L. Landen *et. al.*, JQSRT **71**, pp. 465-478 (2001)

# Dynamics of the projectile ion velocity during the stopping process in solids

O. Rosmej[1] , S. Pikuz[2] , S Korostiy[1] , A. Fertman[4] , T. Mutin[4] , A.A. Golubev[4] , V. Efremov[5], A. Blazevic[3], D.H.H. Hoffmann [1,3]

[1]GSI-Darmstadt, Germany; [2] Moscow State University; [3]TU-Darmstadt, Germany; [4]Institute of Experimental and Theoretical Physics, Moscow, [5] Institute High Energy Density, Moscow

The investigation of heavy ion stopping dynamics using associated *K-shell* projectile and target radiation was in the focus of the reported experiments. Ar projectile ions with the initial energie of 11.4 MeV/u were stopped in quartz and low density aerogels. K-shell projectile and target radiation was investigated spatially resolved perpendicular to the ion beam trajectory using spherically bend mica crystal spectrometer [1,2]. In contrast to the target radiation, the radiation of relativistic ions moving with velocities of 1/10 of light speed undergo relativistic Doppler effect. Fig.1 shows the Doppler line shift attenuation due to the ion energy loss along the ion track in solid target. In the picture, $\lambda_0$ – the wavelength of a radiative transition in the ion at rest, $\lambda_{D1}$ and $\lambda_{D2}$ – shifted due to the Doppler effect wavelength of the same radiative transition of the moving ion at the beginning and the end of the observed trajectory.

The variation of the Doppler shift of the projectile radiation measured along the ion beam track was used to determine the ion velocity dynamics [3]. K-shell resonance radiative transitions in $Ar^{+17}$ (Ly$\alpha$) and $Ar^{+16}$ (He$\alpha$) were used. Si - K$\alpha$ ( target material) served as a reference line.

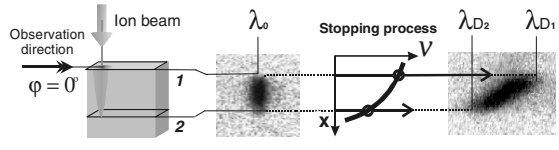


**Fig. 1** Variation of the Doppler line shift along the ion beam track in the stopping process.

The choice of $SiO_2$ aerogel with low avarage densities of 0.04-0.15 g/cm$^3$ as a target material [4] allowed to stretch the ion stopping range by more than 10-50 times in comparison with solid quartz. For the first time, dynamics of the ion stopping process in solid was resolved. The dependence of the ion velocity on the trajectory coordinate was measured over 70-90% of the ion beam track with a spatial resolution of 50-70 μm. The experimental results normalized on $V_{input}$ - the initial ion velocity are compared with the results of the projectile velocity dynamics calculated using SRIM program are presented in Fig.2

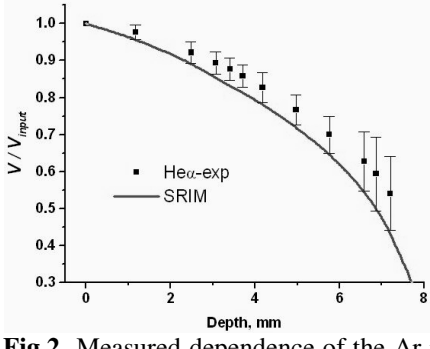


**Fig.2** Measured dependence of the Ar ion velocity on the penetration depth in 0.04g/cm$^3$ aerogel target .

We investigated the possible influence on the stopping process of the aerogel porous nano-sracture. The energy loss and charge state distribution of 11.4 MeV/u Ar ion beam interacting with 50 um Al foil and 3mm aerogel target of the same linear density were measured. For energy loss measurements time-of-flight method was used. The ion charge state distribution was analyzed by mean of the calibrated magnet with the entrance slit.

The energy loss of 11.45 MeV/u Ar beam in 3 mm of 0.04 g/cm$^3$ aerogel target has been measured to be of 3.40±0.07 MeV/u, in Al foil of 50±1 μm thickness - of 3.16±0.07 MeV/u. This results are in a good agreement with SRIM-calculated value of 3.20±0.07 MeV/u.

Fig.3 demonstrates measured Ar projectile charge state distributions after interaction with Al and aerogel targets.

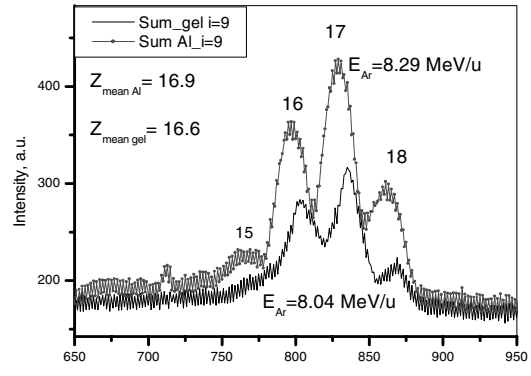


**Fig. 3** Ar charge state distribution after aerogel target with a linear density of 0.012g/cm$^2$ and Al target of 0.013g/sm$^2$.

Measured average charge states of Ar ions are: Z=16.9 after Al and Z=16.6 after aerogel target.

These results prove that at our experimental conditions the $SiO_2$ aerogel pores of 30-50nm sizes does not seriously influence the ion stopping processes.

Finally, the combination of the outstanding properties of spherically bent crystal spectrometers and the target material used in the experiments has allowed to visualize and to measure the projectile ion stopping dynamics in solid matter.

## References:

[1]A.Ya.Faenov et al., Phys. Scripta, **50**, 333 (1994)
[2] O.N. Rosmej et al., NIM A, **495**, 29 (2002)
[3] O. N. Rosmej et al, RSI **74**, N12 (2003)
[4] B.A.Demidov et al, Zhurnal Teknich. Fiziki, **43**, Issue 10,1239-1246 (1998)

The work was supported by DAAD and NATO grand PSTT CLG 979372

# Observation of Enhanced Energy Loss of Xe- and Ar-ions in Shockwave-driven, Non-ideal Plasmas

K. Weyrich[1], H. Wahl[2], A. Golubev[3], A. Kantzyrev[3], M. Kulish[4], S. Dudin[4], D.H.H. Hoffmann[1,2], B. Sharkov[3], V. Mintsev[4]
[1]TU Darmstadt, [2]GSI Darmstadt, [3]ITEP Moscow, [4]IPCP Chernogolovka

For non-ideal plasmas with Γ-parameters ≥ 1 theory predicts a deviation from the $Z_{eff}^2$-behaviour for the energy loss of ions as known in weakly coupled plasmas [1], but no experimental data-base, describing these interaction processes exists yet. Interaction of heavy ions with strongly-coupled plasmas and possible non-ideality effects in the density regime up to $10^{22}$ e-/cm$^3$ and temperatures between 1-10 eV are of interest for investigations in the warm dense matter regime, laboratory astrophysics and basic ICF-research. Such conditions can be realized in shockwave-driven plasmas, as they are investigated at the Z6 experimental area at GSI since 2001. A shockwave that creates the plasma originates from the detonation of a high explosive, and compresses gas (Xe or Ar) in a glass-tube. In front of the shockfront a plasma layer propagates through the target. For details of the experimental principle, development of an optimized target, plasma diagnostis and first results for interaction experiments with C-ions see [2].
In the Ar-plasma free electron densities between 0.26 – 1.5 $*10^{20}$cm$^{-3}$ for initial Ar-pressures between 0.2 – 3 bar were reached and Γ-parameters between 0.6 – 1.3 at temperatures about 2 eV. The energy loss of C-, Ar-, and Xe-ions at 5.9 MeV/u and 11.4 MeV/u was measured with a TOF-method. An enhancement of the energy loss in the compressed plasma-phase above the cold Ar-gas at the same line density could be observed in the experimental data. The results for C-ions have been presented in [2] and further analysis of the data could confirm the measured enhancement of the energy loss. Such an enhancement could also be observed in the recent measurements with Ar- and Xe-ions described here.

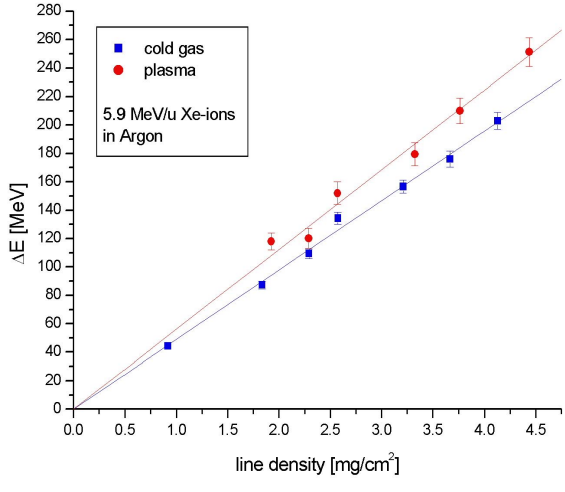


Fig.1: Energy loss of 5.9 MeV/u Xe-ions in Argon

Fig. 1 shows the energy loss of 5.9 MeV/u Xe-ions as function of the Ar-gas, repectively, plasma density. For the 5.9 MeV/u ions the enhancement of the energy loss compared to the one in cold gas for the 3 different ion species varied between 15–23 % and for the 11.4 MeV/u C- and Ar-ions between 6.8–10.5 %.

| $^{40}$Ar at 5.9 MeV/u and 11.4 Mev/u | | | | |
|---|---|---|---|---|
| **p[bar]** | 0.2 | 0.6 | 1.0 | 2.0 |
| Enhancement | 23 % | 21 % | 8.1% | 6.8 % |
| e$^-$/Ar-part. | 0.524 | 0.4273 | 0.37 | 0.3 |

Table1: Energy loss enhancement of Ar-ions

| $^{132}$Xe at 5.9 MeV/u | | |
|---|---|---|
| **p [bar]** | 0.2 | 0.6 |
| Enhancement | 16.5 % | 15.5. % |
| e$^-$/Ar-part. | 0.524 | 0.427 |

Table 2: Energy loss enhancement of Xe-ions

The enhancement is attributed to the free electrons in the compressed plasma phase, even if the major amount of electrons is still bound. Tables 1 and 2 list initial gas pressure, enhancement in energy loss and the ratio of free electrons and Argon particles, either neutral or ionized. The data below 1 bar are for 5.9 MeV/u ions while those ≥ 1 bar for 11.4 MeV/u ion energy. While for the lower energy ions a decrease in the enhancement with higher particle densities can only be estimated, for the 11.4 MeV/u Ar-ions the decrease in enhancement is significantly about 16 % which is close to the decrease of the ratio between free electrons and Argon particles (19%) between 1 and 2 bar, which is a strong evidence that we see here really the part of the energy loss contributed by the free electrons. Calculations (code from the IPCP in Chernogolovka) for 5.9 MeV/u Xenon-ions predict 10 % enhancement at 01. bar initial Ar-pressure and 7 % at 0.7 bar, which is less, then we have measured in our experiments. An influence on the charge state of the ions in the compressed plasma phase is discussed also. Subpression of recombination processes due to the higher particle density in the compressed argon, the compression factor varies between 10–8, would contribute to the enhancement of the energy loss by increased charge states.
Simultaneous measurement of energy loss and charge states, to receive information on the charge state distribution of the ions after having passed the plasma, is planned in the next beam-time in late spring 2004.

**References**

[1] G. Zwicknagel et. al., Phys. Rep. 309 (1999) 117
[2] K.Weyrich et. al., GSI-Report 2002, GSI-2003-1, May 2003, p. 135

# Energy losses of low energy Cu-ions in gases

T. Mutin, M. Basko, V. Dubenkov, A. Fertman, A. Golubev, T. Kulevoy, R. Kuybida, V. Pershin, B. Sharkov

Institute for Theoretical and Experimental Physics, Moscow

Energy losses of low energy ions (<500 keV/u) in plasmas were measured in very few experiments ([1], [2]). To enlargen the amount of data in this ion energy region a new experimental set-up for stopping power measurements based on a 27 MHz RFQ-linac „HIPr“ has been desinged and assembled at ITEP, Moscow. The first results of the planned experiment are reported here. Energy losses of 101 keV/u Cu-ions in nitrogen and hydrogen have been measured for subsequent comparison with the energy losses of the same ions in a plasma. The experimental scheme is shown in fig.1.

fig.1

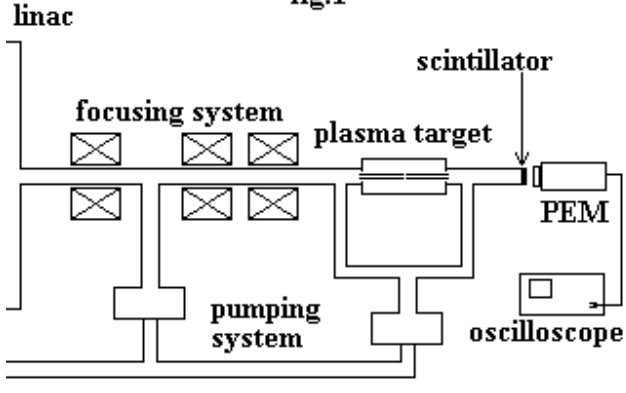


The ion transporting system [3], which consists of three quadrupole lenses has been adjusted to achieve a parallel beam in the target region for maximum intensity on the stop detector. The ion transport channel is pumped by turbomolecular pumps down to $10^{-6}$ mbar. The plasma was generated by igniting a 3 kA electric discharge in two 78 mm long collinear quartz tubes of 6 mm diameter [4]. It is closed at both sides by 1 mm diameter diaphragms. This scheme allows to produce a plasma with a linear electron density up to $5 \cdot 10^{17}$ cm$^{-2}$. Differential pumping at a rate of 500 l/s proved to be sufficient for insulating the vacuum beam line from the pressurized target during its operating cycle. In this experiment it was used as a gas target, i.e. without firing a discharge. The gas pressure was measured by a Balzers vacuum gauge. The measurements have been performed for the pressure range 0.5 – 2.0 mbar in nitrogen and for a single value of 1 mbar in hydrogen.

The energy loss was measured by a time-of-flight method (ToF). In our case the ToF start signals are derived from the high frequency of the accelerator, which provides bunched beams. At the end of the 185 cm long flight-path the stop-detector was positioned. A combination of a fast scintillator and a photoelectron multiplier (PEM) was used for the registration of the ion beam microstructure.

Measured energy losses of Cu-ions in nitrogen are presented in fig.2. Large discrepancy between the experimental points and the predictions of both, the semiempirical SRIM code and the theoretical STIP model (ITEP), show that our understanding of the stopping of low energy heavy ions even in cold gas targets is still far from complete, and new accurate measurements will be quite valuable for testing theoretical models.

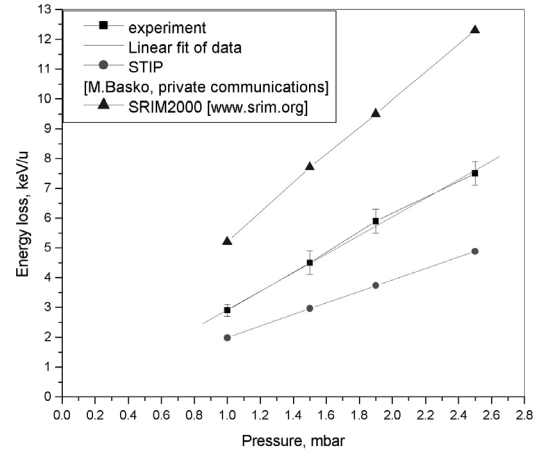


**Figure 2: Energy loss of 101.5 keV/u Copper ions in a Nitrogen cell of 160 mm length**

This project is supported by RFBR 03-02-17226.

## References

[1] R. Kowalewicz, E. Boggasch, D.H.H. Hoffmann et.al., Laser and Particle Beams, V.14(1996), N4, p.599

[2] Y. Oguri, S. Abe, A. Sakumi, Nucl. Instr. And Meth. A, V. 415(1998), N3, p.657

[3] S. Vysotsky et al. preprint 22-01, ITEP, 2001

[4] G. Belyaev et al., Phys. Rev. E, 53, 3, 2701 (1996)

# Report on December 2003 Beamtime Experiment at HHT: Near-Critical HED States of Lead Generated by Intense Uranium Beam

D. Varentsov[1,2], A. Adonin[3], V.E. Fortov[4], V.K. Gryaznov[4], D.H.H. Hoffmann[1,2], M. Kulish[4], I. Lomonosov[4], V. Mintsev[4], P. Ni[1], D. Nikolaev[4], N. Shilkin[4], A. Shutov[4], P. Spiller[2], N.A. Tahir[2], V. Ternovoi[4], and S. Udrea[1]

[1]Technical University Darmstadt; [2]GSI-Darmstadt; [3]University Frankfurt; [4]IPCP-Chernogolovka

This paper presents a preliminary report on a recent beamtime experiment on investigation of heavy-ion-beam generated high-energy-density (HED) matter. The experiment has been performed at the HHT experimental area of GSI on 11–17.12.2003.

**Goals of the experiment.** Main goals of this experiment were commissioning of a new multi-channel pyrometer for temporally resolved temperature measurements, improvement of transport, final focusing and diagnostics of full-intensity uranium beams and experimental test of a novel target design as well as of a few ideas on target diagnostics. Eventually, the experiment could also provide new data on thermodynamic properties and hydrodynamic response of lead in HED states. Since lead is one of the few metals which HED states near the critical point have been previously investigated in shock wave experiments [1, 2], it has been taken as a target material in order to validate the usefulness of the HIHEX method [3] for HED research and to benchmark the obtained experimental data.

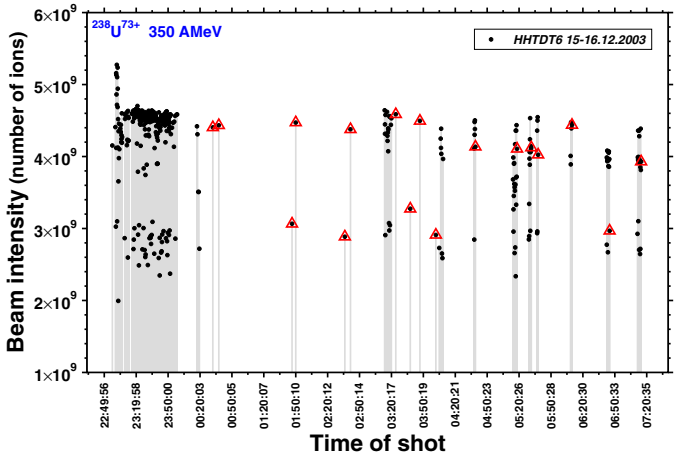


Figure 1: Shot-to-shot record of the beam intensity delivered to the HHT target area. Triangle marks indicate successful shots on the targets.

**Ion beam and accelerator performance.** In the experiment, intense beams of $^{238}\mathbf{U}^{73+}$ ions with initial energy of 350 AMeV have been used. The GSI accelerator facility has demonstrated excellent performance: the beam intensity was more than $4 \cdot 10^9$ particles/bunch (Fig. 1), whereas the bunch has been compressed in time down to 125 ns (FWHM) (Fig. 2). Such a high intensity of uranium beam and short bunch length have never been previously achieved at GSI. The beam intensity and the temporal shape of the beam pulse have been recorded for every shot by various current transformers installed at the HHT beamline as well as by a fast Rogowski coil in the target chamber.

In order to avoid beam loses, the settings of the beam-

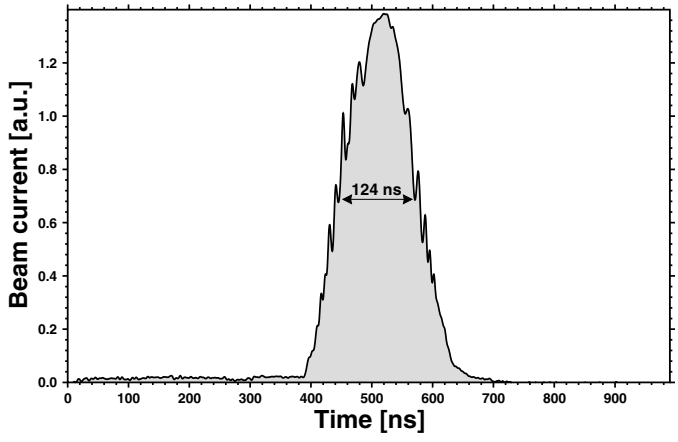


Figure 2: Time profile of the ion bunch after optimized bunch compression.

line magnets have been carefully optimized. The transmission of the beam from SIS-18 extraction to the HHT target area was 100% to the precision of the measurements. Final focusing of the ion beam on the target has been done in absence of the plasma lens, using the beamline quadrupoles. The focal angle has been considerably enlarged by installing special "buterfly"-shaped vacuum chambers in the last two quadrupoles prior to the experiment. The optimization of the beamline transmission and final focusing has been done using the $3^{rd}$-order ion-optical code GICO available at GSI. The results of these simulations are in excellent agreement with the measurements performed during the experiment. The distribution of the ion beam intensity at the target position and the focal spot size have been measured by recording beam-induced scintillation of argon gas. The target chamber was filled with argon at pressures 10–900 mbar and the scintillation images have been recorded by high-resolution amplified CCD cameras (DICAM-PRO, PCO) installed in two perpendicular planes. These cameras have also been used for precision beam-target alignment. The measured focal spot FWHM size was 0.85 mm (horizontal) × 1.6 mm (vertical), in accordance to the simulations. Such an elliptical shape and the spot size have been specially chosen in order to match the target geometry.

**Target design and experimental scheme.** A thin ($250\,\mu m$) foil of the target material is placed vertically along the ion beam, at the origin. The thickness of the foil is much smaller than the horizontal beam spot size, while the vertical beam extension is large. This target geometry therefore provides homogeneous volume heating of the sample and plane quasi-1D character of the hydrodynamic expansion of the heated target matter. Two sapphire plates are located parallel to the foil from both sides at certain distances, limiting the expansion and defining

the final volume. In order to avoid undesirable direct heating of the regions close to the foil and the sapphire plates by the beam, a thick slit diaphragm made of tungsten is installed in front of the foil. The whole target assembly is placed in a solid copper casing with additional sapphire windows at the faces. Besides protecting the target chamber and equipment from deposition of activated vapor of the target material after irradiation, this solid copper casing can serve as a sealed-off high pressure vessel. Therefore this target construction allows one to study quasi-isentropic expansion of target material into a buffer gas (e.g. — helium at different pressures) or vacuum.

Light emitted by the target in a certain area located far enough from the Bragg peak has been registered. This ensures the uniformity of the parameters and 1D character of the hydrodynamic response over the registration region. On one side of the target foil, the emitted light is observed by two electronic streak cameras. One streak camera has the entrance slit aligned along the beam axis and another one perpendicular to the beam axis. This allows the check of the uniformity of the target physical state in two planes. On the other side of the target, the light emitted in VIS/NIR wavelength region has been guided into 400 $\mu m$ quartz fibers using a 1:1 imaging system. The position of the observation region on the target can be adjusted by moving the fiber with three step motors. On the other end, these fibers were connected to a fast 6-channel pyrometer for time-resolved temperature measurement and optionally, to a small fiber optic spectrometer (USB2000, Ocean Optics Inc.) for recording time-integrated spectra.

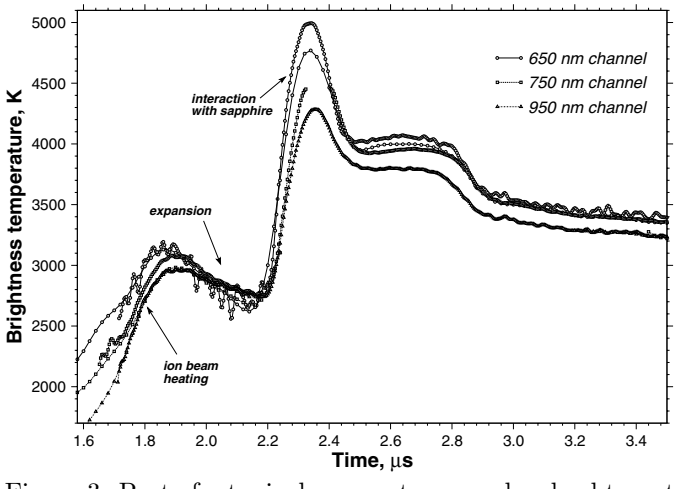


Figure 3: Part of a typical pyrometer record: a lead target heated by $^{238}\mathbf{U}$ beam, $4.44 \cdot 10^9$ ions/bunch.

**Fast radiation pyrometer.** In the performed experiment the key diagnostic instrument was a fast multichannel radiation pyrometer. This novel device recently developed by IPCP-Chernogolovka and GSI-Darmstadt allows one to record the evolution of target temperature with ns time resolution. The pyrometer analyzes the target radiation in the 500–1500 nm wavelength region, given by available interference filters and sensitivity of the photodetectors. There are no beam splitters used in the construction of the device but a filter itself acts as a mirror reflecting the radiation outside its transmission window toward the following channels for further wavelength filtering. This solution, together with a high amplification of the photodetectors, dramatically increases the sensitivity of the instrument. In fact, it was possible to trace the evolution of target temperature down to the level of about 800 K. The maximum brightness temperature measured in this experiment was about 5000 K. Other characteristics of the pyrometer are a high dynamic rage ($> 10^3$) provided by low-noise wide-band amplifiers and a modular design. At the moment the pyrometer has six channels and each channel provides two signals at different amplification levels simultaneously. The modular design of the device allows easy exchange of the filters and upgrade for additional channels. The absolute calibration of each channel has been done with a laboratory tungsten ribbon lamp (OSRAM Wi17/G) before the experiment. A typical pyrometer record for one of the experimental shots is shown in Fig. 3.

**Summary and outlook.** As a result of the beamtime experiment, it has been demonstrated that the fast multichannel radiation pyrometer is an indispensable diagnostic tool for HED studies with intense heavy ion beams. The data on temperature evolution of near-critical HED states of lead during ion-beam heating and quasi-isentropic expansion will be presented as soon as all the results are fully analyzed. It is also planned to compare this experimental data with 3D hydrodynamic simulations taking into account radiation transport phenomena. The usefulness of the quadrupole system for the final focusing of large-emittance uranium beam has been proved experimentally. Using the quadrupoles provides the focal spot size sufficient for such experiments while giving a full control over the beam shape and position, which is necessary in order to match a target design. The problem of vacuum windows damaging by intense beams, typical for a plasma lens focusing, can also be avoided.

The test of novel ideas employed in the "plane-HIHEX" target design has shown its great potential for future HED experiments. The precision of target positioning and alignment will be enhanced after constructing and installing a new six-axis target manipulator. The signal-to-noise ratio and quality of the pyrometric signals will be improved by using a better input optical system which will allow collecting the target radiation over a larger solid angle. However, in order to obtain the complete information on the thermodynamic state of the target, evolving of additional advanced diagnostic methods is still necessary. Therefore the development of an interferometric (VISAR) technique for pressure measurement as well as involvement of backlighting and shadowgraphy for recording the target density evolution is planned for future experiments. After validating the experimental design and diagnostic methods with test target materials such as lead, the ion-beam generated HED states in other materials of interest including copper, gold and uranium dioxide will be studied.

*This work is supported by GSI-INTAS (No.03-54-4254), by ISTC (No. 2170) and by BMBF.*

## References

[1] V.G. Ageev el al., JETP Lett. 48 (1989) 659.
[2] V.Ya. Ternovoi et al., SCCM-1995, (1996) 81–84.
[3] D.H.H. Hoffmann et al., Phys. Plasmas **9** (2002) 3651.

# Influence of focal length and beam rigidity on final focusing at HHT

D. Varentsov[1], P. Spiller[2], and S. Udrea[1]
[1]TU-Darmstadt; [2]GSI-Darmstadt

For future experiments on investigation of high-energy-density (HED) matter at GSI where an intense heavy ion beam *and* a petawatt laser beam from PHELIX will be used simultaneously, a new vacuum target chamber is required. Due to dimensions of the laser guiding and focusing optics, the new chamber has to be considerably larger than the presently installed at the HHT. It may therefore be necessary to shift the position of the interaction point father from the ion beam final focusing system. In order to study the influence of the extended focal length on the focusability of the ion beam and consequently, on the achievable levels of energy deposition in the target, a series of ion optical simulations has been carried out.

In the simulations, the exact layout of the beamline from SIS-18 to the HHT target chamber as well as the actual initial beam parameters ($\alpha$- and $\beta$-functions at the extraction) have been considered. Large transverse emittances of 40 mm·mrad (horizontal) and 10 mm·mrad (vertical) are assumed. Such values are typical for uncooled heavy ion beams at energies about 300 AMeV. The first-order ion optical simulations have been performed for uranium beams of three different magnetic rigidities:

**a)** $^{238}\mathbf{U}^{73+}$, 151 AMeV $\Longrightarrow$ 6 Tm;
**b)** $^{238}\mathbf{U}^{73+}$, 350 AMeV $\Longrightarrow$ 9.57 Tm;
**c)** $^{238}\mathbf{U}^{28+}$, 196 AMeV $\Longrightarrow$ 18 Tm;

using the code COSY INFINITY [1]. The case **a)** is supposed to be the design optimum for the present focusing system. The case **b)** corresponds to the recent beamtime experiment [2] and is preferable to case **a)** because of a higher ion energy and therefore longer ranges of ions in a target material. Due to a smaller charge, the highest intensity of uranium beams will be obtained by using $\mathbf{U}^{28+}$ ions of case **c)**. This 18 Tm beam is also very important for operation of the GSI future facility SIS-100.

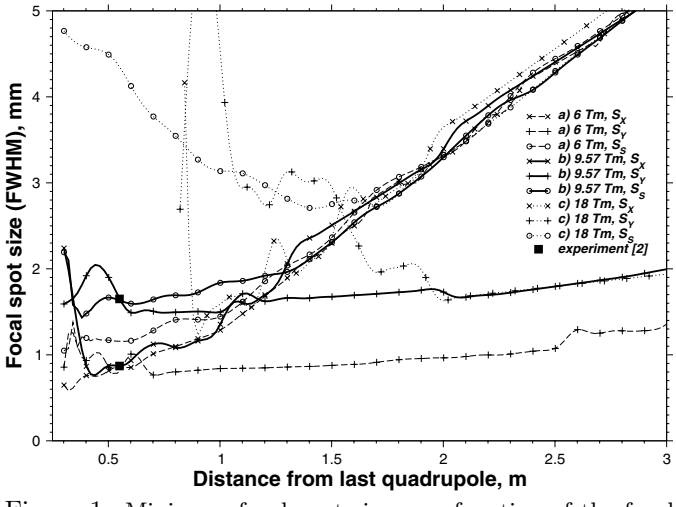


Figure 1: Minimum focal spot size as a function of the focal length. The black squares indicate the focusing settings of the recent HED experiment [2].

For HED experiments in cylindrical geometry a stigmatic focusing is needed, i. e. a round beam focal spot at the target, $S_X{=}S_Y{=}S_S$, whereas for experiments in plane geometry [2] an elliptical focal spot ($S_X{\neq}S_Y$) is preferable. We therefore performed two sets of calculations minimizing the quantities $S_S$ and $\sqrt{S_X S_Y}$, respectively. It is important to note, that the actual apertures of the quadrupole vacuum chambers and the strengths of the magnets have been taken into account. These constrains lead to a highly non-linear dependence of the minimum focal spot size at short focal distances below 1.2–1.6 m. Since the objective function has a very complicated structure with many local minima, a special optimization strategy has been chosen. First, an attempt to approach the global minimum of the objective function is done by varying the settings of the last five quadrupoles and using the Simulated Annealing algorithm in many iterations. After this, the optimization is refined with the last quadrupole triplet using the Simplex minimization algorithm. The results of these calculations are shown in Fig. 1.

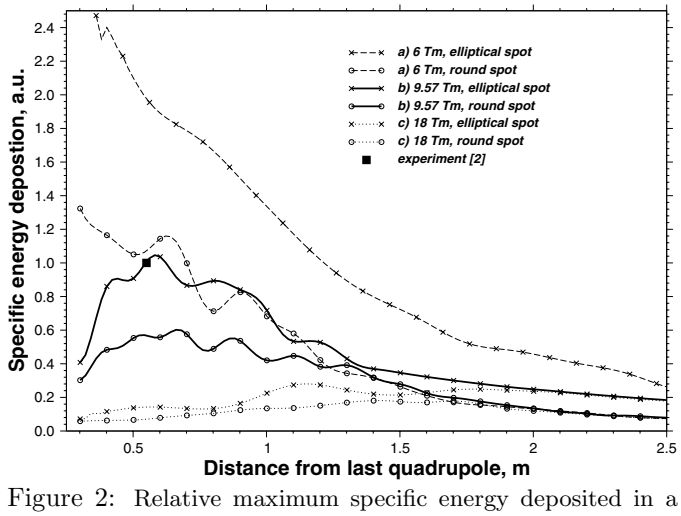


Figure 2: Relative maximum specific energy deposited in a target, recalculated from Fig. 1.

Assuming that the maximum specific energy deposited by the beam in a target material scales with the focal spot size as $E_s \propto S_S^{-2}$ and $E_s \propto (S_X S_Y)^{-1}$, this quantity is plotted in Fig. 2, relative to the value of experiment [2].

In conclusion, for the HED experiments at the HHT using the present final focusing system, a focal length of 40–90 cm and beam magnetic rigidities of 6–10 Tm are preferable. Since the level of energy deposition rapidly drops with increasing rigidity, for $\mathbf{U}^{28+}$ beam a stripper foil before the focusing system should be used. More advanced studies on the final focusing, taking into account high-order aberrations, chromatic effects, influence of the beam emittance and the stripper foil are planned.

## References

[1] M. Berz and J. Hoefkens, *COSY INFINITY Version 8.1 Programming Manual,* MSUHEP-20703, Michigan State University, 2002. URL: http://cosy.pa.msu.edu/.
[2] D. Varentsov et al., *Report on December 2003 Beamtime Experiment at HHT: Near-Critical HED States of Lead Generated by Intense Uranium Beam,* in this report.

# Charge Changing Collisions between Multiply Charged Ions

H. Bräuning, A. Diehl, A. Theiß, R. Traßl, E. Salzborn
Institut für Kernphysik, Justus-Liebig Universität, Giessen, Germany

Besides a general basic interest [1] cross sections for charge changing processes especially in homonuclear collision systems are also of great importance in plasma physics as well as fusion and accelerator research. In the latter case, attention must be given to possibly severe intensity losses due to the charge-changing collisions of ions within the beam pulses [2, 3]. A first measurement of the total loss cross section, which consists of the sum of the ionisation and the electron transfer cross section, for multiply charged ions in a homonuclear collision system has been performed by Kim and Janev [4] for $Ar^{3+}$ and $Kr^{3+}$ at a single center-of-mass energy of 60 keV.

The Giessen ion-ion experiment is ideally suited to study not only the total electron loss in such collision systems but also to distinguish between electron transfer and ionisation. We have already performed extensive measurements of the energy dependent cross section for electron transfer

$$X_1^{q+} + X_2^{q+} \rightarrow X_1^{(q-1)+} + X_2^{(q+1)+} \qquad (1)$$

and ionisation

$$X_1^{q+} + X_2^{q+} \rightarrow X_1^{q+} + X_2^{(q+1)+} + e^- \qquad (2)$$

for four-fold charged ions Ar, Kr, Xe, Pb and Bi [5, 6, 7] and for triply charged ions Ar, Kr and Xe [8]. We have now extended our studies towards charge exchange in collisions of doubly charged Ar and Kr ions. Fig. 1 and Fig. 2 show the measured cross sections in comparison with the earlier

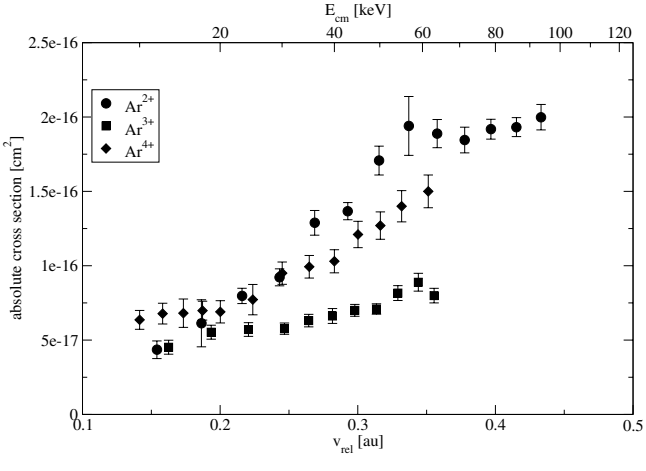


Figure 1: Absolute cross section for electron transfer in the collision system $Ar^{q+} + Ar^{q+}$ with $q = 2, 3, 4$.

data on triply and four-fold charged ions. As usually observed in non-resonant collision systems, the cross section is strongly dependent on the collision velocity. This dependence is less pronounced for the four-fold charged ions, especially at the very low velocities. We attribute this to a significant amount of metastable ions in the beam, which raises the cross section. Keeping this in mind, we see, that at least for the higher velocities, where the metastable contribution is less significant, the dependence of the cross

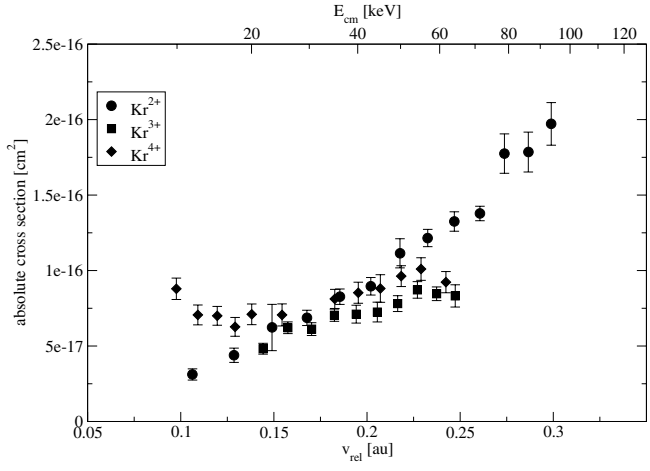


Figure 2: Absolute cross section for electron transfer in the collision system $Kr^{q+} + Kr^{q+}$ with $q = 2, 3, 4$.

section on the charge state is reflected in the Q-value (table 1) of the reaction. Collisions between triply charged ions have the highest negative Q-value and show the smallest cross section.

| | 2+ | 3+ | 4+ |
|---|---|---|---|
| Ar | -13.1 eV | -19.1 eV | -15.2 eV |
| Kr | -12.6 eV | -15.6 eV | -12.2 eV |

Table 1: Q-values for the electron transfer reaction $X^{q+} + X^{q+} \rightarrow X^{(q-1)+} + X^{(q+1)+} + Q$ according to spectroscopical data by C.E. Moore [9].

This work is supported by BMBF under contract no. 06 GI 150.

## References

[1] F. Melchert and E. Salzborn: Charge-changing ion-ion collisions, in The Physics of Electronic and Atomic Collisions, Proceedings of the XXI. ICPEAC, July 22-27, 1999, Sendai, Japan, edited by Y. Itikawa, AIP Conference Proceedings, No 500 (2000) 478.
[2] F. Melchert et al: Nucl. Instr. Meth. A278 (1989) 65
[3] D. Budicin et al: Il Nuovo Cimento 106A (1993) 1621
[4] H. Kim and R. Janev, Phys. Rev. Lett. 58 (1987) 1837.
[5] A. Diehl et al: J. Phys. B: At. Mol. Opt. Phys. 34 (2001) 4073.
[6] R. Trassl et al: Nucl. Instr. Meth. A 464 (2001) 80.
[7] H. Bräuning et al: Laser and Particle Beams 20 (2002) 493.
[8] H. Bräuning et al: Nucl. Instr. Meth. B 205 (2003) 555.
[9] C.E. Moore: Nat. Stand. Ref. Data Ser. - Nat. Bur. Stand. 34 (1970).

# Gas Excitation with High Perveance Electron Beams

J. Wieser[1], A. Morozov[2], R. Steinhübl[3], and A. Ulrich[2]
[1]TuiLaser; [2]TU-Muenchen; [3]Thales Electron Devices

A tabletop electron beam system has been set up to investigate beam excited dense gases at energy loads of up to several kJ/g. A high perveance electron beam is focussed down to a 1mm$^2$ spot size and sent through a thin ceramic foil into the target gas. Perveance is defined as I/V$^{3/2}$; space charge effects cannot be neglected at typically more than 0.1$\mu$A/V$^{3/2}$ [1]. Low acceleration voltages and high beam currents, focussed to a small spot, however, have to be used to achieve high stoppping values and excitation densities.

A 0.8A, 12keV electron beam, thus leading to 0.6$\mu$perv, focussed to 1mm$^2$, has been used for gas excitation. Power densities of several MW/g in 1bar Ar are achieved. Electron beam excitation is routinely used in large volume excimer lasers with electron energies ranging from 200keV to 2MeV. Here, the electron energy could be reduced by more than an order of magnitude. This has become possible by the enabling technology of extremely thin ceramic foils used as entrance windows for the electrons, as described in ref.[2]. Reducing the electron energy reduces the range of the electrons in the medium. This in turn increases the pumping power density for a given beam current. Energy deposition calculations for a 1A, 12keV gaussian beam with 1mm FWHM, focussed through a 300nm thick $SiN_x$ membrane into 1bar Ar gas, have been performed using the CASINO Monte-Carlo program [3]. Using 500ns beam pulses, a temperature increase of the membrane of 1500K would be expected, with an energy density in the gas peaking at 2.5J/cm$^3$, as is shown in Fig. 1. Note that the power density increases after the entrance foil due to higher stopping at lower electron energies, leading to an about fourfold increase of temperature a few hundred micrometer behind the entrance foil. Thus, temperatures up to 8000K would be expected under these excitation conditions.

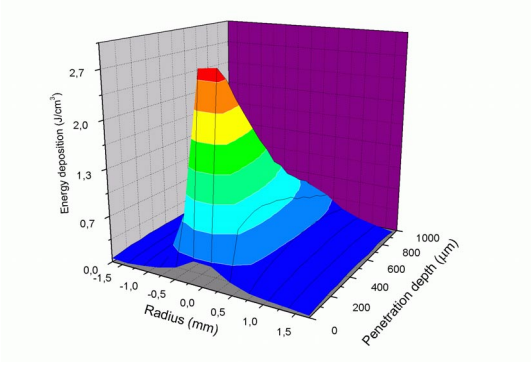


Figure 1: Energy deposition of a 500ns, 1A, 12keV electron beam focussed with a FWHM of 1mm through a 300nm $SiN_x$ membrane into 1bar of argon gas. Calculations have been perfomed using the CASINO software [3].

In a first experiment, up to 0.8A, 12keV electron beam pulses were sent through a square 1mm$^2$, 300nm thick silicon nitride foil into 600mbar argon gas. Rectangular pulses of 10, 20, and 50ns were applied to the extraction grid of the electron gun, using a cable pulser with a fast solid state switch. Wavelength spectra were recorded in the 110 to 200nm range with a gated, intensified diode-array camera. The spectra are dominated by the so called second excimer continuum (Fig.2).

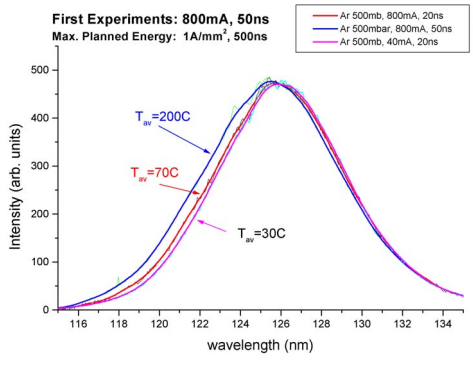


Figure 2: Electron beam excitation of Ar using three different energy loads. Average gas temperatures of 470K, 340K, and 300K, respectively, could be deduced from the width of the excimer continua.

Average gas temperature has been measured using the widths of the recorded excimer spectra ([5]). A maximum average gas temperature of 200 °C could be deduced for the 0.8A, 50ns beam pulse, while essentially no temperature increase was measured for the 40mA, 20ns beam pulse situation. Taking into account that the temperatures, measured, are mean temperatures, averaged over the entire excited volume, a good agreement between simulation and experiment was achieved.

In a next step, longer elctron beam pulses shall be applied, increasing the energy load and thus the temperature of the excited gas. In particular the transition between a cold recombination plasma, spectrally dominated by excimer radiation, and a hot regime, where excimer molecules can not be formed and thermal ionization is increasingly dominant, shall be studied.

Funding by Bayerische Forschungsstiftung Az482/01 and the support of Plasmaphysics Group GSI is greatfully acknowledged.

## References

[1] S.I. Molokovski and A.D. Suschkov, Intensive Elektronen und Ionenstrahlen, Vieweg Verlag, Braunschweig, 1999
[2] J. Wieser et al., Rev. Sci. Instrum. 68 (1997) 1360
[3] P.Drouin et al., CASINO, Univ. de Sherbrooke, Quebec, Canada
[4] S. Valkealahti et al., J. Appl. Phys. 65 (1989) 2258
[5] R. Prem, Diploma thesis, Technische Universität München, Fakultät für Physik E12, 1994

# Residual Radioactivity of Copper Induced by a High Energy Argon Beam

A. Fertman[1], A. Golubev[1], B. Sharkov[1], M. Prokouronov[2], G. Fehrenbacher[3], R.W. Hasse[3], D.H.H. Hoffmann[3,4], I. Hofmann[3], E. Mustafin[3], D. Schardt[3], K. Weyrich[4]

[1] ITEP Moscow, [2] RIPT Moscow; [3] GSI Darmstadt, [4] TU-Darmstadt, Institute of Nuclear Physics

The residual radioactivity produced by high energy heavy ions has been measured using the 300 MeV/u, 500 MeV/u and 800 MeV/u $^{40}$Ar ion beams of the Heavy Ion Synchrotron SIS-18 at GSI Darmstadt. This work is the continuation of the ion induced radioactivity experimental program, which was started at GSI in 2002, with copper and stainless steel irradiated by a carbon beam. [1]. The experimental set-up is presented in figure 1.

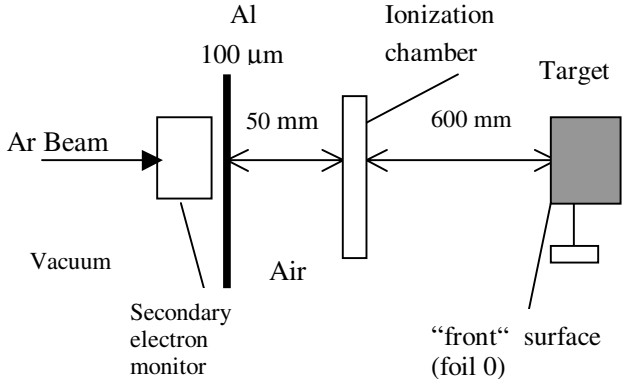


**Fig.1: Experimental set-up for coper target irradiation**

The beam extracted from the synchrotron has a time structure with a pulse width of 1 s at every 3.3 – 3.8 s time interval, depending on the beam energy. During the irradiation experiments the beam intensities were measured with a transmission-type ionization chamber, and a secondary electron monitor. Both these detectors were calibrated for argon ion beam measurements using a scintillator proportional counter. So, for example for 500 MeV/u argon, the number of ions propagating through the SEM detector is: $N = Q_{SEM}(pC)*0.970*10^6$.

The target diameter for all samples was 50 mm. The beam diameter was not larger then 11 mm. The thickness of the target was determined for each ion energy. It was two times larger than the range of the argon ions: 22 mm, 47 mm and 97 mm for 300, 500 and 800 MeV/u Ar-ions, respectively. Thus the beam is completely stopped in the target. One millimeter activation foils of copper were inserted in the target to measure the spatial distribution of residual nuclei in the target. Precise gamma-spectrometry measurements for element identification were carried out with a Canberra HpGe–GEM-45195-S-SV detector. Table 1 gives the residual nuclides measured in the activation targets. In comparison with the carbon irradiation experiment the list of residual nuclides is shorter and consists of 27 isotopes. Short-lived nuclides $^{41}$Ar, $^{44}$Sc, $^{56}$Mn and $^{61}$Co were not registered in the argon-irradiated samples, because the cooling time was increased.

In total, around 75 spectra were measured during one month after the end of the irradiation. Thus, from the irradiation experiments we identified the residual nuclei in all activation foils and obtained the spatial distribution of their activation rates in the copper targets along the ion range (Fig.2). This figure indicates that the spatial distributions of

**Table 1: Residual nuclides measured in the copper target**

| Projectile – target | Residual nuclides in activation target |
|---|---|
| $^{40}$Ar – Cu (nat) | $^{7}$Be, $^{22,24}$Na, $^{28}$Mg, $^{42,43}$K, $^{44M,46,47,48}$Sc, $^{48}$V, $^{48,51}$Cr, $^{52,54}$Mn, $^{52,59}$Fe, $^{55,56,57,58,60}$Co, $^{57}$Ni, $^{61}$Cu, $^{62,65}$Zn, $^{67}$Ga |

the activation rates of Co isotopes, which are close to those of the target consisting of natural Cu ($^{63}$Cu and $^{65}$Cu), increase with depth in the copper target, while the spatial distribution of $^{7}$Be, which has a much smaller mass than natural Cu has a constant distribution in the copper target up to the depth of the energy range of the incident beam. The spatial distribution of $^{46}$Sc exhibits an intermediate profile between those two. The character of the spatial distribution curves is similar to the results obtained by E. Kim et al. at HIMAC [2]. Furthermore the experimental results show that many radionuclides are produced in the target where the depth is beyond the energy range of the incident beam (47.74 mm). This production is initiated due to a large amount of secondary neutrons, protons and light fragments.

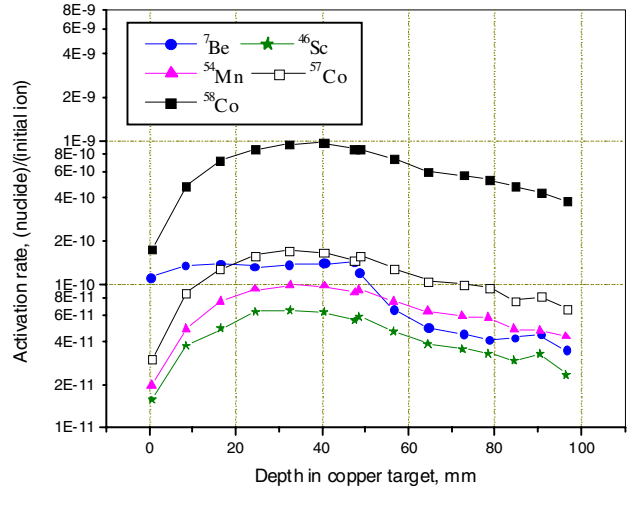


**Fig.2: Spatial distribution of activation rates of different nuclides in the copper target after $^{40}$Ar $E_0$=800MeV/u irradiation**

## References

[1] A. Fertman et al., GSI-2003-2 Report, September 2003

[2] E. Kim, Y. Uwamino, T. Nakamura, et al., Int. Conf. on Nucl. Data for Sci and Technol, May 19-24, 1997 Trieste, Italy

# Critical Assessment of Multistage Pseudospark Switches

Klaus Frank, Isfried Petzenhauser and Udo Blell*

Univ. Erlangen, * GSI Darmstadt

In repetitive pulsed power there is a strongly increasing demand for the development of high voltage pulse forming networks (PFN), which can be operated with high repetition rates and simultaneously extremely long lifetime. Typical applications for such PFNs are modulators for the next generation of accelerators, pulse generators for flue gas cleaning with electrostatic precipitators, high power gas lasers, accelerators for medical radiography and drivers of high power microwaves.

To meet the requirements of the projected SIS100/300 accelerator complex the PFN of the fast injection/extraction kicker system has to fulfill certain properties, such as:

| | |
|---|---|
| Peak voltage: | 100 kV |
| Peak current: | 10 kA |
| Pulse duration: | ≤ 12 µs |
| Charge transfer: | ~ 0,1 C |
| Repetition rate: | 4 Hz |

The kicker rise time has to be 100 ns or less. Therefore the current rise rate has to be $> 10^{11}$ A/s.

An important part of the PFN is the high-power switch. One possible switch type is the pseudospark switch. It combines a high rate of current rise ($>10^{11}$ A/s), low power consumption (no heated cathode), reasonable lifetime (depending on application typ. ~$10^8$ shots) and a 100% current reversibility.

Single stage PSS were commercially build and tested and the results are promising.

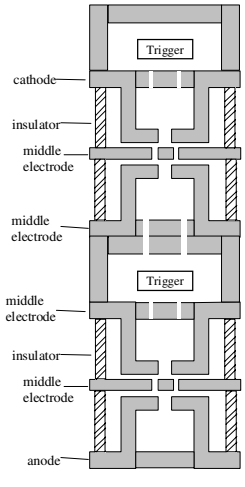


**Fig.: 1: Multistage switch design**

Prototypes of multistage pseudospark switches have been adopted for different purposes such as high voltages (65 kV) [1] and extremely low misfire rate [2].

A new switch was designed to meet the specified requirements. It is shown in Fig.: 1. The four gap design will allow voltages up to ~120 kV.

A critical part in every gas discharge switch is the trigger unit. This design uses two trigger. Other designs use 1 or 4 trigger units. The advantage of 1 unit is a small switch with low inductance but the disadvantage is a rather poor delay/jitter. With 4 trigger units it is possible to achieve a good delay/jitter but the switch is bigger (this leads to a higher inductance) and it needs more connections also on the high voltage side. The two trigger design will combine a fair delay/jitter with a fair size of the switch. Two different types of trigger units are under discussion. One is the glow discharge trigger. It uses an auxiliary glow discharge to provide charges that can be injected into the switch. The advantage are a nearly infinite lifetime and a low delay/jitter. The disadvantage is the power consumption, the size and the rather complicated external circuit. Further developments will solve these problems at least partly. The other possiblility is the high dielectric trigger. It used the electron emission from ferroelectrics to emit charges into the switch. The advantages are a low power consumption, a small size and an easy circuit. The disadvantage is a (compared to the glow discharge trigger) short lifetime especially in extreme working conditions. By a careful choice of the dielectric material and by protection measurements used to separate the main discharge and the trigger unit this problem will be solved.

All in all can be said, that pseudospark switches are a promising alternative to other high voltage switches such as thyratrons or semiconductor switches. They were tested for different applications and the results show a great potential of this switch also for the pulse forming network of the SIS100/300 kicker system.

## References

[1] J. Meier, ”Untersuchungen zum Schaltverhalten von zweistufigen Pseudofunken-schaltern und deren Eignung für Hochstromanwendungen”, Diplomarbeit, Universität Erlangen-Nürnberg, 1998

[2] L. Ducimetière et al. “Pseudospark Switch Development for the LHC Extraction Kicker Pulse Generator”, LHC Projekt Report 56 http://preprints.cern.ch/archive/electronic/cern/preprints/lhc/lhc-project-report-56.pdf

# The Z-pinch snowplow model revisited

A. R. Piriz, J. C. Sanchez Duque, O. D. Cortazar, R. F. Portugues

E. T. S. I. Industriales, Universidad de Castilla-La Mancha, Campus Universitario s/n, Ciudad Real, Spain.

Z-pinches are an excellent way to produce and confine high-temperature plasmas. These plasmas generate copious x-rays radiation that have numerous applications such as the lithography and microscopy, and also in inertial fusion for driving high-temperature radiation cavities (hohlraums). Z-pinch is formed by the implosion of a thin current sheath driven by the magnetic pressure. The current sheath is created on the inner surface of a cylindrical discharge tube of radius $r_0$ that separates the electrodes on which a large voltage is suddenly applied. The simplest way to describe the Z-pinch formation is by means of the snowplow model [1]. It has been widely used for the experimental design and, more recently, for the study of possible methods for stabilizing the hydrodynamic instabilities that affect the implosion of the current sheath and the final pinch uniformity. This model is able to predict quite accurately the implosion time but is inadequate for describing the motion of the preceding shock wave as well as the plasma behaviour after the pinch time. This is because it assumes that the magnetic piston and the shock wave launched into the internal gas are lumped together into a plasma shell of zero thickness. Later models aimed to overcome these shortcomings has been proposed along the time, but no-one has been able to predict the pinch time as accurately as the classical snowplow model [2,3]

We have developed a new model which combines the description of the magnetic piston given by the snowplow model with the slug model for the motion of the shock wave driven by the piston. In this way the model keeps the accuracy of the snowplow model in the prediction of the pinch time whilst it allows for the calculation of the plasma conditions at peak compression.

We have assumed the simplest situation in which the cylindrical current sheath has an initial radius $r_0$ (at $t=0$) and the implosion is driven by a time varying external current $I(t)$. The current sheath is imploded by the magnetic force $(\boldsymbol{J}\times\boldsymbol{B})/c$, where $\boldsymbol{J} = J_z \boldsymbol{e}_z$ is the current density and $\boldsymbol{B} = B_\theta \boldsymbol{e}_\theta$ is the magnetic field created by this current (c is the light speed, and $\boldsymbol{e}_z$ and $\boldsymbol{e}_\theta$ are the unit vectors in cylindrical coordinates). We describe the motion of the magnetic piston by means of a snowplow model and for this we assume that the total current $I(t)$ is concentrated in a thin shell close to the piston position $r_p(t)$.

We consider that a strong shock wave is launched into the internal gas due to the motion of the current sheath so that the kinetic pressure between the shock and the current sheath is $p_s = [2/(\gamma+1)]\rho_0 \dot{r}_s^2$ ($\rho_0$ is the initial density in the discharge tube, $\gamma = 5/3$). Then, we obtain the equation of motion of piston by integrating the fluid momentum conservation equation across the thickness of the current sheath:

$$\frac{d}{dt}\left[m(t)\frac{dr_p}{dt}\right] = -\frac{2I(t)^2}{c^2 r_p} + 2\pi r_p p_s \,, \quad m(t) = \rho_0 \pi (r_0^2 - r_0^2)$$

where $m(t)$ is the shell mass per unit of length and it is equal to the mass swept at the time $t$. It may be worth to notice that the term corresponding to the magnetic force here is a factor two larger than the force due to the magnetic pressure $B_\theta^2/8\pi$ usually considered in the classical snowplow model. Besides the previous equation includes the counter-pressure due to the plasma between the shell and the shock. The pressure $p_s$ depends of the shock motion and it can be described by the following slug model equation [2]:

$$\ddot{r}_s = -\frac{\gamma \dot{r}_s}{r_p^2 - r_s^2}\left(r_p \dot{r}_p - \frac{2}{\gamma+1} r_s \dot{r}_s\right)$$

where $r_s$ is the instantaneous position of the shock wave.

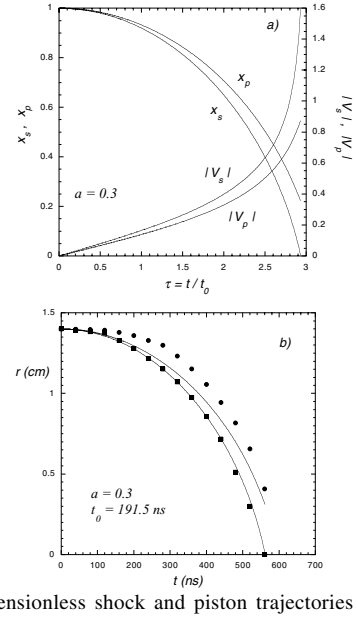


**Fig. 1** a) Dimensionless shock and piston trajectories and velocities for $a$=0.3. b) Shock and piston trajectories given by the model (full lines) and by the simulations of Ref.[4] (dots).

In Fig.1 we show the results of the model and comparisons with numerical simulations for $I = I_0 \sin(a\tau)$ and $a = 0.3$ ($\tau = t/t_0$, $a = 2\pi t_0/T$, $t_0 = (\rho_0 \pi r_0^4 c^2/2I_0^2)^{1/2}$, and $T$ is the period). From these results the model also allows for calculating the average density and temperature at peak compression in good agreement with the numerical simulations.

**References.**

[1] N. A. Krall and A. W. Trivelpiece. *Principles of Plasma Physics* (McGraw-Hill, Tokio, 1973)

[2] D. Potter. *Nucl. Fusion*. **18**, 813 (1978).

[3] T. Miyamoto, *Nucl. Fusion*. **42**, 337 (1984).

[4] K. T. Lee et al. *Phys. Plasmas* **3**, 1340 (1996).

# 2 BEAM TRANSPORT AND ACCELERATOR RESEARCH AND DEVELOPMENT

# High current electron source for beam neutralization experiments

V. Orsic Muthig [1], E. Dewald [2], D.H.H. Hoffmann [3,4], J.Jacoby[1], S. Krebs[4], J. Pozimski [1], U. Ratzinger [1], H. Riege [5], M. Schollmeier [4], A. Tauschwitz [3]

[1]JWG-Univ. Frankfurt, Germany; [2]LLNL, USA; [3]GSI, Germany; [4]TU Darmstadt, Germany; [5]CERN, Switzerland;

To investigate the space charge neutralization effects in the extraction gap of a laser ion source (LIS) [1] a high current density electron beam with low energy spread is needed. The transient hollow-cathode discharge (THCD) source [2] has the required characteristics. The THCD is a pulsed hollow-cathode glow discharge that operates at low gas pressure ($10^{-3}$- 1 mbar) and high applied voltage. Characteristic for this type of discharge is that during the fast voltage breakdown, discharge currents of several kA are reached. At the beginning of the current increase a high current, well focused electron beam is emitted at the anode. The unique feature of the THCD produced beam is its self-focused, space charge neutralized propagation in the background gas. At the beginning of its propagation the beam charge is only partially neutralized. We use the channel spark geometry (Fig. 1) which consists of a hollow cathode and a capillary tube made of $Al_2O_3$.

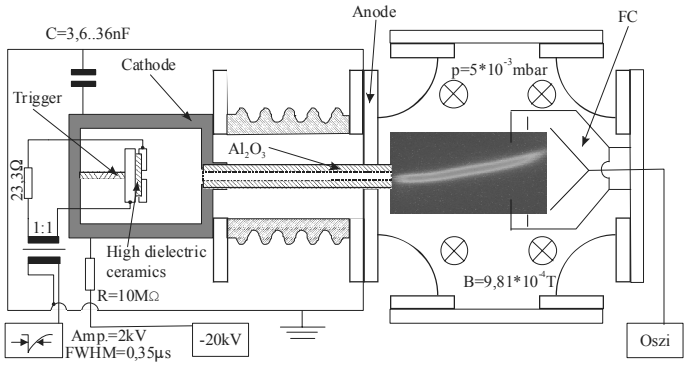


Fig. 1. Set-up of the high current electron source

The disk-shaped anode is mounted on the outer side of the capillary tube. Specific for this kind of discharge is the working gas pressure of $5*10^{-3}$ -$5*10^{-2}$ mbar. The cannel spark is operated by means of a trigger discharge placed in the hollow cathode region. For the operation of the trigger unit, which contains high dielectric ceramics (ε=2000), a pulse of 2kV amplitude and 0.35 µs FWHM is needed.

The electron current has been measured with a Faraday cup with a carbon collector. The shape and material of this collector are chosen to minimize emission of secondary electrons as well as the reflection of beam electrons [3]. To optimize the working pressure of the electron source we measured the beam current in the pressure range from $2.3*10^{-3}$ to $4.4*10^{-3}$mbar (Fig.2). In this pressure range the maximum current varies between 0.4kA and 1.6kA. We found the optimal pressure (measured in the vacuum chamber near the end of the capillary tube) to be $3.2*10^{-3}$mbar with a maximum current between 1.3 kA and 1.6 kA. Below $2.3*10^{-3}$ mbar the electron current is only several mA and above $4.4*10^{-3}$mbar no beam current was measured. We also investigated the dependency of the beam current and pulse shape on the discharged capacity. It has been found that the maximum current does not depend on the capacity and that the pulse length can be increased with the capacity.

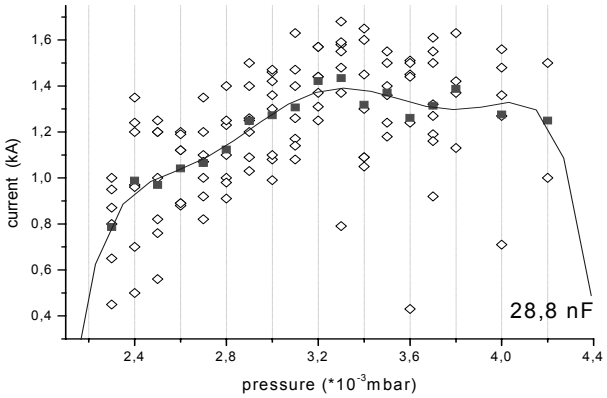


Fig. 2. Beam current depending on pressure in the vacuum chamber (◇-measuring points ■-mean value)

For the determination of the beam energy a homogenous magnetic field ($B=9.81*10^{-4}$T) created by a pair of Helmholtz coils is applied. We recorded the discharge channel of the beam with a gated CCD-camera (optical wave length) and the beam current with a Rogowski coil. The electron energy determines the bending of the beam (Fig.3, lines are

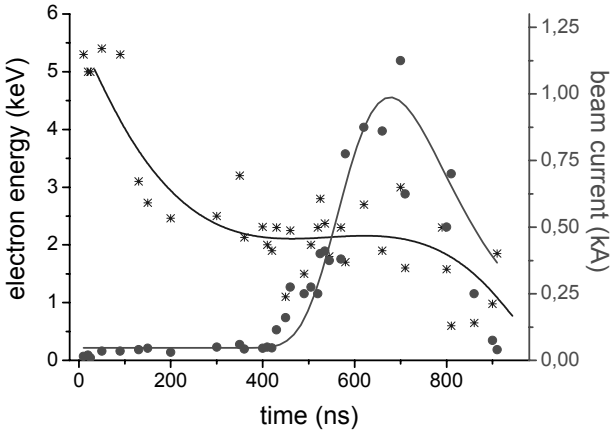


Fig. 3. Energy (crosses) und current (dots) of the electron beam

drawn to guide the eyes). The spread of the data points is caused by the fluctuation of the electron beam from shot to shot and by the error in the determination of the radius of curvature.

## References

[1] V. Orsic, et al. GSI-2002-7 Report (2002)

[2] E. Dewald, PhD Thesis Erlangen 1999

[3] J.A. Dayton, XIIIth ISDEIV,1998, Eindhoven, pp9-15

*Supported by DIP*

# Ion Beam Properties after Transport through an Extended Plasma Channel

R. Knobloch[1], S. Neff[1], A. Tauschwitz[2], and D.H.H. Hoffmann[1,2]

[1]Technische Universität Darmstadt; [2]Gesellschaft für Schwerionenforschung

Beam transport in plasma channels is a transport mechanism especially suited for the transport of high current beams or beams of poor quality (e.g. large momentum spread). It is currently studied as an alternative to ballistic focusing for final transport in ion beam driven inertial fusion reactors.

Plasma channels are created by a discharge in a background gas. The channels can be initiated either by laser heating of the gas along the axis or by sending an ion beam pulse through the gas-filled vessel before the discharge, which ionizes the gas on the axis.

The initial GSI experiments used a discharge chamber with a length of 50 cm. In 2003, the experimental setup has been refitted to accommodate a longer chamber to be able to produce longer plasma channels. A 50 cm extension tube was inserted. Within this extended chamber, 1 m long channels could be created. However, it became evident that the former design of having the chamber walls on one half of the cathode potential had to be improved, because the electric field strength on the axis in the longer chamber is very low with just one wall potential. Calculations showed that different potentials on the three wall parts increase the field strength [1]. Insulator flanges of 3 cm thickness and an array of resistors were included in order to set the three parts of the new chamber separately to different percentages of the full cathode potential. The resistors are used as potential dividers, so that the total voltage is divided evenly between the wall parts, see fig. 1.

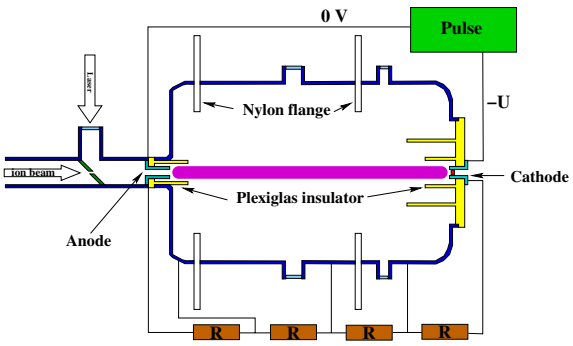


Figure 1: Schematic representation of the extended chamber

For ion beam initiated channels, different parameter ranges of voltage and gas pressure in the extended chamber were explored using several background gases: nitrogen, xenon, argon, neon, and krypton. These measurements were made with the extended chamber of 1 m length, but yet without the insulator flanges and thus without potential grading. From the side window, the light created by self emission of the plasma channel was observed by a CCD camera and a Gaussian fit was done over the image data. Background light in the chamber is mostly due to discharges across the insulators to the chamber walls. A high peak-to-background ratio of light intensity is thus a good indicator for a channel where little of the discharge current is lost over the walls.

The best channels were obtained with xenon at a pressure of 0.7-0.8 mbar and a voltage of 12.5-17.5 kV, see figure 2.

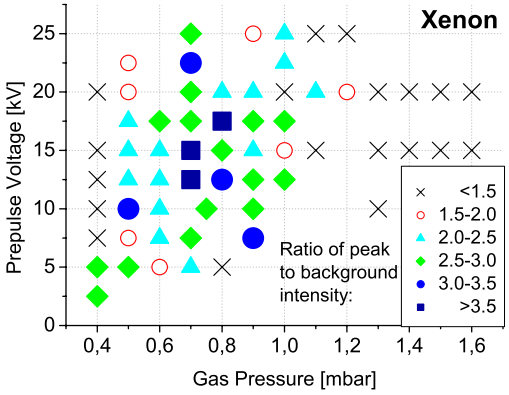


Figure 2: Parameter range for channels in xenon

In nitrogen, reasonably good channels could still be initiated at higher pressures, up to 1.5 mbar. Krypton showed ranges similar to xenon; the data analysis for argon and neon is still in progress, but preliminary results indicate that better transport channels can be created in higher-Z noble gases.

At the end of 2003, diagnostics for beam emittance measurements were included in the setup. A 50 $\mu$m thin copper foil with a grid of circular holes of 500 $\mu$m in diameter was built into the hollow cathode at the end of the discharge chamber. The beamlets shaped by these circular holes were then made visible on a plastic scintillator after several centimeters of drift space. The beam emittance $\varepsilon$ can be calculated from the data for each beamlet [2]:

$$\varepsilon \approx \frac{Rd}{2z}\left(\frac{D}{d} - \frac{Y}{y}\right) \qquad (1)$$

$R$ is the beam radius at the waist, $z$ the length of the drift space between pepperpot mask and scintillator. The other variables are shown in figure 3.

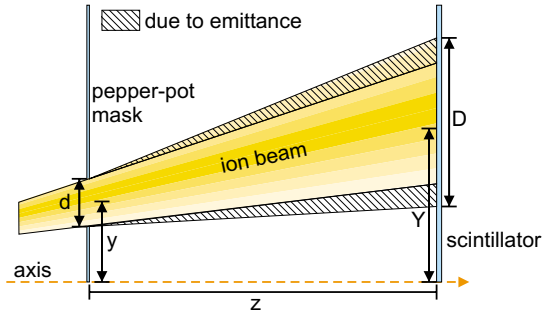


Figure 3: Emittance measurement

The analysis of the emittance data has started and will be continued in 2004; further measurements are planned.

## References

[1] S. Neff et al., *this annual report*

[2] J.G. Wang et al., *IEEE Transactions on Electron Devices* Vol. 37, No. 12, page 2622 (1990)

# Electrostatic Field Calculations for Plasma Channel Ion Beam Transport

S. Neff[1], R. Knobloch[1], A. Tauschwitz[2], and D.H.H. Hoffmann[1,2]

[1]Technische Universität Darmstadt; [2]Gesellschaft für Schwerionenforschung

Current inertial fusion reactor designs require heavy ion beams in the kiloampere range and beam diameters of less than a centimeter. The final transport of these beams is challenging, since no focusing magnets can be placed inside the reactor chamber. Plasma channels are a solution: they can easily be created by discharges inside the chamber and they possess an azimuthal magnetic field of up to several tesla. Calculations with a hybrid magnetohydrodynamics and particle-in-cell code have shown that the fields created by a 60 kA discharge are sufficient to transport the ion beams over several meters inside the channel[1]. Naturally, kiloampere heavy ion beams are not available yet. Therefore our experiments at the UNILAC accelerator facility at GSI do not take into account the large space-charge effects of a reactor beam. Nevertheless studies of the channel evolution and stability and proof-of-principle experiments regarding beam transport are possible. Our initial experiments used a 50 cm long chamber with a diameter of 60 cm[2]. Recently the chamber was prolonged to 1 m to be closer to the reactor parameters. This required electric field calculations to improve the chamber design.

The gas breakdown depends on the electric field, the gas pressure and the initial ionization of the gas. A breakdown to the metallic chamber walls can therefore be prevented by reducing the gas density on the axis (laser induced channels) or by ionizing the gas before the discharge (ion beam induced channels). However, these methods still require a reasonable field distribution in the chamber. Of particular importance for the breakdown is the minimum electric field on the axis.

Poisson, part of the Poisson/Superfish[3] software package from the Los Alamos National Laboratories, was used to calculate the electric field right before the start of the discharge. It uses the finite element method to solve the poisson equation

$$\Delta\phi = -\frac{\rho}{\epsilon_0\ \epsilon_r}. \qquad (1)$$

Since it is able to solve three dimensional problems with cylindrical symmetry, it is suited for our problem. Poisson requires

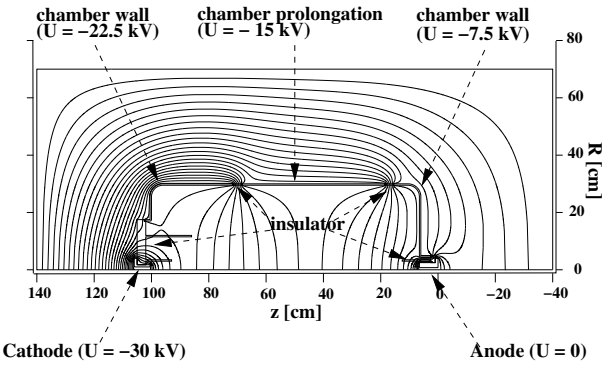


Figure 1: Chamber with calculated equipotential lines

a definition file with the problem geometry, material characteristics and fixed potentials. It uses the symmetry condition that the radial electric field vanishes on the axis and the boundary

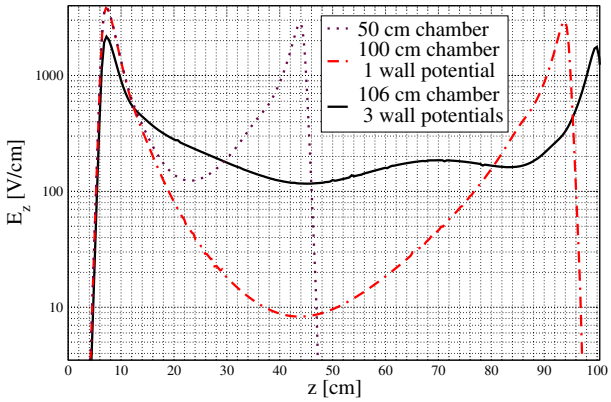


Figure 2: Calculated electric field on the symmetry axis (R = 0)

condition that the field perpendicular to the problem boundary is zero. Although this is strictly true only for a boundary at infinite distance from the electrodes, the thereby induced error for the field on the axis is negligible.

Figure 1 shows the calculated equipotential lines for the prolonged chamber. The three parts of the chamber wall are separated by two insulator rings, each having a width of 3 cm. This offers the possibility to apply a different voltage to each part. The cylindrical electrodes are located on the beam axis and are hollow. This allows the ion beam and the laser beam to enter the chamber through the electrodes. Furthermore it is possible to insert a scintillator into the cathode to analyze the beam. Two plexiglas insulators separate the electrodes from the walls.

Figure 2 shows the calculated electric field for three different setups: the 50 cm long chamber, the 1 m chamber and the optimized long chamber with three wall potentials. Figure 1 refers to the last case. All scenarios work with a cathode potential of -30 kV and an anode potential of 0 V. The chamber wall is set to -15 kV in the first two cases. In the last case, three separate voltages, -22.5 kV, -15.0 kV, and -7.5 kV, are used.

In the case of the short chamber, the minimum electric field on the axis is 124 V/cm (at $z = 23\,\mathrm{cm}$). It drops to 8 V/cm (at $z = 44\,\mathrm{cm}$) for the extended chamber. This is below the breakdown threshold of 60 V/cm for 5 mbar neutral xenon gas. While it is still possible to create discharges by lowering the gas density and ionizing the gas, breakdowns to the walls become more likely. In contrast, using three wall potentials yields a minimum electric field of 117 V/cm (at $z = 45\,\mathrm{cm}$). Furthermore the voltage between the electrodes and the adjacent parts of the wall becomes smaller, favouring the breakdown along the axis. This illustrates the usefulness of field calculations to test modifications of the experimental setup.

*This work is supported by the 'Graduiertenkolleg Physik und Technik von Beschleunigern'*

## References

[1] D.R. Welch et. al, *Phys. of Plasmas*, 9, 2344–2353 (2002).

[2] C. Niemann et al., *JAP*, 91, 617–623 (2002).

[3] http://laacg1.lanl.gov/laacg/services/possup.html

# Beam Injection Experiments using Space Charge Lenses

O. Meusel, J. Pozimski, A. Bechtold, A. Schempp and U. Ratzinger

Institut für Angewandte Physik der Johann Wolfgang Goethe-Universität D-60054 Frankfurt am Main

http://mikro1.physik.uni-frankfurt.de/Lebt/

Space charge lenses for ion beam focussing are in theory, especially for singly charged heavy ion beams at low velocities, superior to other lens systems [1]. On the other hand previous experiments [2] have shown, in contrary to the theoretical forecast, a small degree of lens filling and serious emittance growth. Newer experiments [3] demonstrated a much better degree of lens filling and substantially lower emittance growth. Therefore an injector to study the injection of a space charge dominated ion beam into an RFQ is under construction. The schematic layout of the experiment is shown in fig. 1. As reported previously [4] the ion source and LEBT system is operational, and the beam was matched to the injection point of the RFQ.

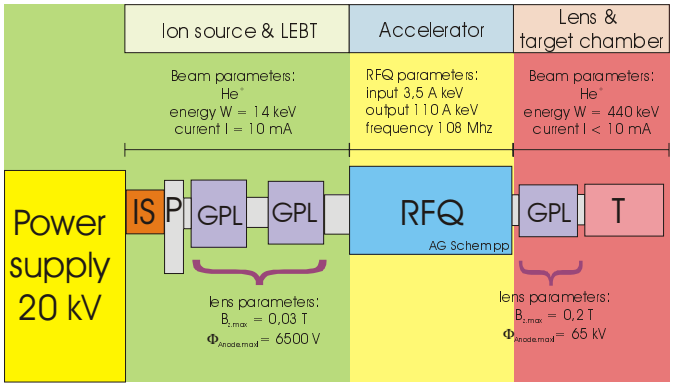


*Fig. 1:Schematic drawing of the experimental set up of Test injector 1. The LEBT system (green underlay) is operational and the experiments are finished, the injection into and acceleration in the RFQ (yellow underlay) is operational and under investigation and the final Focus and Target (red ) under completion and test.*

An existing RFQ [5] was implemented in this experiment. After low power tests and measurements of the RFQ-cavity (108 MHz, 25 dB) have been finished the tuner was installed and tested. Then the RFQ was successfully conditioned using high power RF levels (30 kW, duty cycle 2 %). The first experiments on beam injection into the RFQ and beam acceleration started in December 2003. For acceleration of $He^+$ the necessary design power is 8 kW. At this power level the accelerated beam current already reached 50 % of the current limit of the RFQ (0.7 mA·A/q). First beam profiles and emittance measurements as well as measurements of the beam energy and energy spread have already been performed and show satisfactory results and no significant deviation from the theoretical predictions. Further experiments for optimization of beam injection and improvements of the beam transmission are planned in the first months of 2004. After characterisation of the accelerated beam behind the RFQ the injector will be completed by the installation of the new high power space charge lens and the target chamber (already under vacuum). The large Gabor lens for the final focus into the target chamber has already been tested at high power ($U_A$=30 kV, $B_z$=0.1 T). First experiments on the investigation of the electron cloud have already started. The light emitted by the interaction between the space charge cloud and the residual gas has been observed. The radial light density profile was measured and a spectral analyses of the emitted light was performed to evaluate the temperature of the enclosed space charge cloud (see fig. 2). First beam tests using the new lens are planned for summer 2004. The experiments under preparation will concentrate on the space charge density distribution and on the degree of lens filling as well as on time dependent effects caused by the interaction of the space charge cloud with the beam pulses.

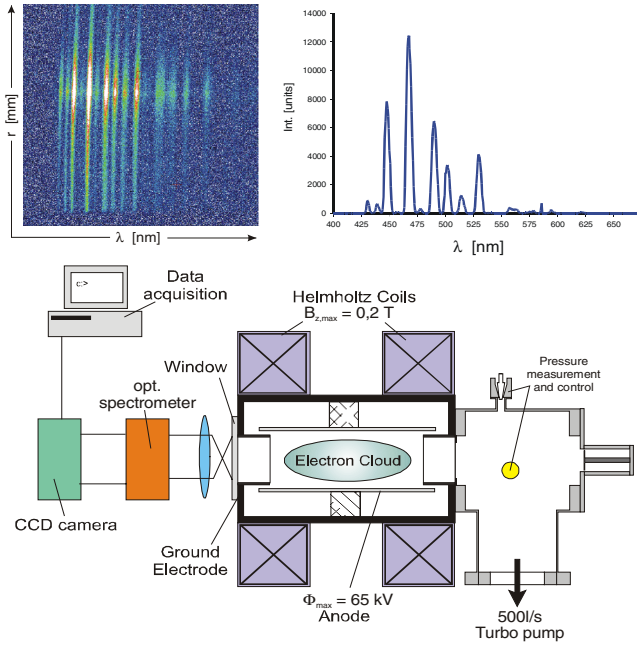


*Fig. 2: Picture of the new Gabor lens and optical spectrum of the light emitted by interaction between the space charge cloud and the residual gas.*

## References

[1] Reiser, Comparison of Gabor lens, gas focussing and electrostatic quadrupol focusing for low energy beams, Proc. PAC Conf. 1989, Chicago, USA

[2] J. A. Palkovic, Measurement on a Gabor lens for neutralising and focusing a 30 keV Proton beam, University of Wisconsin, Madison

[3] J. Pozimski, Untersuchungen zum Transport raumladungskompensierter, niederenergetischer und intensiver Ionenstrahlen mit einer Gabor Plasma-Linse, Dissertation IAP 1997.

[4] J. Pozimski, O. Meusel, Beam Injection studies Using a Gabor Lens, Annual Report GSI-2003-2, p.25

[5] A.Bechtold, Construction of an heavy ion RFQ accelerator with high duty cycle. Diploma thesis, IAP 1997.

# The Frankfurt Funneling Experiment

H. Zimmermann, U. Bartz, N. Müller, A. Schempp, J. Thibus

Institute of Applied Physics, J. W. Goethe-University, 60325 Frankfurt am Main, Germany

## 1. Introduction

New high current accelerator facilities like proposed for the HIDIF driver require beams with such high brilliance, which can not be produced by a single pass rf-linac. The increase in brightness in such a driver linac is done by several funneling stages at low energies, in which two identically bunched ion beams are combined to a single beam with twice the frequency, current and brightness, in the ideal case.

The Frankfurt funneling experiment is a set up of two ion sources, the Two-Beam-RFQ and a funneling deflector. It is a scaled model for the first funneling stage of a HIDIF driver, to demonstrate funneling of two ion beams.

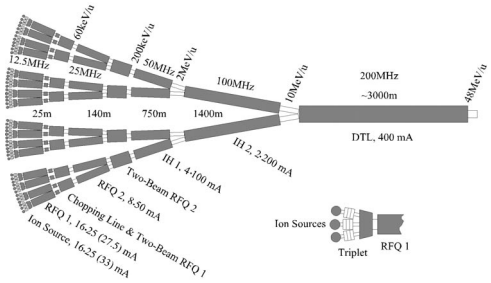


Fig. 1: Layout of the 12.5...200 MHz linac system for 400 mA of $Bi^+$.

## 2. The Two-Beam RFQ

The two-beam RFQ consists of two sets of quadrupole electrodes at an axis angle of 75 mrad, where the beams are bunched and accelerated with a phase shift of 180° between each bunch, driven by one resonator structure [1]. The electrode design of the RFQ is divided in two sections. The first section, which is about two thirds of the total length of 2 meters, accelerates the beam to a final energy of 40 keV/u. The last section has to match the beam to the funneling deflector to optimize beam radius and phase width. For first beam tests the last section consists of unmodulated electrodes. This allowed us to demonstrate the acceleration of two beams at the same time, but the beams were not matched to the funneling deflector. At present one beam axis consists of the original unmodulated electrode end part while the second one has an modulated electrode end part. This enables a comparison of both beams.

Fig. 2: Photo of the accelerating part of the RFQ, changing to the 3d focus end part. In the background beam line are still the unmodulated electrodes implemented.

The new design includes a rebunching section at the end of the electrodes of the RFQ. Figure 3a shows the interlaced beam pulses of the old and new electrode design with the same beam current from the LEBT's. The new electrodes show a higher beam current and a shorter pulse lengths. In figure 3b the pulses have the same current at the faraday cup. The pulses from the new elctrode design has a shorter pulse length.

The used faraday cup has a restricted bandwidth and cannot resolve the pulses at high resolution. But the results clearly indicate the improve matching to the funneling deflector.

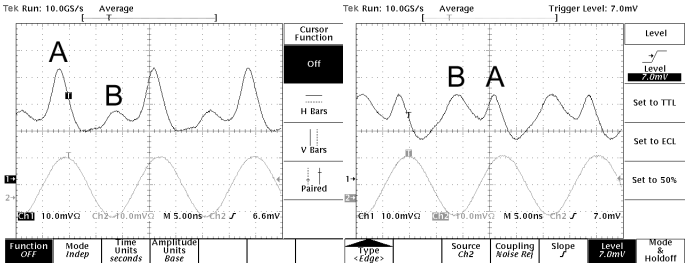


Fig. 3a,b: Interlaced beam pulse measurements with a faraday cup.
Fig. 3a: Same beam current from LEBT, Fig. 3b: Same current at faraday cup
A:Beamline with modulated electrode endpart, B: Beamline with unmodulated electrode endpart

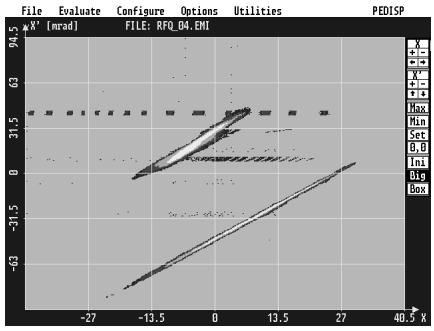


Fig. 4: Comparison of the old electrode endpart (bottom) with the new design (top). The new endpart reduces the beam radius for about 66 %.

## 3. Conclusions

Funneling has been demonstrated with both kind of funneling deflectors [2]. The last electrode endpart has shown the improvement to the funnel deflector. The electrodes of the second end part are now installed.

Next step will be funneling with the beams to investigate the emittance growth during funneling in details.

## References

[1] A. Schempp, Nucl. Instr. and Meth. A 415 (1998) p. 209

[2] H. Zimmermann et al, Proc. XX PAC 2003, Portland , USA (2003)

# High Current Accumulator Ring Study for Frankfurt University

M. Droba [1], U. Ratzinger [1], J. Maruhn [1]

[1]IAP, J. W. Goethe University Frankfurt, Germany

Closed toroidal field line systems have been used to confine pure electron plasmas, and more recently, magnetic surface configurations have become of interest as confinement devices for non-neutral plasmas [1],[2],[3]. Densities and magnetic fields of these experiments with respect to the Brillouin limit are in Fig.1.

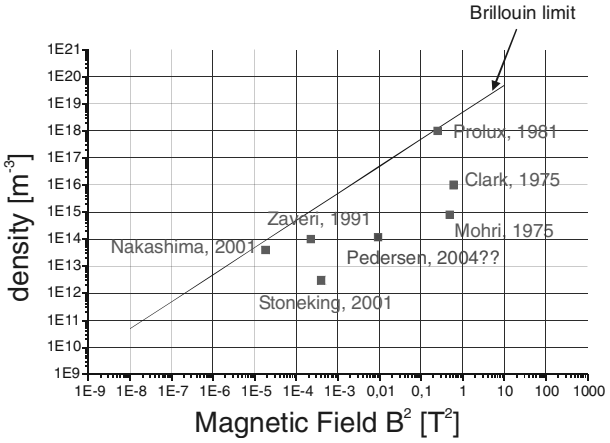


Fig.1.: Experimental data from the confinement of non-neutral plasmas in toroidal devices.

The stellarator configuration with closed magnetic surfaces seems to be convenient also for a magnetic confinement of high current beams. Numerical studies for a proton accumulator ring (*major radius R = 1 m, minor radius r = 0.25 m, B = 1 T, kinetic energy W = 150 keV, magnetic surface rotation parameter* $\iota < 2\pi$ *per turn*) were done in a single particle study at the beginning. Rotation of the magnetic surfaces enables a stable motion according to various drifts and their cancellation. Resulting drift surfaces (*particles with the same initial energy and input angle*) are displaced of about 2 cm against the geometrical axis (Fig. 2).

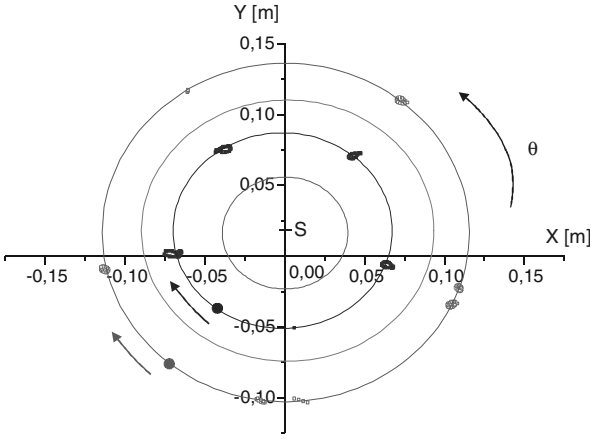


Fig. 2.: Drift surfaces in single particle model at an injection angle 0°.

The drift dynamics depends both on the magnitudes and the ratio of $v_\perp$ and $v_{||}$. Numerical results (Fig. 3.) indicate that kind of loss cone in phase space can be derived in the figure-eight stellarator.

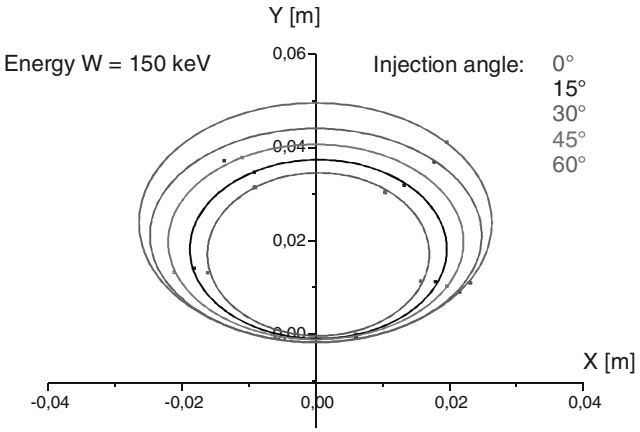


Fig. 3.: Drift surfaces for different input angles.

An overlap of individual drifts (curvature drift, grad B drift, ExB drift) complicate the particle motion. For an easier computation magnetic surfaces and adequate coordination systems have to be derived. The magnetic topology was computed by an application of the trace field line method on the parallel linux cluster of CSC (Center for Scientic Computing Frankfurt).

A next step will be to study the collective behaviour of high current beams in such devices. The equilibrium will be solved numerically from the Poisson equation (1) for magnetic surfaces.

$$\nabla^2\phi = \frac{e}{\varepsilon_0} N(\psi) \exp\left(\frac{e\phi}{T(\psi)}\right) \qquad (1)$$

($\psi$ denotes the magnetic surface parameter). The temperature is taken to be constant on a magnetic surface due to rapid thermalization along field lines. Here, the function $N(\psi)$ indirectly defines the density profile. The imaging charges have a strong influence on the beam profile in case of device with low aspect ratio ($\varepsilon$ = R/r ~ 1). Diocotron (density oscillation along the poloidal angle $\theta$) and ion-resonance instabilities should be avoided. Here the Landau damping effect could be helpful[4].

## References

[1] T. S. Pedersen et al., Numerical investigation of two-dimensional pure electron plasma equilibria on magnetic surfaces, Phys.of Plasmas 10, pp. 334-338, 2003

[2] A. Mohri et al., Formation of a Non-Neutral Relativistic-Electron-Beam Ring in a Toroidal Magnetic Field, Phys.Rev.Letters 34, pp. 574-577, 1975

[3] W. Clark et. al., Experiments on Electron Injection into a Toroidal Magnetic Field, Phys.Rev.Letters 37, pp. 592-595, 1976

[4] J. H. Yu et. al., Diocotron Wave Echoes in a Pure Electron Plasma, IEEE Trans. on plasma sci. 30, 1, 2002

# Radio-frequency gas discharge plasma confined in a magnetic quadrupole field*

M. Iberler, R. Berezov, J. Jacoby, Ch. Teske

Inst. für Angewandte Physik, J.W.Goethe-Universität, D-60325 Frankfurt/Main, Germany

Subject of this report is a new kind of a high frequency gas discharge plasma based on an electrode less configuration similar to a helicon discharge. In this radio-frequency plasma the confinement is caused by the focussing and defocusing force acting by the magnetic field on the electrons due to the alternating electron movement during the discharge. A main advantage of this new discharge is the electrodeless configuration of the discharge with inductive energy coupling, which minimizes the impurities from the electrodes and the gas tube wall. Figure 1 shows a schematic drawing as a side view. Shown are the magnetic poles oft the quadrupole with field configuration, the Rf-coil and the focused plasma [1].

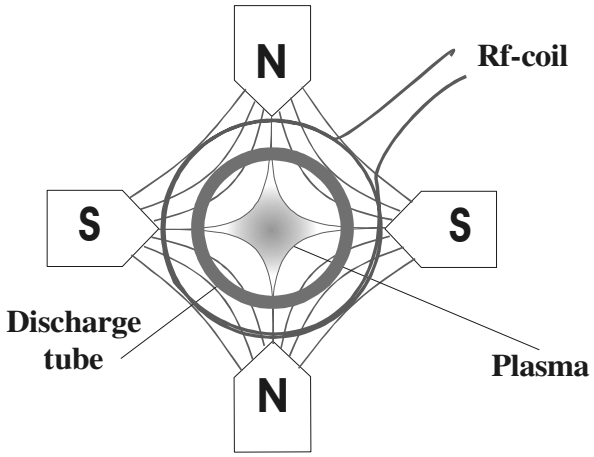


Fig.: 1 Schematic drawing of the used configuration.

At the present state of the work via a capacitive matching network, up to 600 W can be coupled into the antenna (Rf-coil). The inductive coupled plasma is run in a CW mode [2].

In this magnetic configuration the radial time independent magnetic field is introduced to the alternating plasma current. The plasma was generated in a RF plasma apparatus called Radio Frequency Quadropole. The main section of this experimental set-up is a glass discharge tube of about 21 mm inner diameter wrapped with a radial field coil, which produces a non uniform and time dependent magnetic- and electric field. The inductive coupled plasma is run in a CW mode. This described set-up is embedded in a permanent quadropol magnetic field, with a field strength tuneable from 0 to 2 T. The bias pressure of the discharge tube was in the range of $10^{-7}$ Pa and than filled with argon at a pressure in the range from 0.5-1.5 Pa. Figure 2 shows the shape of the plasma with for pronounced edges at the poles of the magnetic fields. The size of the plasma shape is strongly dependent on the high frequency power input and the gas pressure.

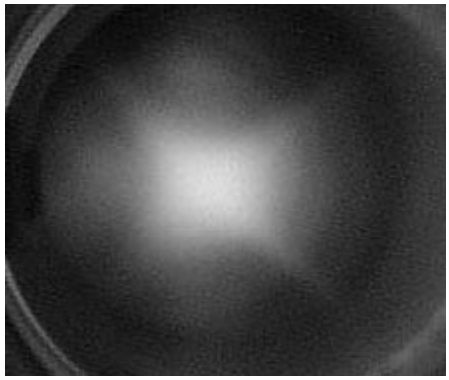

Fig.: 2 Shape of the confined plasma.

We are studying the plasma parameter of argon depending on the radial magnetic quadrupole field, gas pressure and the plasma power input [2]. The advantage of this system is the homogenous and dense plasma within a small volume.

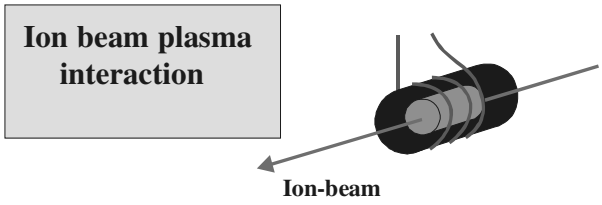


Fig.: 3: Sketch of the ion beam interaction with the cylindrical plasma

Further investigations are proposed in the field of heavy ion interaction with a dense rf-plasma (Figure 3). It is planned to study the energy losses and energy deposition of heavy ion beams for various plasma targets with different ionisations states, temperature and density. For this experiment a cylindrical time independent plasma target experiment is proposed to the ion beam target interaction to achieve a gas temperature in the range of several eV and high gas pressures.

## References

[1] J. Christiansen et al., “High-frequency discharge gas-laser embedded in a magnetic multipole field”, Patent pending, Aktenzeichen 199 30 755.5, München 1999.

[2] Peiyuan Zhu, R.W. Boswell, “A new argon-ion laser based on an electrodeless plasma”, Journal of applied Physics, 68, No 5, September 1990.

[3] William B. Bridges, Arthur N. Chester, A. Stevens Halsted, Jerald V. Parker, “Ion Laser Plasma”, Proceedings of the IEEE, Vol. 59, No 5, May 1971.

* this work is supported by the BMBF under contract F-130

# Interference experiment with elastic scattering of entangled electrons

V. Arsov, R. Berezov, J. Jacoby

IAP, JWG- Universität Frankfurt am Main, Robert-Mayer-Str. 2-4, D-60325 Frankfurt am Main

The scattering of electrons on electrons is a basic interaction process in plasma physics. By starting from binary collisions several many body processes like stopping power and strongly coupled plasmas are modeled. Furthermore, elastic scattering reveals fundamental quantum mechanical properties:

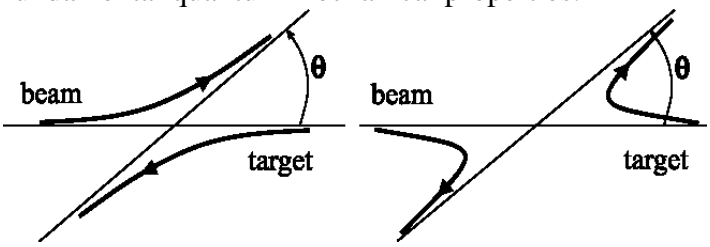


Fig. 1: The scattering cross-section for a fixed angle Θ has two components referring to the beam and to the target [1]. If the two scattered particles are indistinguishable entanglement appears.

The present experiment is performed with electrons, scattered elastically from a target (Figure 1). In this case interference appears, when the two scattered particles are indistinguishable. For identical fermions scattering to $\Theta = \pi/2$ is forbidden, whereas for identical bosons the scattering cross-section at that angle is twice as big as the one for distinguishable particles [2]. Therefore scattering of electrons to $\Theta = \pi/2$ is only permitted for distinguishable electrons, where the spin orientation for both scattered electrons is anti-correlated.

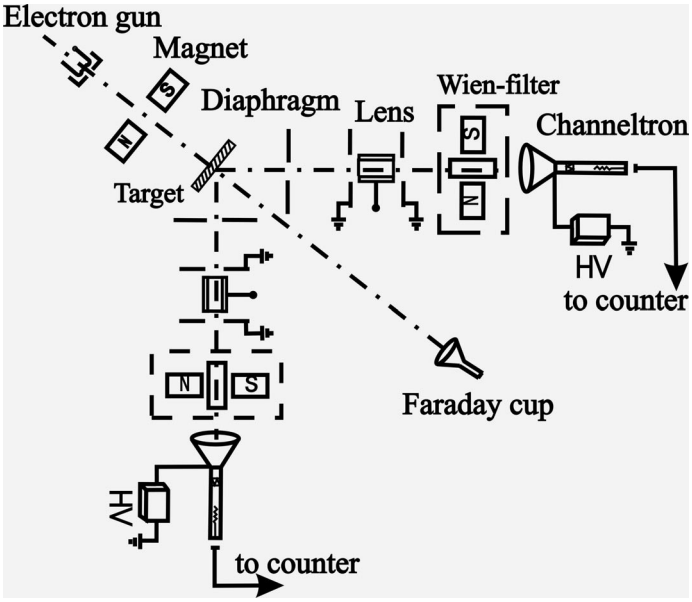


Fig. 2: Setup for the elastic scattering experiment of electrons on electrons.

The setup for the Moeller scattering experiment is sketched in Figure 2. The vacuum pressure in the chamber is $5 \cdot 10^{-7}$ mbar. The 10 keV electron beam is produced by a commercially available electron tube. The beam current can be varied between 10 and 50 μA and is stabilized dynamically at the desired value. The energy and the focus of the beam are adjusted manually. The spatial position of the beam is controlled by two pairs of coils. A C-target with about 10 $\mu g/cm^2$ is used for electron scattering. The beam current is measured behind the target and at ±45° towards the incidence direction with a faraday cup or with an electron multiplier. The latter is used for detection of single electrons. Coincidences are detected by a set of NIM-modules. Higher beam intensity on the detector is achieved by the use of single lenses. Wien-filters are used for separation of the Moeller component from the Mott one.

The first part of the experiment is spin unresolved. Its aim is to achieve time correlation in the two branches of the chamber. The main difficulty is to overcome the instabilities of the electron beam and the detection efficiency of the channeltrons, as well as to resolve the influence of the residual gas on the signal. Even small impurities can lead to false counts. Prerequisite for low background is the use of oil free pumps as well as getters on the side the electron gun and the channeltrons. Even when the vacuum is free of oil and water vapor, which is achieved either by heating of the setup or by using of cryogenic traps, the rest gas ions remain a problem. The construction of additional screens in front of the channeltron didn't solve it. For this reason a new construction of the channeltron is foreseen, which would prevent the drift of low energy ions towards the detector. Concerning the stability of the electron beam tests of alternative gun constructions are proposed. Prototypes of such guns are already available.

## References

[1] T. Mayer-Kuckuk, Kernphysik, Stuttgart, ISBN 3-519-23021-6 (1979)

[2] J. Jacoby, Which path information and coherence of elastic scattering, Phys. Scripta Vol. 64, 220-225 (2001)

# 3 TARGET THEORY

## 3.1 Properties of Dense Plasma

## 3.2 Instabilities in Beam-Plasma-Interaction

## 3.3 Heavy Ion Target Simulations

## 3.4 Beam Transport in Dense Plasmas

## 3.5 Short-pulse Laser-Matter-Interaction

# EOS of helium and hydrogen and its application to astrophysics

Volker Schwarz, Hauke Juranek, Nadine Nettelmann, and Ronald Redmer
Universität Rostock, FB Physik, 18051 Rostock, Germany

With the shock compression experiments in the Mbar regime [1, 2, 3] extensive investigations were performed on the equation of state (EOS) for hydrogen. One major application of this EOS is the modelling of gaseous planets like Jupiter. These planets consist basically of hydrogen and helium. We extended our chemical models, developed earlier [4], to a hydrogen-helium mixture.

For a typical fraction of 15% of helium in a hydrogen-helium mixture we show the pressure isotherms in Fig. 1. The effect of helium is to be seen at larger densities above 1 g/cm$^3$. The model is based on fluid variational theory (FVT) using effective pair potentials [4]. We extended this model to a three-component model for the species hydrogen atom and molecule and helium atom [5].

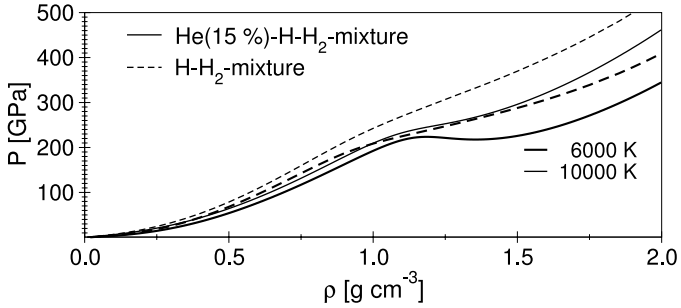


Figure 1: Pressure isotherms for a helium (15%)-hydrogen mixture in comparison to those of pure hydrogen plotted versus the total density.

For the hydrogen EOS we succeeded in calculating ionisation degrees by introducing a density-dependent partition function according to [6]. In Fig. 2 the mass fractions for the considered species of atoms, molecules and ions are plotted for 10000 K versus the density. We used FVT [7] for the atoms and molecules together with the density dependent partition function for the atoms and combined it with Padé approximations [8] for the electrons and protons of a fully ionized plasma.

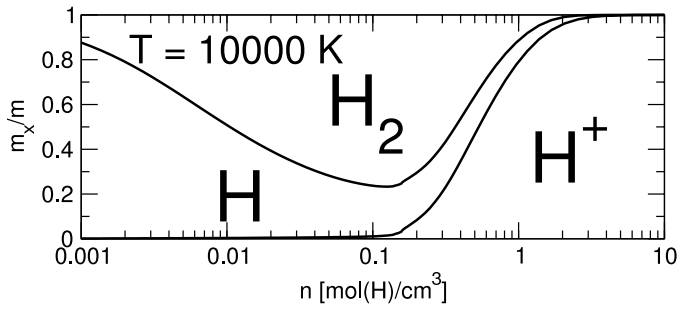


Figure 2: Mass fractions of the hydrogen species shown for 10000 K versus the molar (total proton) density; $m_{H^+} + m_H + m_{H_2} = m$.

This hydrogen EOS was applied to model the giant planet Jupiter assuming constant entropy, see [9]. In Fig. 3 we compare the mass distribution alond the radius for an ideal gas with the FVT/Padé results and the Sesame EOS [6]. The ideal gas model reproduces already the real Jupiter radius of 11.2 Earth masses within 4%. The FVT/Padé and Sesame models lead to 18% and 22% too large radii, respectively. These results are consistent with the missing fraction of 15% of helium in the pure hydrogen EOS.

Our future research goals are the EOS of helium-hydrogen mixtures that consider ionisation of hydrogen and in addition helium. The EOS will be supplied to more sophisticated planetary models. As a first step, the planet is assumed to consist of pure hydrogen. Its internal structure is governd by the equation of hydrostatic equilibrium without rotation, which was integrated along an isentrope. The temperature of the 1 bar level as well as the totel mass have been chosen to match the observed Jupiter data, resulting in mass-radius relations for different EOS as shown in figure 3. They reflect the increase and decrease of pressure due to the neglection of interactions (Ideal gas) and ionization (FVT), respectivly.

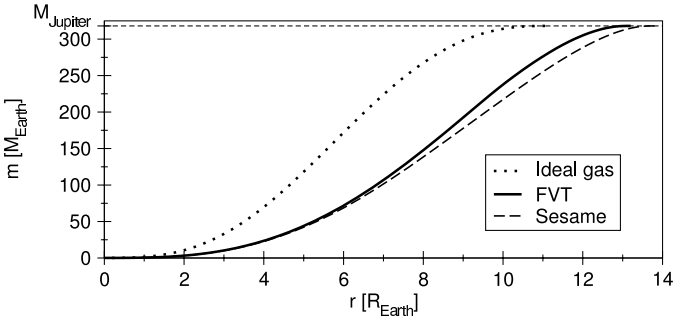


Figure 3: Mass of Jupiter along the radius r using different EOS.

## References

[1] G. W. Collins *et al.*, Science **281**, 1178 (1998).
[2] A. N. Mostovych *et al.*, Physics of Plasmas **8**, 2281 (2001).
[3] M. D. Knudson *et al.*, Phys. Rev. Lett. **90**, 035505 (2003).
[4] H. Juranek and R. Redmer, J. Chem. Phys. **112**, 3780 (2000).
[5] R. Redmer, H. Juranek, S. Kuhlbrodt, and V. Schwarz, Z. Phys. Chem. **217**, 782 (2003).
[6] G. I. Kerley, Technical Report No. LA-4776, UC-34, Los Alamos Scientific Laboratory, (1972).
[7] H. Juranek, R. Redmer, and Y. Rosenfeld, J. Chem. Phys. **117**, 1768 (2002).
[8] W. Stolzmann and T. Blöcker, Astron. Astrophys. **361**, 1152 (2000).
[9] T. Guillot, Science **286**, 72 (1999).

# Equation of state for weakly coupled quantum plasmas

J. Vorberger, M. Schlanges, W.D. Kraeft
Institut für Physik der Ernst-Moritz-Arndt-Universität Greifswald, 17487 Greifswald, Germany

Starting from quantum statistical theory [1] we establish a perturbation expansion for the equation of state of a quantum plasma in terms of the dynamically screened potential. In order to describe two component plasmas of any degeneracy, we restrict ourselves to systems of weak coupling and take into account terms up to order $e^4$ [2].

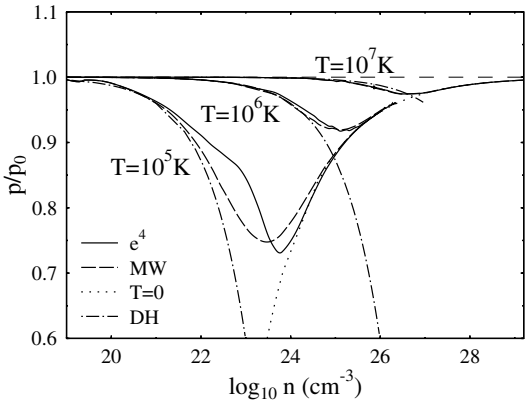


Figure 1: Isotherms of the pressure of an electron gas in units of the ideal pressure as function of the number density in different approximations.

Results for an electron gas are shown in figure 1. DH means the classical Debye–Hueckel correction, MW takes into account Hartree-Fock (HF) and Montroll-Ward (MW) terms, and the $e^4$ curve additionally accounts for exchange effects of order $e^4$ and represents the full expansion up to this order. The minimum behavior of the lines at intermediate density is due to nonideality effects. At higher and lower densities the curves approach unity what is caused by degeneracy effects at high densities and by large interparticle distances at low densities.

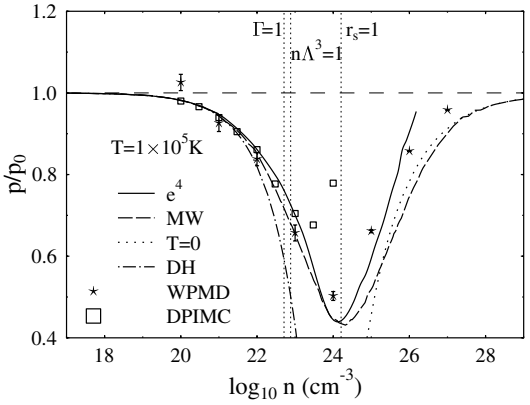


Figure 2: Pressure of a fully ionized hydrogen plasma in units of the ideal pressure as function of the number density at a temperature of $T = 10^5 K$ in different approximations. WPMD data from [3], DPIMC data from [4].

The pressure of fully ionized hydrogen can be seen in figure 2. The curves for hydrogen show, in principle, the same behavior as the curves in figure 1. We compare our results with results from first principle numerical simulations: Direct Path Integral Monte Carlo [4] and Wave Packet Molecular Dynamics [5]. As can be seen in this figure, at lower densities the agreement between the results is rather good. The results for depth and exact location of the pressure minimum strongly depend on the technique and thus on the approximation used.

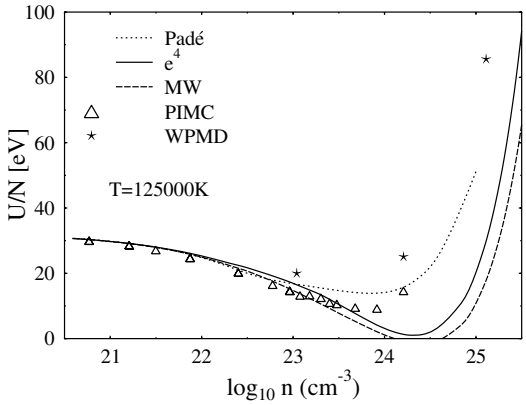


Figure 3: Internal energy of a fully ionized hydrogen plasma as function of the number density $n$ at a temperature of $T = 1.25 \times 10^5 K$ in different techniques. WPMD data from [5], PIMC data from [6]. Padé means a Padé formula [1].

Nearly the same situation can be observed in figure 3 where the internal energy for hydrogen is shown. At intermediate and higher densities, where the coupling parameter becomes equal to or larger than unity strong electron–proton and proton–proton correlations occur. These correlations are not included in our approach.

## References

[1] W.D. Kraeft, D. Kremp, W. Ebeling and G. Röpke, Quantum Statistics of Charged Particle Systems, Akademie–Verlag, Berlin (1986).

[2] J. Vorberger, M. Schlanges, W.D. Kraeft, Phys. Rev. E, accepted for publication.

[3] M. Knaup, private communication.

[4] V.S. Filinov, M. Bonitz, W. Ebeling, V.E. Fortov, Plasma Phys. Control. Fusion **43**, 743 (2001); V.S. Filinov, private communication.

[5] M. Knaup, P.-G. Reinhard, C. Toepffer, Contr. Plas. Phys. **41**, 159 (2001)

[6] B. Militzer, PhD, University of Illinois, Urbana, 2000; B. Militzer, D.M. Ceperley, Phys. Rev. E **63**, 066404 (2001).

# Conductivity and Reflectivity in Xenon Plasma

H. Reinholz, S. Kuhlbrodt, R. Redmer, G. Röpke
Universität Rostock, FB Physik, 18051 Rostock

Conductivity and reflectivity measurements on dense xenon plasma have been obtained by various groups and have been interpreted on the basis of a consistent approach to thermodynamic and transport properties using equilibrium Green functions and related correlation functions.

Xenon under the conditions considered is a partially ionized plasma (PIP). The composition has been calculated applying a system of coupled mass action laws [1], the so called PIP model. Three ionization stages have been taken into account which is an acceptable approximation for temperatures up to 40 000 K and densities below 4.5 g cm$^{-3}$. The composition for a density of 1 g cm$^{-3}$ is shown in Fig. 1. The conductivity has been calculated within a

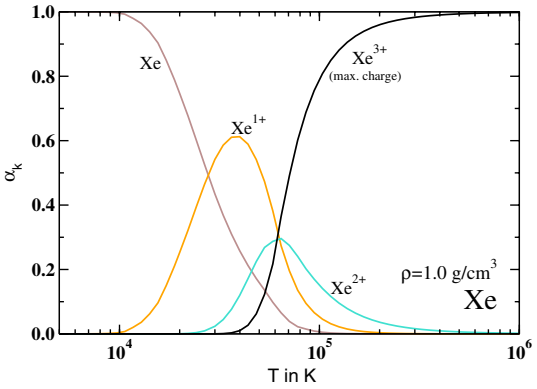


Figure 1: Composition of xenon in dependence of temperature at fixed density $\rho = 1$ g cm$^{-3}$ [2]

generalized linear response theory [1] which allows a systematic quantum statistical treatment. Fig. 2 shows the conductivity for different temperatures in comparison to measurements done in single or multiple shock compressed plasmas. For temperatures below 25 000 K, the conductivity shows a pronounced minimum due to partial ionization. The latter causes additional scattering on bound states and a reduction of free charge carriers.

Partial ionization would lead to a modification of the reflection coefficient as well. However, at the temperatures of about 30 000 K where measurement, see Fig. 3, have been done the contribution of the neutral component to the conductivity is small and was neglected.

Calculations assuming a sharp shock wave front are shown in Fig. 3. The reflectivtiy is calculated using a Drude model with a static collision frequency. No satisfying agreement can be found. Replacing the static collision frequency by a dynamical one leads only to small changes [3] and will not improve this discrepancy. In order to infer plasma parameters from optical reflection coefficient measurements of dense xenon plasmas, we propose a width of the shock wave front which was determined to be in the order of $\mu$m . A double linear profile has been considered [4], and the reflectivity can be obtained by solving the Helmholtz equation. The dielectric function is determined via a Drude formula where the static collision frequency is based on an interpolation formula for the dc conductivity. Results are shown in Fig. 3.

The experimental values of the reflectivity at different frequencies allow to determine the density profile. Instead of step-like density profiles which are not able to explain the measured reflectivities, smooth density profiles were considered. The gradient of the density profile is higher for higher densities, i. e. closer to the shock wave front. In order to explain the smooth density profiles, the propagation of a shock wave should be considered within a non–equilibrium approach containing ionization and compression processes.

## References

[1] S. Kuhlbrodt, R. Redmer, Phys. Rev. E **62**, 7191 (2004)
[2] S. Kuhlbrodt, Dissertation, Rostock 2003
[3] H. Reinholz, G. Röpke, A. Wierling, V. B. Mintsev, V. K. Gryaznov, Contrib. Plasma Phys. **43**, 3 (2003)
[4] H. Reinholz, Yu. Zaporoghets, V. Mintsev, V. Fortov, G. Röpke, Phys. Rev. E **68**, 036403 (2003)

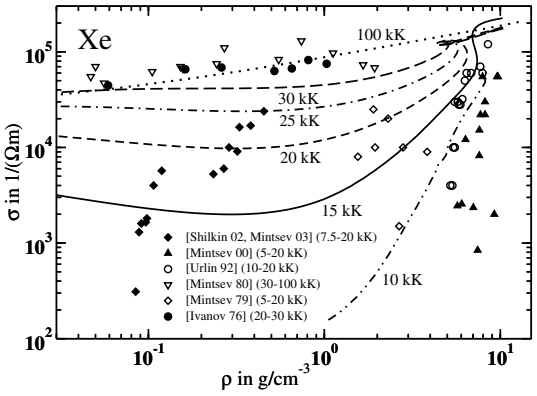


Figure 2: Comparison of experimental results and calculations for the dc conductivity of xenon plasma [2]

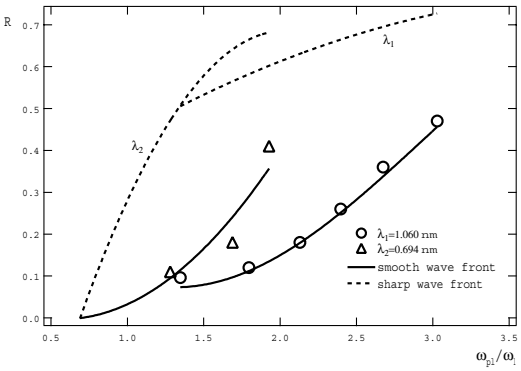


Figure 3: Comparison of experimental results and calculations for the reflctivity of xenon plasma [4]

# WPMD Simulations for the Conductivity of Warm Dense Hydrogen

B. Jakob, T. Pschiwul, P.-G. Reinhard, C. Toepffer, G. Zwicknagel
Institut für Theoretische Physik II, Universität Erlangen

We investigate the conductivity of hydrogen under extreme condition with "Wave Packet Molecular Dynamics" (WPMD) simulations [1]. The WPMD method describes the electrons as antisymmetrized Gaussian wave packets with a variable width for each particle. It thus allows to take into account many body quantum effects. In this method it is possible to calculate systems in a wide range of temperatures and densities.

The possible existence of a metallic phase in warm dense hydrogen has been discussed since long times [2, 3, 4]. A central observable is the conductivity. Here we present some first results on the dynamic longitudinal conductivity $\sigma_\parallel(k,\omega)$ as evaluated from WPMD simulations via the current-current-autocorrelation, according to

$$\Re\left[\sigma_\parallel(k,\omega)\right] \;=\; \frac{1}{2Vk^2k_\mathrm{B}T}\int_{-\infty}^{\infty}\mathrm{d}t\; e^{i\omega t}\;\langle \mathbf{k}\cdot\mathbf{J}_\mathbf{k}(t)\;\mathbf{k}\cdot\mathbf{J}_{-\mathbf{k}}(0)\rangle$$

where the current density $\mathbf{J}_\mathbf{k}$ is given by

$$\mathbf{J}_\mathbf{k} \;:=\; \sum_\alpha \mathbf{v}_\alpha \exp\left(-i\,\mathbf{k}\cdot\mathbf{v}_\alpha(t)\right) \qquad .$$

For first tests in the WPMD calculations of the dynamic conductivity we neglect the antisymmetrization. Instead we focus on the effects related to the time dependent width which is one of the essential ingredients of the WPMD method.

The Figures show two examples for the dynamic conductivity $\sigma_\parallel(k,\omega)$ of hydrogen at different plasma parameters $\Gamma$ and wave numbers $k$ (in units of the inverse Debye length $\lambda_\mathrm{D}$) and a degree of degeneracy $\theta_\mathrm{e} = k_\mathrm{B}T/E_\mathrm{F} = 6.96$. The curves are the result from the WPMD method with variable time dependent width for the wave packets, the points are calculations where the widths are fixed to the mean value of the widths as calculated during the corresponding run with variable width.

In the weakly coupled system ($\Gamma = 0.5$) there are no differences between both cases within the numerical fluctuations. But for stronger coupling ($\Gamma = 2$) deviations show up at frequencies larger than the plasma frequency $\omega_\mathrm{P,e}$. In this case the fluctuating width of the wave packets will influence the collective response of the system. On the other hand, a description using time independent effective potentials, which is equivalent to the case of a fixed width, is appropriate for weak coupling or for studying slow processes like the static conductivity $\sigma_\parallel(0,0)$.

In further calculations with the WPMD method we will take into account the effects of the antisymmetrization of the electrons.

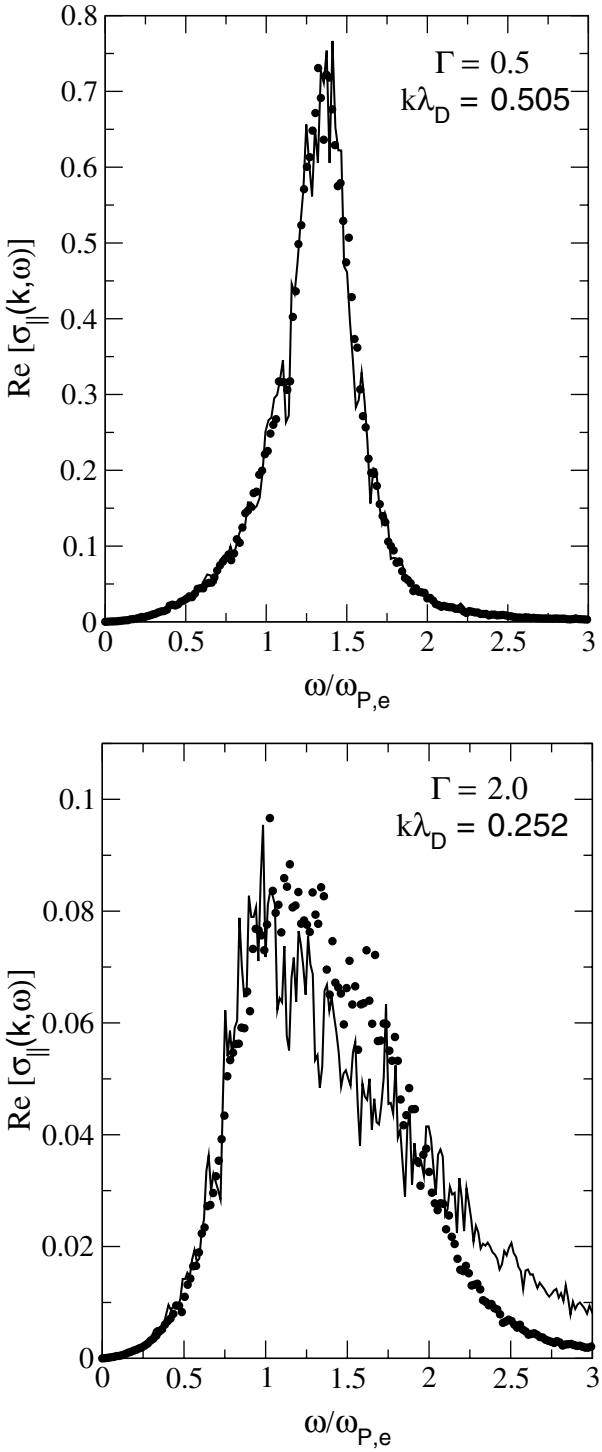


Dynamic conductivity from calculations in the WPMD method. Curve: variable width, points: fixed width.

## References

[1] M. Knaup, P.-G. Reinhard, C. Toepffer, G. Zwicknagel, J. Phys. A **36** (2003) 6165–6171

[2] E. Wigner, H. B. Huntington, J. Chem. Phys. **3** (1935) 764–770

[3] D. M. Ceperley, B. J. Alder, Phys. Rev. B **36** (1987) 2092–2106

[4] D. Saumon, G. Chabrier, H. M. Van Horn, Astrophys. J. Suppl. **99** (1995) 713–741

# Correlation Effects on Collisional Absorption in Dense Laser-Produced Plasmas

Thomas Bornath[1], Manfred Schlanges[2], Paul Hilse[2], and Dietrich Kremp[1]

[1]Universität Rostock, Fachbereich Physik, D-18051 Rostock, Germany; [2]Ernst-Moritz-Arndt-Universität Greifswald, Institut für Physik, Domstrasse 10a, D-17487 Greifswald

Starting from quantum kinetic theory, collisional absorption of laser radiation has been investigated [1, 2, 3, 4] for dense fully ionized plasmas. The balance equation for the current density, e.g., can be written in the following form [1]

$$\frac{d}{dt}\mathbf{j}_e(t) - n_e\frac{e^2}{m_e}\mathbf{E}(t) = \int \frac{\mathrm{d}^3q}{(2\pi\hbar)^3}\frac{e\mathbf{q}}{m_e}V_{ei}(q)L_{ei}^{<}(\mathbf{q};t,t), \quad (1)$$

where $i\hbar L_{ab}^{<}(t,t') = \langle\delta\rho_b(t')\delta\rho_a(t)\rangle$ is the correlation function of the density fluctuations. For the latter quantity, quantum statistical expressions were derived for plasmas in which the coupling between electrons and ions is weak due to the influence of the strong high-frequency laser field, however, the electron and the ion components may be strongly coupled within their respective subsystems [1, 5]. Consequently, the expressions for, e.g., the electrical current and the cycle-averaged energy absorption rate contain the dynamical structure factors and the dielectric function of the strongly correlated subsystems. The expressions are valid for arbitrary field strength assuming the nonrelativistic case. For high–frequency fields we get

$$\begin{aligned}\langle\mathbf{j}\cdot\mathbf{E}\rangle &= 2\int\frac{d^3q}{(2\pi\hbar)^3}V_{ei}^2(q)\,n_iS_{ii}(\mathbf{q}) \quad (2)\\ &\times\sum_{n=1}^{\infty}n\omega J_n^2\left(\frac{\mathbf{q}\cdot\mathbf{v_0}}{\hbar\omega}\right)\mathrm{Im}L_{ee}^R(\mathbf{q};-n\omega)\,.\end{aligned}$$

The ion–ion correlation is expressed by the static ion structure factor $S_{ii}$ whereas the electron–electron correlations are given by the density response function $L_{ee}^R(\mathbf{q};\omega)$ which was calculated via the local field correction function (LFC). Neglecting these two effects, we get the weak coupling results of Refs. [6, 7].

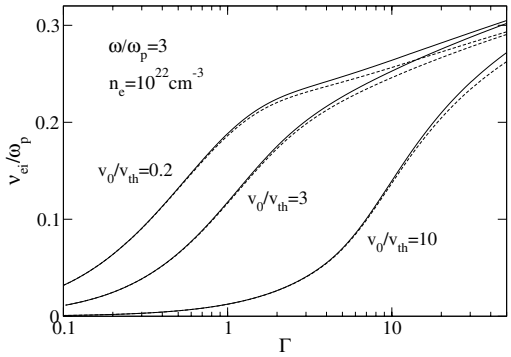


Figure 1: Electron–ion collision frequency as a function of the coupling parameter Γ for different values of the quiver velocity. LFC in accordance with Ichimaru and Utsumi (solid), without LFC (dashed).

Fig. 1 shows the influence of the LFC (the structur factor is calculated in HNC approximation) on the electron-ion collision frequency $\nu_{ei} = (\omega/\omega_\mathrm{p})^2\langle\mathbf{j}\cdot\mathbf{E}\rangle/\langle\epsilon_0E^2\rangle$. For weak and moderate electric fields, ($v_0/v_\mathrm{th} = 0.2$ and 3), there occur deviations in the region $\Gamma > 1$ which increase with increasing coupling. For rather strong fields, the LFC has no influence up to a coupling of about $\Gamma = 10$. Furthermore, one can see that for strong coupling the influence of the field strength becomes smaller.

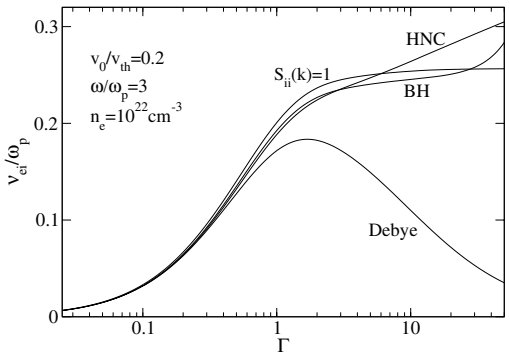


Figure 2: Electron–ion collision frequency as a function of the coupling parameter Γ. Ion structur factor in different approaches: HNC, Debye, BH (Baus–Hansen formula).

The influence of the ion–ion correlation is shown in Fig. 2. We compare different approximations for the static ion-ion structur factor $S_{ii}$ (the LFC is used in the Ichimaru approximation). Inclusion of the structur factor decreases the collision frequency for small and moderate coupling up to a value of $\Gamma \approx 5$. The Debye approximation is useful only for weak coupling. For strong coupling there is a fast increasing of the absorption. This increase is in the HNC calculation even stronger than in the semi-analytical formula of Baus and Hansen.

## References

[1] Th. Bornath, M. Schlanges, P. Hilse, and D. Kremp, J. Phys. A: Math. Gen. **36**, 5941 (2003).

[2] M. Schlanges, P. Hilse, Th. Bornath, and D. Kremp, in: Bonitz (ed.), *Progress in Nonequilibrium Green's Functions II*, World Scientific 2003, p. 50.

[3] M. Schlanges, Th. Bornath, D. Kremp, and P. Hilse, Contrib. Plasma Phys. **43**, 360 (2003).

[4] Th. Bornath, M. Schlanges, P. Hilse, and D. Kremp, in: Morawetz (ed.), *Nonequilibrium at short time scales. Formation of correlations.*, Springer 2004, p. 144–161.

[5] G. Hazak, N. Metzler, M. Klapisch, and J. Gardner Phys. Plasmas **9**, 345 (2002).

[6] Th. Bornath, M. Schlanges, P. Hilse, and D. Kremp, Phys. Rev. E **64**, 26414 (2001).

[7] H.-J. Kull and L. Plagne, Phys. Plasmas **8**, 5244 (2001).

# Thomson Scattering in Warm Dense Matter

A. Höll, R. Redmer, G. Röpke, H. Reinholz
Universität Rostock, FB Physik, 18051 Rostock

**The scattering of photons in plasmas is an important diagnostic tool. The region of warm dense matter can be probed by x-ray Thomson scattering. The scattering cross section is related to the dynamic structure factor $S(k,\omega)$. We focus on the contribution of free electrons to the dielectric function which is calculated in the Born–Mermin approximation. The inclusion of collisions modifies the dynamic structure factor significantly in the warm dense matter regime which is important for plasma diagnostics.**

Thomson scattering in plasmas has been studied for a long time [1]. Its cross section is directly related to the dynamic structure factor $S(k,\omega)$. Therefore, Thomson scattering can serve as a perfect tool to either analyze the plasma parameters, or to test the quality of the model used to determine the dynamic structure factor. Dense plasmas are opaque in the optical region so that x-rays instead of optical lasers have to be used to probe the plasma. This new technique has successfully been applied to derive plasma parameters such as density and temperature from spectrally resolved x-ray Thomson scattering experiments [2]. For this, the contributions of free, weakly bound, and tightly bound electrons to the dynamic structure factor have to be determined [1, 2, 3]. Tightly bound electrons follow the ion motion and yield elastic x-ray photon scattering. Weakly bound and free electrons give Compton-down shifted x-ray photons where, in addition, free electrons impose a distribution on the scattering signal according to the plasma temperature and density [4]. This information has to be resolved by an appropriate evaluation of the dynamic structure factor.

We focus on the contribution of free electrons which is usually treated within the random phase approximation (RPA). Strong coupling effects can be analysed within the scheme of local field corrections. Alternatively, we take into account collisions in the electron gas via a Born–Mermin approximation (BMA), i.e. calculating the dynamic collision frequency in Born approximation [5] and inserting these results into a generalized Mermin dielectric function [6]. Results for the dynamic structure factor are shown in Fig. 1 for an electron gas at a density of $10^{21}$ cm$^{-3}$ and temperatures of 0.5 eV (1), 2.0 eV (2) and 8.0 eV (3) in comparison with the RPA results. We have chosen x-ray photons of 4.13 nm wavelength and a scattering angle of 160°. Details of the theoretical approach and results for other plasma parameters will be published elsewhere [7]. Photons with several nm wavelength will be available at the free electron laser facility (VUV-FEL) at DESY Hamburg from 2005 on so that warm dense matter can be probed by x-ray Thomson scattering experiments there.

The influence of collisions is important in this strongly coupled, weakly degenerate domain. Collisions broaden the structure factor and shift the position of the peak to higher energies. For the case of lower densities $n \ll 10^{21}$ cm$^{-3}$, the RPA is applicable and collisions don't play any role. In the case of solid-density plasmas, i.e. $n \approx 10^{23}$ cm$^{-3}$, Pauli blocking prevents a major influence of collisions on the dynamic structure factor.

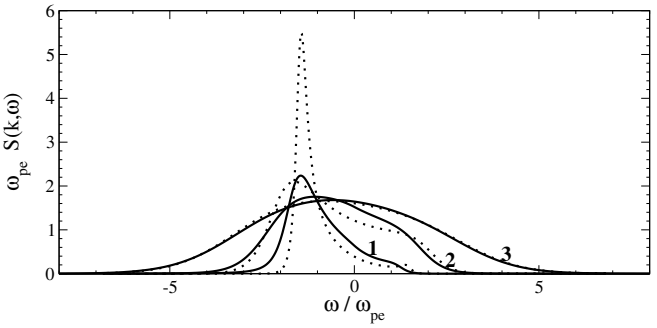


Figure 1: $S(k,\omega)$ for plasmas with a density of $10^{21}$ cm$^{-3}$ and temperatures of 0.5 eV (1), 2.0 eV (2) and 8.0 eV (3). Full lines: collisions included via the BMA; dotted lines: RPA (collisions neglected). The electron plasma frequency is $\omega_{\rm pe}^2 = n_{\rm e}e^2/(\varepsilon_0 m_{\rm e})$.

The differences between the RPA and the BMA have pronounced influence on plasma diagnostics in this regime. For instance, comparing the high-frequency wing of the dynamic structure factor with the corresponding RPA results for the lowest temperatures of 0.5 eV (1), agreement is found only if a temperature of $T_{\rm e}^{\rm RPA} = 1.0$ eV is assumed. Thus, for these plasma parameters, a temperature inferred from the RPA structure factor overestimates that given by the BMA by a factor of two.

Improved approximations for the collision frequency beyond the Born approximation are needed (i) to indicate the range where collisions are important for the determination of plasma parameters, and (ii) to improve the accuracy of thermodynamic data inferred from x-ray Thomson scattering experiments. For a complete description of Thomson scattering, the contributions of ions and bound states have to be considered as well. This is the aim of future efforts.

## References

[1] J. Chihara, J. Phys.: Condens. Matter **12**, 231 (2000).
[2] S.H. Glenzer et al., Phys. Rev. Lett. **90**, 175002 (2003); Phys. Plasmas **10**, 2433 (2003).
[3] G. Gregori et al., Phys. Rev. E **67**, 026412 (2003).
[4] O.L. Landen et al., J. Quant. Spectrosc. Radiat. Transf. **71**, 465 (2001).
[5] H. Reinholz, R. Redmer, G. Röpke, A. Wierling, Phys. Rev. E **62**, 5648 (2000).
[6] G. Röpke et al., Phys. Lett. A **260**, 365 (1999).
[7] A. Höll, R. Redmer, G. Röpke, H. Reinholz, in preparation.

# Analytical and Numerical Studies on the Non-Linear Rayleigh-Taylor Instability

R. Ramis, J. Ramirez, and J. Sanz
E. T. S. I. Aeronáuticos, Universidad Politécnica de Madrid

The Rayleigh-Taylor instability (RTI) takes place when a stratified fluid is submitted to an acceleration in the direction of the density gradient. A fully nonlinear sharp boundary model (SBM) for the development of the 2D RTI at ablation fronts has been developed [1], and it is applicable for ablation fronts with large Froude number, when cutoff of the unstable spectrum occurs for long-wavelength perturbations. We found that, besides the trivial zero amplitude solution, there is another equilibrium shape. The non-steady weakly nonlinear analysis (up to third order) gives us the following damped oscillator equation:

$$\frac{\partial^2 \xi}{dt^2} + 4\varepsilon \frac{\partial \xi}{dt} + \left( \left( \frac{k}{k_c} \right)^{\frac{n-1}{n}} - 1 \right) \xi - \frac{\xi^3 k^2}{b(n)^2} = 0, \qquad (1)$$

for the amplitude $\xi$ of the fundamental mode of a periodic perturbation with wavenumber close to the cutoff wavenumber ($k \simeq k_c$), where $\varepsilon = \sqrt{k_c V_a^2 / g}$ is a small parameter (for large Froude numbers), being $V_a$ and $g$ the ablation velocity and the acceleration, $t$ is the time scaled with $\sqrt{k_c g}$, $n$ is the heat conductivity exponent ($\vec{q} \propto -T^n \nabla T$), and $b(n)$ is a $n$ dependent constant close to unity (i.e. $b = 0.95$ for $n = 2.1$). This equation can be interpreted by the simple mechanical analogy shown in Fig. 1. Hence, for perturbations with $k > k_c$, the ablation surface can become nonlinearly unstable if the initial amplitude is outside an attraction basin. In fact, at the cutoff predicted by the linear theory, any finite perturbation is indeed unstable.

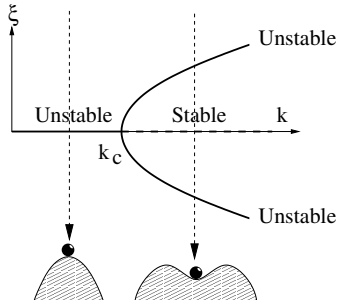


Figure 1: Mechanical analogy for Eq. 1.

We have confirmed qualitatively this phenomena by means of numerical simulations with code MULTI2D [2, 3]. We operate the code in eulerian mode, using a regular rectangular grid in a non-inertial reference frame, and with only the hydrodynamics and the heat diffusion modules active. We initialize the code with a 1D steady analytical solution [4]. Boundary conditions are also forced to follow this solution. After some time (100 time units; needed to reach a numerically stationary flow), the flow is impulsively perturbed with a zero divergence velocity field with transversal wavenumber $k$ just above the cutoff $k_c$. For small perturbations the stable solution is recovered after some time, and for large perturbations the amplitude grows unbounded (see Fig. 2). The curve separating both behaviors (dashed line) corresponds to a stationary non-trivial unstable solution. Fig. 3 shows the actual density

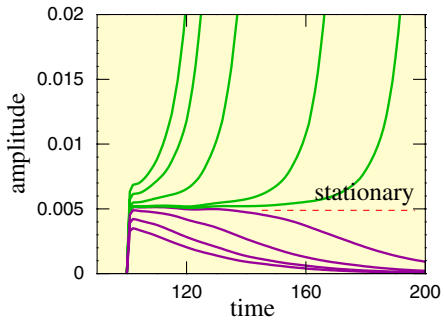


Figure 2: $\xi(t)$ for different perturbations.

plots obtained in the simulations for perturbations just below/above the threshold. This phenomena has important repercussions for inertial confinement fusion (ICF); to be damped, irregularities must have not only small enough wavelength, but also **small enough amplitude**.

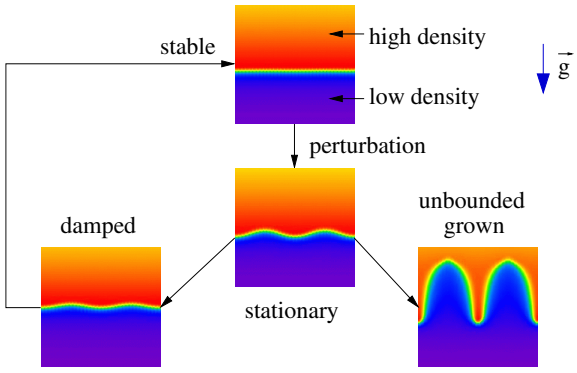


Figure 3: Nonlinearly unstable ablating surface.

## References

[1] SANZ, J., RAMIREZ, J., RAMIS, R., BETTI, R., and TOWN, R.P.J. Phys. Rev. Lett. **89** (2002) 195002.
[2] RAMIS, R., and MEYER-TER-VEHN, J., MULTI2D - A Computer Code for Two-Dimensional Radiation Hydrodynamics, Rep. MPQ174, Max-Planck-Institut für Quantenoptik, Garching, Germany (1992)
[3] http://server.faia.upm.es/multi
[4] RAMIREZ, J., RAMIS, R., and SANZ, J., to appear in Laser & Part. Beams (2004)

# Rayleigh-Taylor instability in elastoplastic solids

J. J. López Cela[1], A. R. Piriz[1], M. Temporal[1], N. A. Tahir[2] and M. C. Serna Moreno[1]

1) ETSII, Univ. Castilla-La Mancha, Spain. 2) Institut für Theoretische Physik, Univ. Frankfurt, Germany.

A typical experiment that can be carried out at the future synchrotron facility SIS100 at the Gesellschaft für Schwerionenforschung (GSI), Darmstadt, considers the implosion of a multilayer cylindrical target that contains a material sample (for instance, hydrogen) in the axial region. The target is axially irradiated from one side of the cylinder by an intense heavy ion beam with an annular focal spot. When the annular region of the absorber is heated by the ion beam, it expands thereby pushing the inner layers of the target (the pusher) and compressing the sample material in the axial region. Such a configuration is very suitable for an experiment dedicated to the study of the hydrogen metallization problem. The annular spot can be achieved with a rf-wobbler that will rotate the ion beam with a rotation frequency of the order of GHz with an acceptable symmetry level[1]. However, the stability of the pusher that drives the implosion still remains another issue of possible concern since the relatively low temperatures in the absorber region prevent the ablation of the pusher material, and consequently, there are no apparent mechanisms that could reduce the growth rate of the Rayleigh - Taylor (RT) instability seeded by the asymmetries in the pusher-absorber interface. Nevertheless, we have noticed from the numerical simulations that, for driving pressures of the order of few megabars, the pusher material remains in a solid or liquid state which may still retain some of the elastoplastic properties of the material that can provide a stabilizing mechanism that is certainly beneficial for the previously mentioned experiment.

In a recent work[2] we have performed a series of two-dimensional (2D) simulations using an explicit version of the ABAQUS finite element code in order to study the influence of the material elastoplastic behavior on the growth rate of the RT instability of accelerated planar solids. This behavior is defined by the yield stress Y and the shear modulus G of the material. Several calculations varying these two parameters have been performed by using gold slabs of a given thickness h initially perturbed with different wavelengths $\lambda$ and amplitudes $a_0$. The results are compared with those corresponding to the classical case, that is, when the slab behaves like an inviscid and incompressible fluid that represents the worst case with the fastest growth of the perturbations. We applied an external uniform pressure applied at the upper solid-vacuum surface that has a profile with a rise time of 100 ns after which the load is kept constant and equal to 40 GPa.

We have simulated several cases for a gold slab with initial perturbations of different wavelengths, $\lambda$ = h, h/2, h/4, h/8, h/12 and h/16. We have performed these calculations for different values of the yield stress Y between 2 $10^7$ Pa and $10^8$ Pa. The actual value of the yield stress for a solid under a pressure of 40 GPa is not known and therefore we have taken values below that one corresponding to the yield stress under static conditions. We have also performed a few calculations with different values of the shear modulus G for a given value of the yield stress Y and we have found that the value of G has no significant effect on the instability growth rate. Therefore, in the calculations presented below we have taken a constant value of G = 30 GPa.

We have computed the instability growth rate $\gamma$ as a function of the perturbation wavelength $\lambda$ for different values of the yield strength Y. The results are summarized in Figure 1. As we can see, for the lowest value of Y we have considered, Y = 2 $10^7$ Pa, the growth rate is very similar to the classical case corresponding to a fluid. However, for higher values of Y the growth rate is reduced and it becomes practically zero for relatively short perturbation wavelengths.

Thus, the elastoplastic properties of the material produce a stabilizing effect for all the perturbation wavelengths shorter than some cut-off value similar to the situations in which ablation is present. We see that even a relatively strong reduction of Y by a factor of 2.5 with respect to its standard solid value (Y = $10^8$ Pa) leads to a growth rate reduction of almost two orders of magnitude compared with the classical value for $\lambda < 10$ μm.

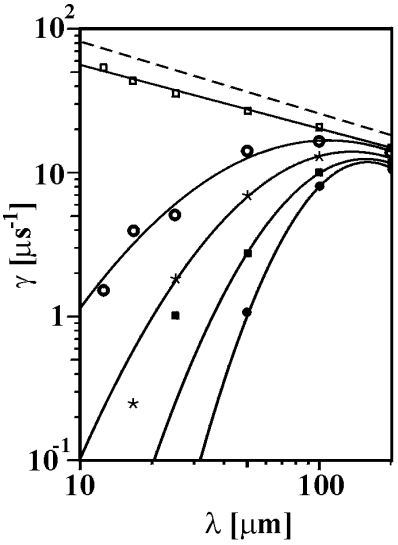


Fig. 1. Instability growth rate as a function of the wavelength. The data have been evaluated for different values of the yield stress, Y = 2 x $10^7$ Pa ( ), Y = 4 x $10^7$ Pa (0), Y = 6 x $10^7$ Pa (*), Y = 8 x $10^7$ Pa (■) and Y = $10^8$ Pa (•). The dashed line represents the classical growth rate and full lines curves fit the data.

**References**

[1] A.R. Piriz et al., *Phys.Rev.E* **67**, 017501 (2003).

[2] J.J. López Cela et al., submited to *Eur.Phys.J.*

# Bridging the Gap between Two Stream and Filamentation Instabilities

A. Bret, M.-C. Firpo and C. Deutsch

Laboratoire de Physique des Gaz et des Plasmas, Université Paris XI, Bâtiment 210, 91 405 Orsay Cedex, France

Two-stream and filamentation instabilities in beam/plasma interactions have been investigated for a long time and have their wave vectors respectively parallel and normal to the beam velocity. As far as oblique wave vectors are concerned, it has sometimes been argued that the only relevant quantity for instabilities is the wave vector projection on the beam velocity. However, even if such can be the case for slightly oblique wave vectors, this reasoning cannot stand all the way through purely normal wave vectors, since there are still some non-negligible unstable modes for such wave vectors yielding the so-called filamentation instability whose importance for the beam stability is paramount. Recent papers dealing with quark-gluon and atmospheric plasmas [1] emphasized oblique instabilities, and numerically computed growth rates show non-trivial effects in directions which are neither parallel nor normal to the velocity distribution anisotropy. Other investigation [2] paid attention to oblique vectors numerically investigating a 2D fluid model. We have analytically investigated oblique wave vectors unstable modes of a beam passing through a plasma at non relativistic velocity $\mathbf{V}_b$ with return current using a simple waterbag model for the plasma velocity distribution (thermal velocity $V_{th}$).

The dielectric tensor is derived within the linear Vlasov-Maxwell formalism. The dispersion equation must be valid for any orientations of the wave vector as well as any orientation of **k** and **E** because the same imaginary root of dispersion equation yields the longitudinal two-stream instability for **k** // $\mathbf{V}_b$ and the quasi transverse filamentation instability for **k** perp. $\mathbf{V}_b$. Any formalism embracing both modes must therefore be able to deal with any kind of waves as far as the angle (**k**, **E**) is concerned. The dispersion equation found displays two branches, one of them bridging between the two stream and filamentation instabilities. Fig. 1 displays a plot of this mode growth rate over the plan ($k_{//}$, $k_{perp}$). The two arches in the $k_{perp}$ and $k_{//}$ directions pertaining respectively to the filamentation and two-stream configuration are clearly visible, but the main feature of this plot is indeed the very important and slowly decreasing growth rate in a $\phi$ direction which is rigorously given by

$$\tan\phi=\frac{1+\alpha}{\alpha_t}, \qquad (1)$$

where $\alpha = N_b/N_p$ and $\alpha_t = V_b/V_{th}$. We proved that the asymptotic growth rate in the $\phi$ direction equals the maximum filamentation growth rate $\gamma_{perp} \approx \beta\sqrt{\alpha}$ ($\beta = V_b/c$). The maximum growth rate all over the **k** space, $\gamma_{//}$, is found along the beam and one has

$$\frac{\gamma_{perp}}{\gamma_{//}} \approx 1.45\beta\alpha^{1/6}, \qquad (2)$$

which is smaller than 1 as soon as $\alpha < 1$. Fig. 2 is a contour plot of Fig. 1 and shows the growth rate is more than 80% of its maximum value up to $Z_{perp} \approx 40$ whereas the maximum $Z_{perp}$ yielding an instability in the normal direction is only 6.

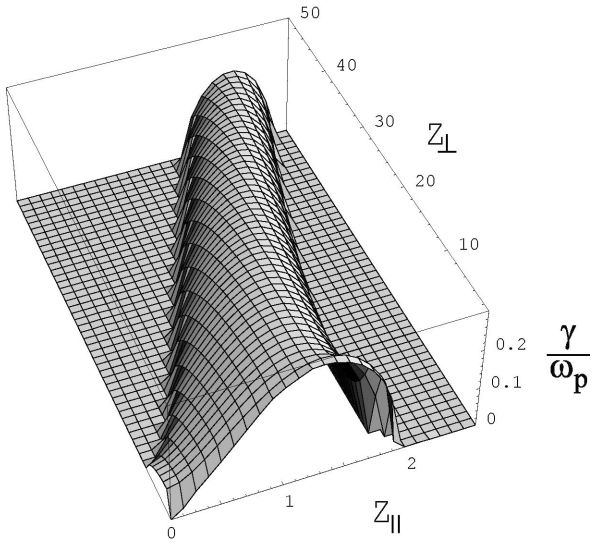


Fig. 1: Growth rate for the usual two-stream/filamentation mode in terms of the reduced wave vector $\mathbf{Z} = \mathbf{k}V_b/\omega_p$. Parameters are $V_b/c = 0.2$, $\alpha = 1/10$, $\alpha_t = 1/30$.

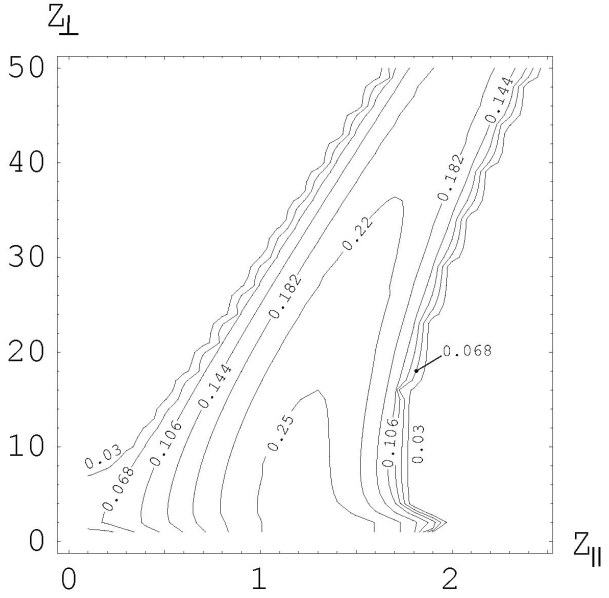


Fig. 2: Contour plot of Fig. 1. Still $\mathbf{Z} = \mathbf{k}V_b/\omega_p$.

## References

[1] J. Randrup, St. Mrowczynski, Phys. Rev. C **68**, 034909 (2003) ; O. J. G. Silveira, L. F. Ziebell, R. Gaelzer, P. H. Yoon, Phys. Rev. E **65**, 036407 (2002)

[2] F. Califano, F. Pegoraro, S. V. Bulanov, A. Mangeney, Phys. Rev. E 57, 7048-7059 (1998); F. Califano, F. Pegoraro, S. V. Bulanov, Phys. Rev. E **56**, 963–969 (1997)

# Collisional Mitigation of the Weibel instability occuring in Fast Ignition

C. Deutsch, A. Bret and M.-C. Firpo

Laboratoire de Physique des Gaz et Plasmas, Bâtiment 210, Université Paris XI, 91405 Orsay Cedex, France

Very recent experimental results seem to confirm the relativistic electron beam (REB) penetration in dense and hot plasmas with parameters compatible with those of possible outer layers surrounding a super dense DT core [see Fig. 1] [1]. Such a situation motivates our present focus on the basic mechanisms affecting REB propagation during the initial time scale ~ $\omega_p^{-1}$ ($\omega_p$, target plasma frequency) when Weibel Electromagnetic Instability (WEI) behaves mostly linear. In particular, we intend to stress the N-body features of REB stopping in those specific conditions.

Paying first attention to the WEI linear growth rate (LGR), we notice that in a standard Maxwell-Vlasov setting including REB-target collisions [2], this LGR is essentially controlled by two asymmetry parameters

$$A=1+r^2 511(1-\gamma_b^{-2})T_p^{-1},\quad B=1+511(\gamma_b-\gamma_b^{-1})T_b^{-1} \qquad (1)$$

where $r=N_b/N_p, \gamma_b=\left(1-\frac{V_b^2}{c^2}\right)^{-1/2}$, $T_b$ and $T_p$, denote respectively REB and target plasma isotropic temperature in keV.

Moreover, it is also useful to remark that the quasi-linear theory (Dupree-Weinstock [3]) based on mode-mode coupling can provide even more accurate parameters, in the form

$$A'=\frac{AT_p}{T_p+XD},\quad B'=\frac{BT_p}{T_b+XD} \qquad (2)$$

with X, positive solution of ($u = (rv_b/\gamma_b)^2$)

$$(1+r^2)X^4+\left[r^2\frac{T_p}{m}+\frac{T_b}{m\gamma}(1+r^2)\right]X^2-u\left[\frac{T_p}{m}+\frac{T_b}{m\gamma}\left(u^2-r^2\frac{T_p}{m}\right)\right]=0 \qquad (3)$$

and D = 511r (1 - $\gamma_b^{-1}$) in keV. Using respectively (A,B) and A', B') in the relevant linear dispersion relations, we obtain the WEI growth rates depicted on Figs. 2, as linear and turbulent, respectively. We then emphasize moderately hot ($T_p \leq 1$ keV) outer DT layers and 1 MeV REB with a thermal $T_b \leq 1$ keV. Maximum LGR $\delta_{max}$ occurs close to the skin depth wavelength $c/\omega_p$. $\delta_{max}$ is also shown steadily decaying with increasing $N_p$. Also, quasi-linear ("turbulent") LGR profiles stand beneath linear ones.

The main purpose now is to stress the obvious mitigating effect of the WEI through collisions in the $kc/\omega_p \geq 1$ range when typical parameters of the REB-Target plasma interaction are used for mimiking a fast ignition process.

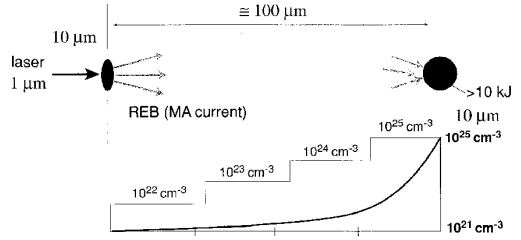


**Fig.1**: Relativistic electron beam (REB) propagation with MeV incoming energy through layers of increasing density $N_p$ in a core of precompressed DT fuel.

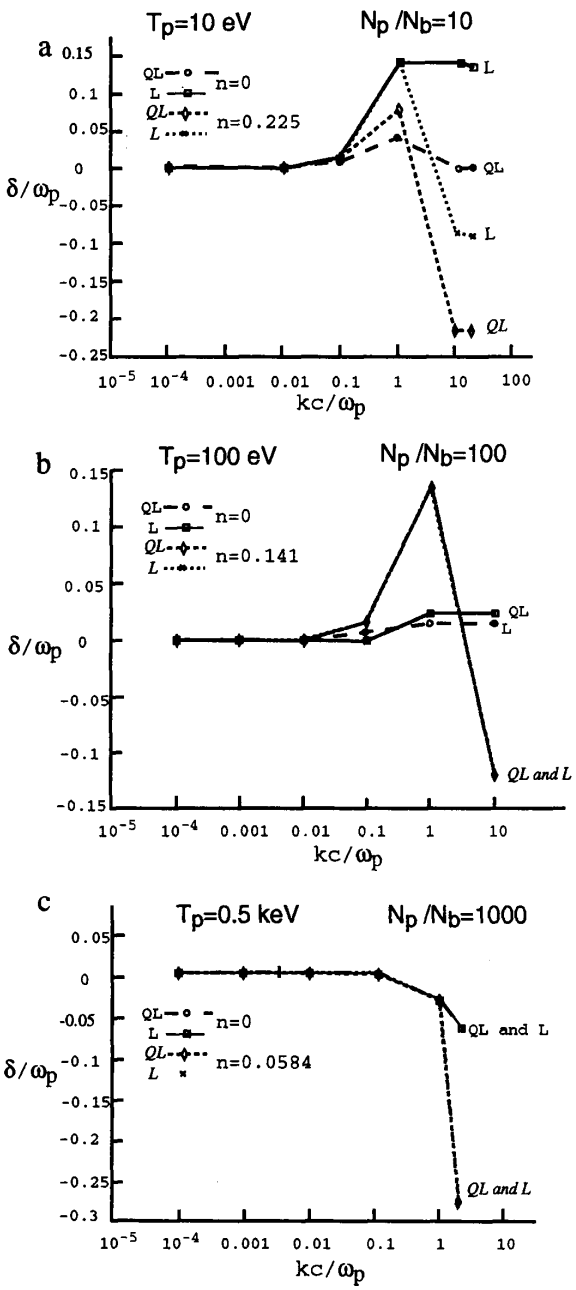


**Figs. 2 (a)-(c)** : Weibel growth rates for a REB with anisotropic temperature $T_b$ (ortho, para) = 10 keV, 10 eV, density $N_b=10^{22}$cm$^{-3}$ and energy target $E_b$=1 MeV in target electron. Plasma with **(a)** $T_p$=10 eV, $N_p/N_b$=10 ; **(b)** $T_p$=100 eV, $N_p/N_b$=100 ; **(c)** $T_p$=1 keV, $N_p/N_b$=1000 ; n=ν/$\omega_p$ qualifies a REB-target collision rate.

## References

[1] R. Kodama *et al*, Nature, **412**, 798 (2001).

[2] T. Okada and K. Niu, J. Plasma Phys., **23**, 423 (1980).

[3] M. Kono and Y. H. Ichikawa, Prog. Ther. Phys., **49**, 754 (1973).

# Integrated Simulations of Targets for Fast Ignition with Proton Beams

R. Ramis and J. Ramirez
E. T. S. I. Aeronáuticos, Universidad Politécnica de Madrid

The heavy-ion-beam (HIB) indirectly driven compression of a small amount of DT fuel, and its fast ignition by means of a beam of laser accelerated protons (PB) is considered [1]. Firstly, a representative working point

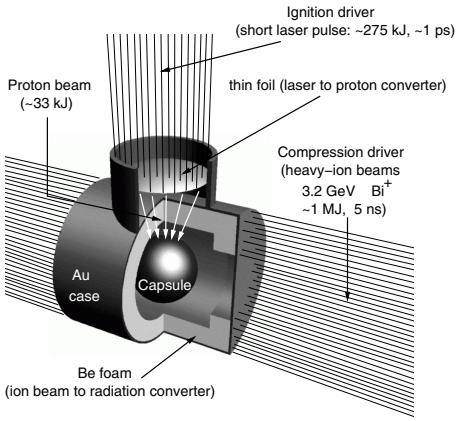


Figure 1: Target scheme for fast ignition with PB.

(0.8 mg of DT at 400 g/cm$^3$) has been derived from the energy balance of an hypothetical power plant [2]. Secondly, self-consistent 2D radiation hydrodynamic simulations with MULTI [3, 4] allows us to define and optimize a HIB-driven hohlraum target, as well as to determine the minimum PB energy ($\simeq$ 33 kJ) needed to ignite the asymmetrically compressed fuel. Thermonuclear ignition and burn is now included in the simulations; the predominant reaction $D + T \rightarrow n + \alpha$ is considered, neutrons are assumed to escape, while $\alpha$ particle energy is transported kinetically. Fig. 2 shows the ignition process; the beam (coming from above) produces a hot spot with temperature up to 20 keV and a complex hydrodynamic motion that induces a density hole ($\rho \simeq 100$ g/cm$^3$) in the compressed core. The energy yield is 83 MJ.

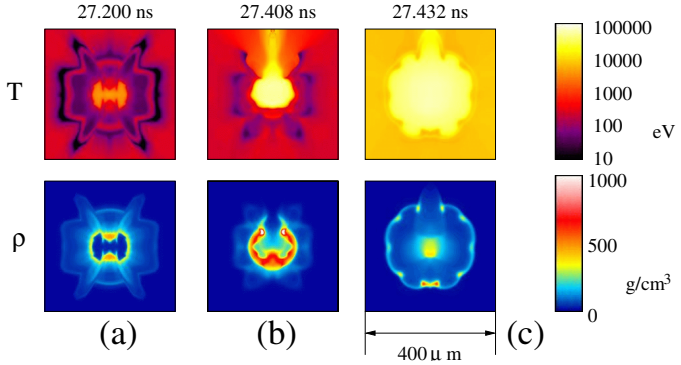


Figure 2: MULTI simulation: before ignition (a), at ignition (b), and after ignition (c)

Although HIB timing requirements are similar to the ones in a conventional (NIF like) target, the implosion is about five times less sensitive to implosion asymmetries. This fact allows us to reduce the hohlraum size, improve the driver coupling, reduce the compression energy, and have enough clearance for the installation of the PB converter foil at distances (d$\simeq$3-4 mm) appropriate for an efficient ignition. Despite the fact that the ignition process takes place inside a rather irregular fuel distribution, the scaling ($E_{ign} \propto d^{0.7}/\rho^{1.3}$) given in [6] is appropriate; PB energy clearly decreases when the average density increases or when the distance between PB converter and fuel is reduced. A target design with energies (967 kJ of 3.2 GeV Bi HIB + 275 kJ of short laser pulse), sizes (0.56 cm of length/diameter), and mass (0.8 mg of DT) a factor 1.5 to 4 smaller than in conventional targets [5] is proposed as a trade-off between two opposite HIB parameters: energy and intensity. Although this target needs less total

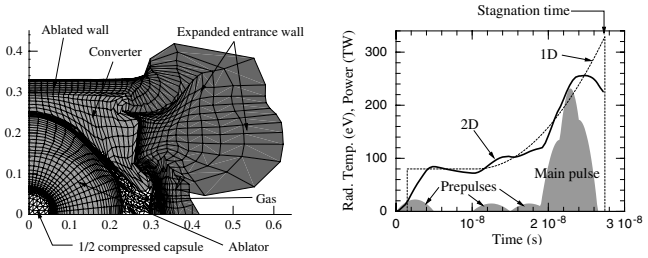


Figure 3: Nominal target after 25 ns. HIB (shadow) and radiation (lines) pulses.

driver energy than a conventional one, a very energetic laser short-pulse and the focusing of the PB into a 20 $\mu$m spot are required. A relaxation of the focusing will imply an increase of laser energy; we found that 650 kJ are needed for a 40 $\mu$m spot.

In the current 2D simulations of a complete target, we use around 4500 computational cells, 32 propagation directions for thermal radiation, and 50 heavy-ion beamlets each time step. Each simulation needs about 90 minutes (implosion) and 4 hours (ignition) on a Pentium IV at 2.66 GHz with Linux.

## References

[1] ROTH, M., et al., Phys. Rew. Lett. **86** (2001) 436
[2] RAMIS, R., and RAMIREZ, J, Working region for Fast Ignition with Proton Beams, GSI-Report, GSI-2002-7, november 2002.
[3] RAMIS, R., et al., Comp. Phys. Comm. **49** (1988) 475
[4] http://server.faia.upm.es/multi
[5] RAMIS, R., et al., Nucl. Instr. and Meth. in Phys. Res. A **464** (2001) 45
[6] ATZENI, S., TEMPORAL, M., and HONRUBIA, J.J., Nucl. Fusion **42** (2002) L1

# Laboratory Planetary Physics Using Intense Heavy Ion Beams

N. A. Tahir[1], B. Geil[2], A. Shutov[3], A. R. Piriz[4], M. Temporal[3], and D. H. H. Hoffmann[1,2]
[1]GSI Darmstadt; [2]TU-Darmstadt; [3]IPCP Chernogolovka; [4]UCLM Spain

The Giant planets in our solar system are fascinating objects and investigation of their structure is a problem of fundamental scientific interest. Using the improved set of gravitational moments provided by the Voyager, new models have been developed for the distant planets Uranus and Neptune [1]. The two planets are believed to have very similar structure. Fig.1 shows a crossectional view of Neptune based on such models and it is seen that it has an atmosphere of hydrogen and helium while its surface consists of a thick layer of ice which has a temperature of 5000 K, a pressure of 3 Mbar and a density of about 4 . g/cm$^3$

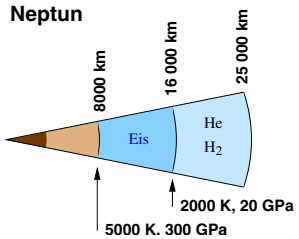


Figure 1: A Model Picture of Neptune.

Figure 2 shows a phase diagram of water under those planetary conditions which is obtained by ab initio Car-Purinello molecular dynamics simulation [2].

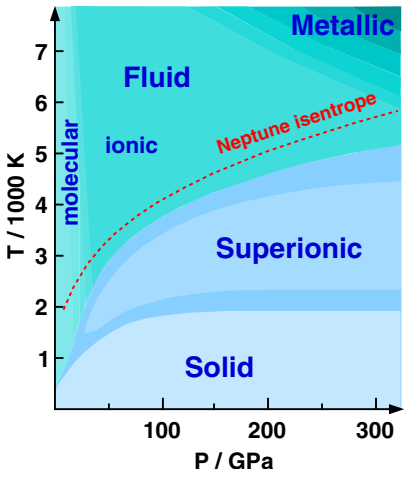


Figure 2: A Phase Diagram of Water

In a previous publication [3] we showed that one may use an intense heavy ion beam to implode a hydrogen sample that is enclosed in a multi-layered cylindrical target to extreme physical conditions that are found in the interior of Jupiter. In this contribution we have used the same target design that consists of a solid cylindrical lead shell that is filled with water. One face of the cylinder is irradiated with an intense heavy ion beam which has an annular focal spot. This avoids direct heating of the sample material by the beam. The lead material around the sample material is heated and the high pressure generated in the heated region implodes the sample material quasi-isentropically.

Using a two-dimensional hydrodynamic computer code we have carried out simulations of implosion of the above target using a high intensity uranium beam with a particle energy of 1 GeV/u and a pulse duration of 50 ns. For the beam intensity, N, we use three different values, namely, $5 \times 10^{11}$, $10^{12}$ and $2 \times 10^{12}$ respectively. These beam parameters correspond to the future SIS-100 beam. The results are plotted in Figs.3 and 4. where we plot the density and pressure at the time of maximum compression vs radius at the middle of the cylinder in the sample region (ice). It is seen that using the above beam intensity range one can achieve a density of 4 - 6.5 g/cm$^3$, a pressure of 2 - 12 Mbar while the corresponding temperature range is 2000 - 10000 K. Using the future SIS-100 beam one can therefore access the entire phase diagram of water shown in Fig.2.

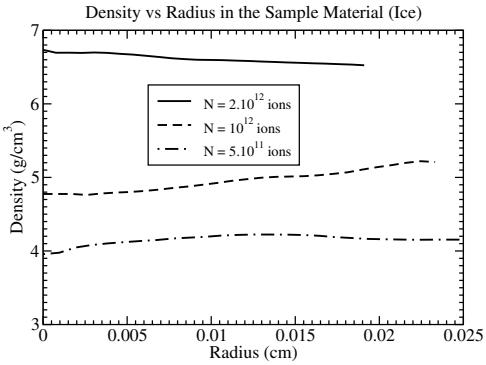


Figure 3: Density vs Cylinder Radius at the Time of Maximum Compression Using Different Beam Intensities, $\tau$=50 ns.

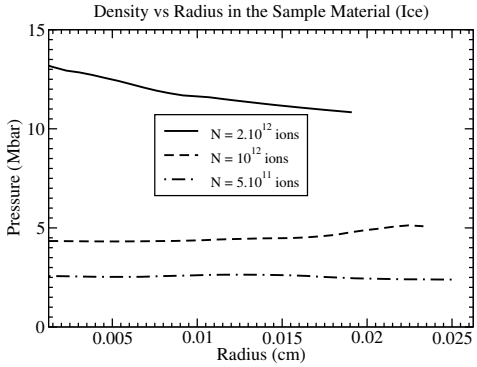


Figure 4: Pressure Profiles Corressponding to Fig.3

**References**

[1] M. Podlak et al., Planet. Space Science 43 (1995) 1517.

[2] Carlo Cavazzoni, PhD Thesis, Int. School for Adv. Studies, Rome (1998)

[3] N.A. Tahir et al., Phys. Rev. E 63 (2001) 016402.

# Simulations of Recent Heavy Ion Beam Matter Heating Experiments at GSI

N. A. Tahir[1], A. Adonin[2], C. Deutsch[3], V. E. Fortov[4], V. Gryaznov[4], D. H. H. Hoffmann[1,5], M. Kulish[4], I. V. Lomonosov[4], V. Mintsev[4], P. Ni[5], D. Nikolaev[4], A. R. Piriz[6], N. Shilkin[4], A. Shutov[4], M. Temporal[6], V. Ternovoi[4], S. Udrea[5], and D. Varentsov[5]

[1]GSI Darmstadt; [2]Univ. Frankfurt; [3]LPGP Orsay; [4]IPCP Chernogolovka; [5]TU-Darmstadt; [6]Univ. Castilla-La Mancha

In December 2003, the SIS-18 delivered a 350 MeV/u intense uranium beam and a record high intensity of more than $4 \times 10^9$ particles was achieved. The beam focal spot was elliptic while the beam power profile along the radial direction was Gaussian with a $(\mathrm{FWHM})_x = 0.85$ mm and $(\mathrm{FWHM})_y = 1.6$ mm. The experimentally measured temporal beam power profile is shown in Fig.1 which is very similar to a Gaussian with a FWHM of about 300 ns.

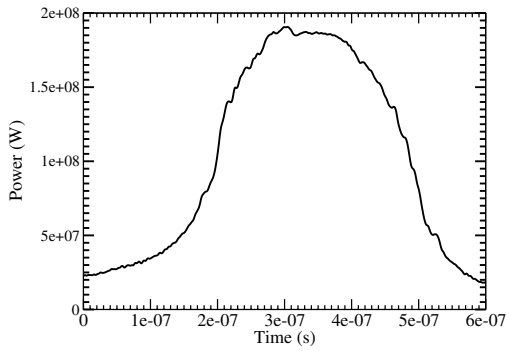


Figure 1: Experimentally measured temporal power profile of the beam.

During this beam time compound metallic targets with plane geometry were irradiated by the beam and temperature of the heated material was measured using a newly developed six channel pyrometer. Details about the experimental setup and measurements are presented in [1].

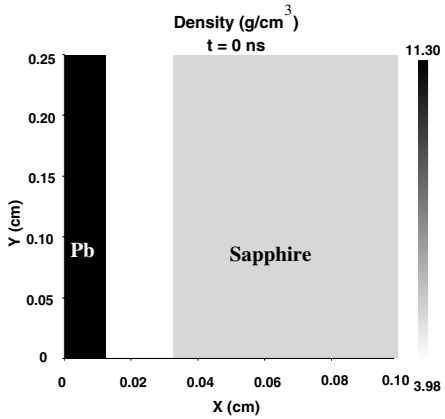


Figure 2: A vertical plane showing facial view of the target.

One of the typical target designs used in these experiments is presented in Fig.2 which shows one quarter face of the target. It consists of a thin lead foil that is 250 $\mu$m thick and has a hight of 5 mm. This is followed by a gap which is 200 $\mu$m wide and that is followed by a thick layer of sapphire which is about 1 mm thick. In some cases the gap was filled with helium gas at different pressures as helium gas is useful for diagnostic purposes. However in the present calculations we consider a vacuum in the gap.

The beam is directed perpendicular to the target face with its center coinciding with the origin. In the experiment a tungsten beam blocker was used to avoid heating of the sapphire window and to simulate this effect we cut the Gaussian distribution along the x-direction at x = 0.375 $\mu$m. In the following are presented the simulation results that have been achieved using a two-dimensional hydrodynamic code, BIG-2 [2].

In Fig.3 we plot the target temperature along x-direction at y = 0 and at different times in the lead foil. It is seen from Fig.3 that the target is uniformly heated along the x-direction to a temperature of 3700 K at t = 600 ns when the beam has just delivered its total energy. The heated material expands in the cavity until it arrives at the sapphire wall at t = 1 $\mu$s and as a result of this impact a temperature peak of about 4500 K is created at the boundary. The material is reflected at the boundary and it moves backwards. The temperature peak also starts to smooth out and spreads up to the reflection front as is seen from the profile at t = 1.5 $\mu$s.

The temperature values predicted by the simulations will be compared with the experimental measurements after the results are thoroughly analyzed.

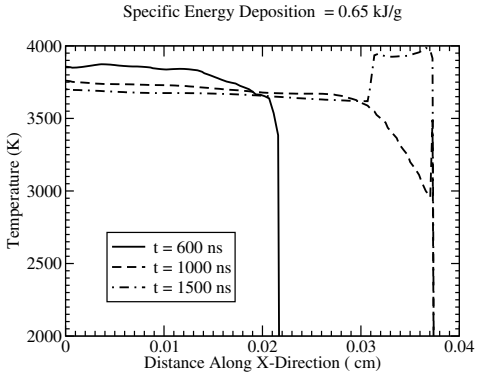


Figure 3: Target temperature along x-direction at different times

**References**

[1] D. VARENTSOV et al., this report.

[2] V.E. FORTOV et al., Nucl. Sci. Eng. 123 (1996) 169.

# Interaction of the CERN Large Hadron Collider (LHC) Beam with Solid Targets

N. A. Tahir[1], V. Kain[2], R. Schmidt[2], A. Shutov[3], I. V. Lomonosov[3], V. E. Fortov[3], A. R. Piriz[4], M. Temporal[4], and D. H. H. Hoffmann[1,5]

[1]GSI Darmstadt; [2]CERN Switzerland; [3]IPCP Chernogolovka; [4]Univ. Castilla-La Mancha; [5]TU-Darmstadt

The large hadron collider (LHC) will operate at an energy of 7 TeV with a luminosity of $10^{34}$ cm$^{-2}$s$^{-1}$. This requires two beams, each with 2808 bunches. The nominal intensity per bunch is considered to be $1.1 \times 10^{11}$ while each bunch has a duration of 0.5 ns. Two neighboring bunches are separated by 25 ns so that the total length of the LHC beam will be 75 $\mu$s. The power profile along the radial direction is a Gaussian with a standard deviation, $\sigma = 0.2$ mm. The deflection of these protons in a circular path with a circumference of 27 km is caused by superconducting magnets. In the event of quenching of a magnet, or after accelerator equipment failures, the beam will not follow its allocated path. Sophisticated diagnostics will detect such failures and trigger an extraction kicker that safely deflects the beam into a target. However, in case of failure of the machine protection systems, the beams may cause considerable damage to machine equipment. It is therefore necessary to evaluate the possible equipment damage caused by the beam in the event of a functional failure.

Using a two-dimensional computer code BIG-2[1], we have studied the hydrodynamic and thermodynamic response of a solid copper target in plane geometry that is irradiated with the LHC beam perpendicular to one of its faces. The face area of the target is 4 cm$^2$ (2 cm x 2 cm) and the specific energy deposited by the hadronic shower is calculated using the FLUKA code.

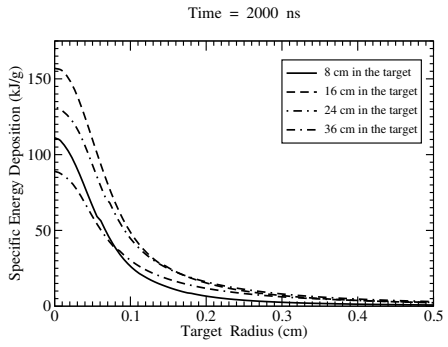


Figure 1: Specific energy deposition vs transverse target dimension at t = 2 $\mu$s and at different lengths, L into the target.

In Fig.1 we plot the specific energy deposition vs transverse target dimension at t = 2 $\mu$s and at four different values of L, namely, 8, 16, 24 and 36 cm respectively. It is seen that corresponding to an L = 16 cm the specific energy deposition is the highest and is about 160 kJ/g which results from the impact of 80 out of the total of 2808 bunches.

The high specific energy deposition leads to a high target temperature as shown in Fig.2 where we plot the temperature vs transverse target dimension at L = 16 cm and at different values of time. It is seen that the target temperature increases with time that leads to a corresponding increase in pressure. The high pressure launches a shock wave outwards that moves the material away from the beam heated region as seen in Fig.3 where we plot the corresponding density profiles. It is seen that the density in the beam heated region decreases steadily with time and at t = 2.5 $\mu$s the density at the target center has become less than 1 g/cm$^3$ which is very low compared to the initial solid copper density of 8.93 g/cm$^3$. As a result the particles that will follow will will tunnel further and further into the target. This effect has already been observed in simulations of heavy ion beam heated targets [2]. It is therefore important to take this effect into account while designing the machine protection systems for the LHC. In addition, the study of the physics of high energy density matter with the LHC might be of considerable interest because of the high specific energy deposition of the intense 7 TeV proton beams.

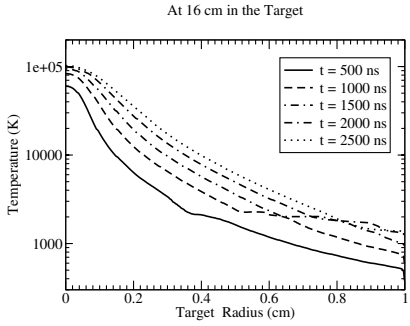


Figure 2: Temperature vs transverse target dimension at different times at L = 16 cm.

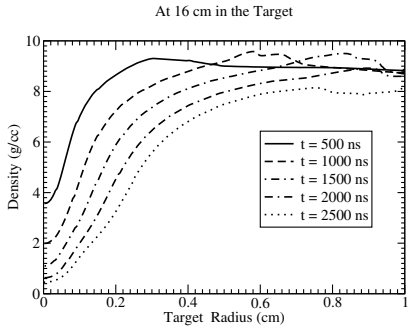


Figure 3: Density profiles corresponding to Fig.2

**References**

[1] V.E. FORTOV et al., Nucl. Sci. Eng. 123 (1996) 169.

[2] N.A. TAHIR et al., Phys. Rev. E 63 (2001) 036407.

# Recent Progress in High-Power Production Target Design Studies for the Super-FRS for a Fast Extraction Scheme

N. A. Tahir[1], H.Geissel[1], B. Kindler[1], B.Lommel[1], G.Münzenberg[1], K.Sümmerer[1], A. Shutov[2], H.Weick[1] and M.Winkler[1]

[1]GSI Darmstadt, [2]ICPR Chernogolovka

Very intense heavy ion beams of different species including Ar, Xe and U will be available at the GSI Darmstadt when the new synchrotron facility, SIS100/200 will become operational. It is expected that in a fast extraction mode, a total number of $10^{12}$ ions will be delivered in a single bunch that will have a duration, $\tau = 50$ ns. One of the important experiments that will be carried out using these intense beams are the fragment separator experiments (Super-FRS). Unlike the plasma physics experiments, in the Super-FRS experiments one is interested to use the same target over an extended period of time which requires that the target is not destroyed by the beam. However with the beam intensities that will be available at the SIS100/200 this may not be the case. Calculations have shown [1,2] that the specific energy deposition in the target could be large enough to heat the target material to temperatures far above the melting or sublimation temperature of the target material. Another very important physical parameter is the target pressure induced by beam heating. If the pressure becomes higher than a critical value, the material would break even if the temperature is below the melting or the sublimation point. For carbon one finds in the literature that this value of critical pressure is 0.1 GPa.

The target temperature is determined by the specific power, $P_s$, deposited by the beam in the target material and is given by

$$P_s = \frac{E_s}{\tau} \tag{1}$$

where $\tau$ is the pulse duration and $E_s$ is the specific energy deposition given by

$$E_s = \frac{\frac{1}{\rho}\frac{dE}{dx}N}{\pi r_b^2} \tag{2}$$

In the above equation, $\frac{1}{\rho}\frac{dE}{dx}$ is the specific energy loss due to a single ion, N is the total number of particles in the bunch and $r_b$ is the beam radius. The target temperature is determined by $P_s$ and in order to keep the temperature low one needs to reduce $P_s$ accordingly. From Eqs. (1) and (2) it is obvious that the only parameter one can vary is the beam spot area, $\pi r_b^2$. However one needs the smallest possible radius of the beam spot in order to have good resolution of the fragment separator.

It is however to be noted that in first-order optics the resolution of the separator depends only on the size of the beam spot in x-direction (the dispersive plane of the separator) while the size of the beam spot in y-direction influences mainly the transmission through the separator. Calculations have shown [2] that increasing $\sigma_y$ from 1 mm to 12 mm results in a transmission loss of 25 %, which is tolerable. A suitable value for $\sigma_x$ has been found to be 1 mm. It is therefore advantageous to use a beam with an elliptic focal spot that has a small x-dimension and a much larger y-dimension so that the beam spot area becomes large enough to keep $E_s$ below the critical level.

In a previous contribution [3] we reported calculations that showed that if one uses up to $10^{12}$ Ar ions, the target will survive for a beam spot with a $\sigma_x = 1$ mm and a $\sigma_y = 6$ mm. For Xe ions, on the other hand, if one uses a beam intensity of $10^{12}$ ions, the target will not survive even if one uses a $\sigma_y = 12$ mm. One must keep the beam intensity to a lower value of $10^{11}$. For a uranium beam the situation is much more difficult as in this case the target will only survive for a much lower intensity of $10^{10}$ particles in the bunch and with a $\sigma_y = 6$ mm. One would therefore need to develop a new target design for the higher uranium intensities, for example, a liquid metal jet target.

It is also important to note that the target has to be irradiated by the beam repeatedly over an extended period of time with a frequency of 1 Hz. If the same spot of the target is irradiated all the time, the accumulative energy will finally drive the temperature and hence the pressure to above the critical value and the target may finally be destroyed after it is irradiated a number times. In order to overcome this problem we have designed a hollow cylindrical shaped target made of solid carbon. A crossectional view (one face of the cylinder) of the target is shown in Fig.1.

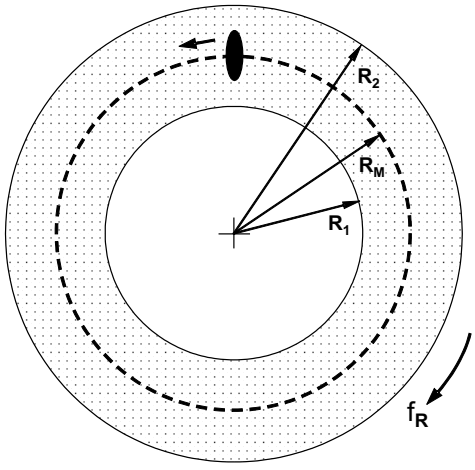


$$R_M = \frac{R_1 + R_2}{2}$$

Figure 1: Target design for the Super-FRS fast extraction scheme, $R_1 = 10$ cm, $R_2 = 15$ cm.

It is seen that the inner radius of the target, $R_{in} = 10$ cm and the outer radius, $R_{out} = 15$ cm. The beam is vertically

directed on the face of the cylinder and the center of the focal spot lies at R = 12.5 cm. The beam therefore hits the middle of the annulus. The cylinder is rotated at a low frequency so that next time (after every 1 s) the target is irradiated at a different location. The heated spot will cool due to thermal conduction by the time the target completes one rotation and that spot is irradiated again by the beam. This will help to keep the temperature and the pressure under control.

In the work reported in this contribution, we have considered a uranium beam with an intensity of $10^{10}$ ions having a particle energy of 1 GeV/u, while for the beam focal spot size we assume that $\sigma_x$ = 1 mm and $\sigma_y$ = 6 mm. Using a two-dimensional computer code, BIG-2 [4], we have studied the beam-target heating.

We assume that the cylinder is rotated around its axis at a rotation frequency of 1.04 Hz while the repetition rate of the beam is 1 Hz. The target surface therefore is irradiated 25 times at different locations in one revolution. Beam with the above parameters leads to a specific energy deposition of 0.074 kJ/g that produces a maximum temperature of 356 K which in turn induces a pressure of 0.04 GPa. In Fig.2 we present the temperature distribution in the target after 25 s. It is seen that the beam has irradiated the target at 25 different locations and the target has completed one rotation. The maximum temperature is 356 K at the location that has been irradiated at t = 25 s while the temperature at the location that has been irradiated first (at t = 0 s) has been reduced to 332 K.

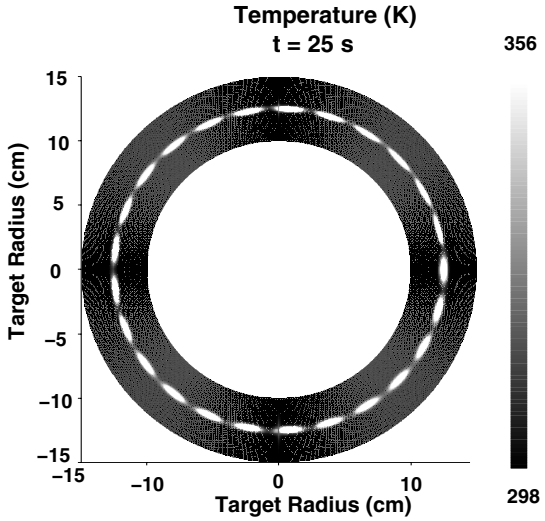


Figure 2: Temperature distribution in the target after 25 s.

In Fig.3 we plot the temperature profile along the beam radius at the location of first irradiation at different times. It is seen that due to thermal conduction the temperature decreases significantly after 25 s and heat spreads out of the beam heated region. After completion of one rotation of the target (at t = 25 s), the beam irradiates the same location that was irradiated initially. In this study we have considered that the target is irradiated 100 times. Therefore each of the 25 locations on the target surface will be irradiated 4 times with a separation of 25 s between two successive irradiations. In Table 1 we present specific energy deposition, temperature and pressure in a given location after every 25 s. It is seen that the target will survive even after it is irradiated 100 times.

One can therefore use this scheme for an Ar beam with the maximum expected intensity of $10^{12}$, a Xe beam with an intensity of $10^{11}$ and a U beam with an intensity of $10^10$. For higher intensities of Xe and U beams one must develop an alternate target concept. One such concept is to use a liquid metal jet target and work is in progress to study the feasibility of such a target design for the Super-FRS.

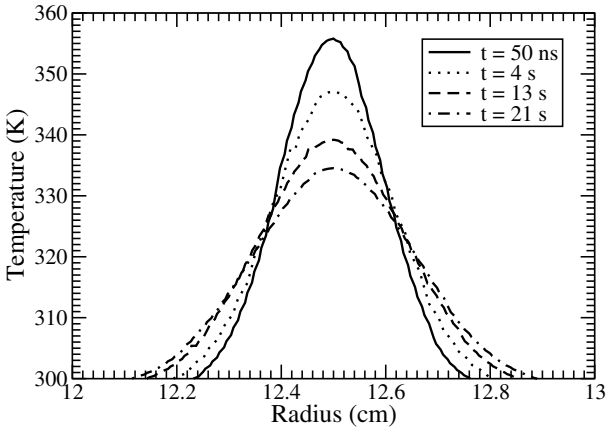


Figure 3: Temperature evolution at the place where first irradiation has taken place.

Table 1: U ions, N = $10^{10}$, $\sigma_x$ = 1.0 mm,$\sigma_y$ = 6 mm

| Time (s) | E(kJ/g) | T (K) | P (GPa) |
|---|---|---|---|
| 5.0x$10^{-8}$ | 0.074 | 356 | 0.040 |
| 25 | 0.120 | 387 | 0.060 |
| 50 | 0.150 | 413 | 0.080 |
| 75 | 0.180 | 434 | 0.096 |

## References

[1] N.A.Tahir et al., Phys. Rev. E 63 (2001) 036407.

[2] N.A.Tahir et al., Phys. Nucl. Inst. Meth. B 204 (2003) 282.

[3] N.A.Tahir et al., GSI Plasma Physics Annual Rep., GSI-2003-2, September 2003, p.33.

[4] V.E.Fortov et al., Nucl. Sci. Eng. 123 (1996) 169.

# Optimization of Focal Spot Size and Pulse Length for Heavy Ion Beam Heating of Targets at the SIS-100

N. A. Tahir[1], C. Deutsch[2], V. E. Fortov[3], V. Gryaznov[3], D. H. H. Hoffmann[1,5], I. V. Lomonosov[3], A. R. Piriz[4], A. Shutov[3], P. Spiller[1], M. Temporal[4], S. Udrea[5], and D. Varentsov[5]

[1]GSI Darmstadt; [2]LPGP Orsay; [3]IPCP Chernogolovka; [4]Univ. Castilla-La Mancha; [5]TU-Darmstadt

To maximize heating of matter by an ion beam, one should optimize the specific power deposition, $P_s$ which is given by

$$P_s = \frac{E_s}{\tau} \tag{1}$$

where $\tau$ is the pulse duration and $E_s$ is the specific energy deposition given by

$$E_s = \frac{\frac{1}{\rho}\frac{dE}{dx}N}{\pi r_b^2} \tag{2}$$

In the above equation, $\frac{1}{\rho}\frac{dE}{dx}$ is the specific energy loss due to a single ion, $\rho$ is the target material density, x is the coordinate along the particle trajectory, N is the total number of particles in the beam and $r_b$ is the beam radius that is the full width at half maximum (FWHM) of the Gaussian distribution.

When the future SIS-100 will work at its full capacity, it will deliver a uranium beam with an $N = 2 \times 10^{12}$ and a wide range of particle energy, 400 MeV/u - 2.7 GeV/u will be available. The bunch length corresponding to this energy range will be 90 - 25 ns. It is seen from Eq.(2) that $E_s$ varies as inverse square of $r_b$ and in principle one should be able to substantially increase $E_s$ by improving the beam focusibility. However one should also adjust the bunch length according to the change in the focal spot radius, otherwise the hydrodynamic transit time will not match the pulse duration and significant hydrodynamic expansion of the target will occur during the irradiation. This will lead to a significant reduction in the deposited energy.

In this contribution we report results from two-dimensional hydrodynamic simulations of heating of solid lead cylindrical targets using the SIS-100 beam assuming a particle energy of 1 GeV/u and a pulse duration of 50 ns. The beam target geometry is shown in Fig.1.

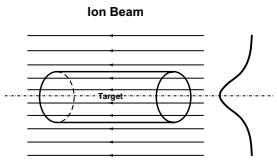


Figure 1: Beam-target geometry.

The target is assumed to have a length, L = 2 mm and three different values for the beam radius (FWHM), namely, 0.5 mm, 1.0 mm and 1.5 mm have been used. Corresponding to these values of FWHM we considered the target radii to be 0.2 mm, 0.4 mm and 0.6 mm respectively. This implies that the target will be uniformly heated along the length as well as along the radial direction.

In Fig.2 we plot density vs radius at L = 1 mm at different times during the irradiation for the case with a FWHM = 0.5 mm. It is seen that the density decreases significantly at t = 20 ns and the target radius becomes 0.4 mm due the hydrodynamic expansion. This leads to a lower energy deposition by the bulk of the ions that come in the later part of the pulse.

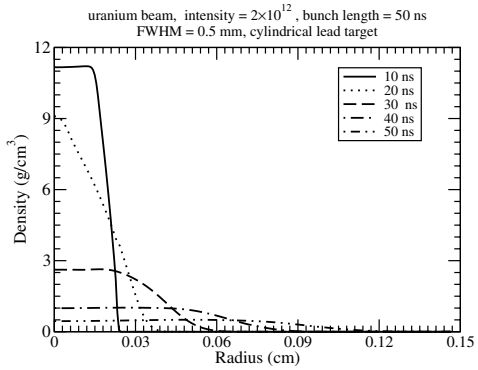


Figure 2: Density vs radius at the cylinder center, $N=2 \times 10^{12}$, FWHM=0.5 mm, $\tau$=50 ns .

In Fig.3 we plot the corresponding temperature profiles. It is seen that a maximum of 23 eV temperature is achieved at t = 20 ns but by the time the pulse delivers its total energy the temperature has been reduced to about 15 eV due to expansion of the material. For such a small focal spot radius it is necessary to have a bunch length of 5 ns that will lead to a high specific energy deposition of 1023 kJ/g which will produce a temperature of the order of 46 eV. However this bunch length will not be achievable at the SIS-100 and therefore this beam spot radius is not suitable.

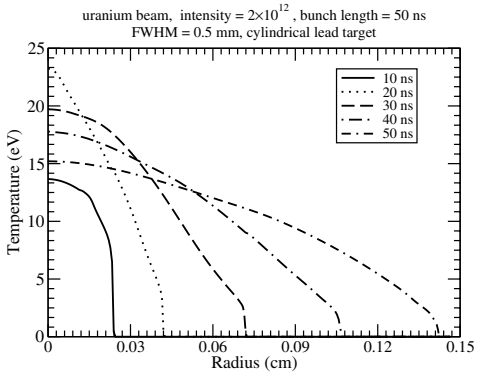


Figure 3: Temperature profiles corresponding to Fig.2

Our calculations show that for a pulse length of 50 ns an $r_b$ of 1 mm and for a pulse length of 100 ns an $r_b$ of 1.5 mm are suitable.

# Design of Future Equation-of-State Experiments at the Upgraded SIS-18 Facility

N. A. Tahir[1], A. Adonin[2], C. Deutsch[3], V. E. Fortov[4], V. Gryaznov[4], D. H. H. Hoffmann[1,5], M. Kulish[4], I. V. Lomonosov[4], V. Mintsev[4], P. Ni[5], D. Nikolaev[4], A. R. Piriz[6], N. Shilkin[4], A. Shutov[4], M. Temporal[6], V. Ternovoi[4], S. Udrea[5], and D. Varentsov[5]

[1]GSI Darmstadt; [2]Univ. Frankfurt; [3]LPGP Orsay; [4]IPCP Chernogolovka; [5]TU-Darmstadt; [6]Univ. Castilla-La Mancha

During the last beam time in December 2003, a record high intensity of $4 \times 10^9$ particles in a bunched uranium beam has been achieved. It is expected that in the near future the beam intensity will increase to about $10^{10}$ uranium particles that will enable us to carry out equation-of-state (EOS) studies in regimes that previously have not been accessed, in particular the critical point region. A detailed theoretical study of the different regions of the phase diagram that can be accessed using semi-isochoric heating and subsequent isentropic expansion of the heated material (HI-HEX) using an intense heavy ion beam has been reported in [1]. In this contribution we present a novel target design that is based on the ideas developed in [1] and that may be used to carry out these future EOS experiments. The target initial conditions are shown in Fig.1. The target consists of a wire of a test material whose properties are to be studied that is surrounded by a cylindrical shell of a transparent material like LiF, Sapphire or quartz. In this scheme we can study the physical properties of metals as well as non metals. One important non metallic material is uranium dioxide whose properties are of considerable importance to the safety of nuclear reactors. The two sides of the target are closed using two thin foils of a strong material like tungsten.

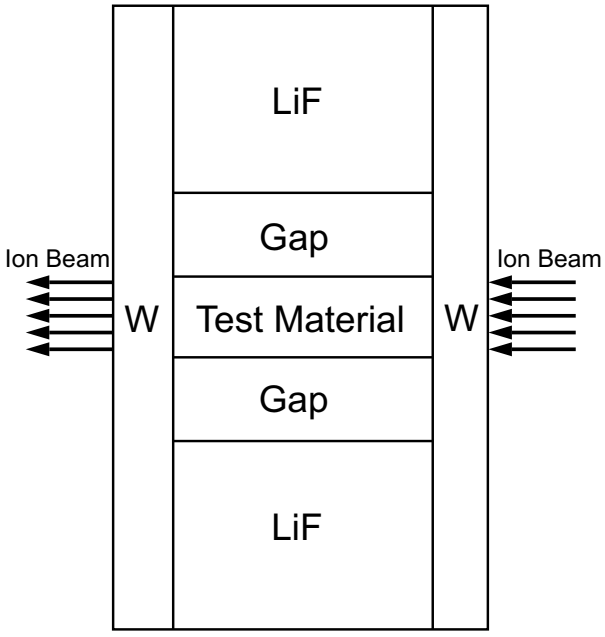


Figure 1: Target initial conditions

The length of the test material is so adjusted that the ions deposit a fraction of their energy in the wire and emerge from the opposite face of the target with a reduced energy. Since the Bragg peak does not lie inside the target, the energy deposition will be fairly uniform along the particle trajectory. In order to ensure a uniform energy deposition along the target radius we assume that the radius of the wire is much smaller than the beam radius (full width at half maximum of the Gaussian distribution). The heated wire expands mostly along the radius. The expansion along the axial direction is partly inhibited by the heavy walls of W to reduce the influence of fringe effects. It is expected that the expanding material will be reflected by the outer wall and after a few reflections between the axis and the wall, uniform physical conditions will be achieved in the test material. By choosing the size of the gap one can control the expansion and hence the final volume of the heated wire.

The diagnostic techniques that will be used to measure the physical parameters of the test material during the experiment are conceptually shown in Fig.2. The target density will be measured using x-ray backlighting. One of the proposed x-ray source is the PHELIX laser. The target temperature will be measured using pyrometric techniques and the pressure delivered onto the LiF wall will be measured using laser interferometry including VISAR. A set of the measured volume, temperature and pressure will determine the EOS of the material completely. Moreover, in heavy ion experiments the deposited energy could be estimated with a reasonable precision.

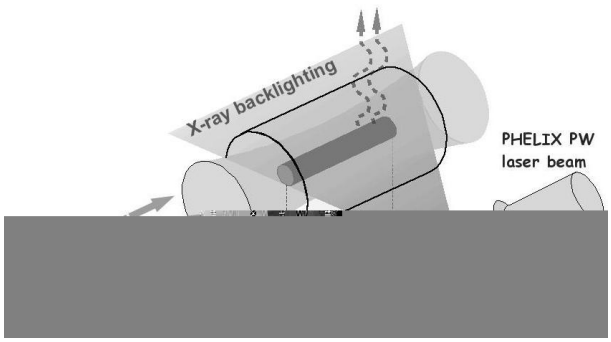


Figure 2: Layout of diagnostics

In this study the beam consists of 500 MeV/u uranium ions with an intensity of $N = 10^{10}$ particles that are delivered in a single bunch with a duration, $\tau = 300$ ns. The beam deposition profile along the radial direction is assumed to be a Gaussian with a FWHM = 1.0 mm which for calculation purposes we define as the effective beam radius. The beam power profile in time is assumed to be parabolic.

For the test material we consider four different metals,

| | Range (mm) |
|---|---|
| lead | 5.93 |
| gold | 3.42 |
| zinc | 7.07 |
| copper | 5.71 |

Table 1: Range of 500 MeV/u uranium ions in different materials

| | T(K) | P(kbar) | $\rho$(g/cm$^3$) |
|---|---|---|---|
| Lead | 5500 | 2.30 | 3.10 |
| Gold | 8500 | 6.14 | 6.10 |
| Zinc | 3080 | 3.30 | 2.40 |
| Copper | 7800 | 9.00 | 2.28 |

Table 2: Estimated critical point parameters for different metals

namely, lead, gold, copper and zinc. The range of the 500 MeV/u uranium ions in these materials is given in Table 1. These ranges have been calculated using the SRIM code [2]. In order to allow for quasi-uniform deposition along the target length, in case of Pb, Zn and Cu we consider the length of the target = 2 - 3 mm while for Au we assume a 1 mm long wire. The radius of the wire is assumed to be 300 $\mu$m which is much smaller than the FWHM of the Gaussian and therefore the energy deposition along the radial direction is almost uniform. The thickness of the two end foils of W is considered to be 50 $\mu$m each. The inner radius of the LiF shell is varied between 0.7 mm and 1.0 mm while the outer radius is assumed to be 3.5 mm.

In the following we present numerical simulation results using the beam and target parameters specified above considering lead as the test material. The radius of the lead wire is 300 $\mu$m and the radius of the inner wall of LiF is 900 $\mu$m. These simulations have been carried out employing a two-dimensional hydrodynamic computer code BIG-2 [3].

Our simulations show that at the end of the pulse at 300 ns the beam deposits a specific energy of the order of 1.7 kJ/g that leads to a temperature of about 9500 K, a pressure of the order of 20 kbar and the density has been reduced to about 4.5 g/cm$^3$.

If Fig.3 we plot the target density at t = 450 ns on a length−radius plane. It is seen that the average material density in this region is 2.8 g/cm$^3$, the average pressure is 4 kbar and the temperature is 7000 K. The estimated critical point values for these parameters for lead are 3.1 g/cm$^3$, 2.3 kbar and 5500 K respectively. One can therefor achieve the critical point region for lead in these experiments that will allow to check the theoretically calculated values for the respective parameters.

The estimated critical point parameters for some metals are listed in Table 2. Our simulations show that with these beam parameters one will be able to access the critical point region for all these metals. An experimental study of this region will be a very valuable contribution to the field of EOS of high-energy-density matter.

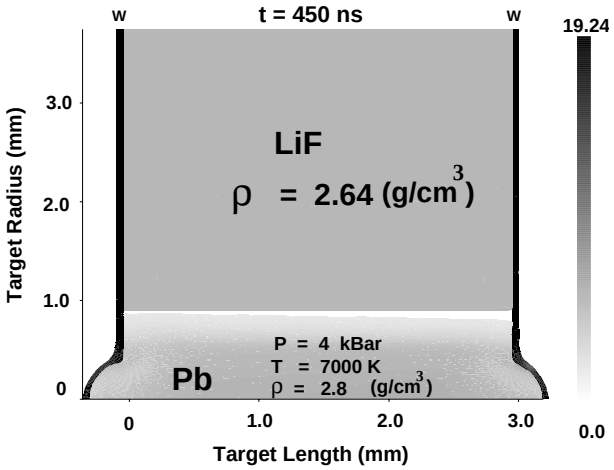


Figure 3: Target density on a length-radius plane at t = 450 ns, ions travel from right to left

**References**

[1] D.H.H. HOFFMANN et al., Phys. Plasmas 9 (2002) 3651.

[2] J.F. ZIEGLER et al., "The Stopping and Ranges of Ions in Solids" (Pergamon Press, New York, 1996).

[3] V.E. FORTOV et al., Nucl. Sci. Eng. 123 (1996) 169.

# Numerical Evaluation of the Influence of Non-Stationary and Heterogeneity of the Rotated Ion Beam on the Irradiated Cylindrical Target Compression Parameters

G.V.Dolgoleva and V.F.Ermolovich
RFNC-VNIIEF Sarov, Russia

Cylindrical target using for physical research (EOS, neutron radiation and metallic hydrogen production) under irradiation with high-energy ion beams seems natural and depends on the irradiation conditions. Higher compression ratios in targets can be achieved, if the target cores remain cold, i.e. if they are not exposed to ion beams. One of the methods used to provide such conditions is to rotate an ion beam with speed *w* around the target axis (Fig.1) [1,2] The principal requirement of achieving high compression ratios is to provide homogeneous irradiation that is assumed to be resultant from ion beam rotation at high speeds. The efforts described consist in evaluation (in1D approximation) of the requirements imposed on temporal and spatial characteristics of the ion beam rotated around the cylindrical target axis to gain high compression ratios.

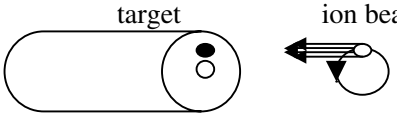


**Figure 1:** Diagram of a target irradiation with a rotating ion beam

The problem setting was as follows: a target was irradiated with an ion beam of 1 mm in diameter with the beam center being displaced for a length of 2.6mm relative to the target center. The beam moved around the target axis with period of revolution $t_w$. The energy density was homogeneously distributed over the beam area providing the energy contribution of about 100kJ/g to Au (that corresponds to the future characteristics of SIS (GSI) and TWAC (ITEF) facilities).

The following two types of the ion beam energy rate dependences on time were under consideration: time-constant and parabolic. The ion beam duration was $t_i$=100ns. The period of revolution of the ion beam, $t_w$ varied from 0.1 to 50 ns. The target poles' dynamics difference value [3] obtained during 1D comparative computations with respect to the ion beam's rating data (the "unlimited" speed of rotation, the spherical form of an ion beam with homogeneous distribution of energy) was used as a parameter allowing the influence of 2D geometry to be evaluated.

Fig.2 shows the curves of the radial compression decrease versus the period of revolution of the ion beam, $t_w/ t_i$ for the parabolic and time-constant energy rates of the ion beam (Cr(tw=0) ≅15).

The results show that for $0.1 < t_w/ t_i < 0.3$ there is a significantly lower influence of the two-dimensional nature of heating on the radial compression for the parabolic time-dependence of the ion beam energy rate than for the time-constant dependence. If $tw/ t_i < 0.1$ or $0.3 < t_w/ t_i$ , the effect of the ion beam rate time-dependence on the radial compression is less noticeable.

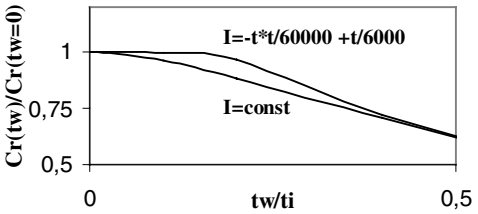


**Figure 2:** The radial compression decrease versus the ion beam's period of revolution

It was examined how the elliptic form of the ion beam with homogeneous energy distribution and the cylindrical beam with heterogeneous energy distribution over the spot area influenced the compression ratio (figs.3, 4).

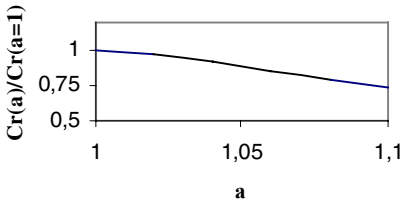


**Figure 3:** The radial compression decrease versus the ion beam form ($ar_0$ is an ellipse semi-axis)

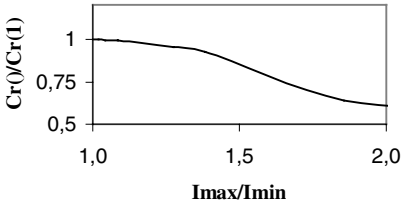


**Figure 4:** The dependence of the radial compression decrease on heterogeneity of energy distribution over the ion beam

Analysis of the numerical results obtained allows us to conclude that spatial parameters of the ion beam significantly influence the homogeneity of the cylindrical shell convergence and that knowledge of the beam form and the energy distribution over the spot area is required to carry out experiments.

## References

[1] B. Yu. Sharkov et al., Nucl. Instr. Meth. A. 464, 1 (2001).

[2] A.R.Piris, N.A.Tahir, D.H.H.Hoffman, M.Temporal Phys.Rev E 67,017501 (2003)

[3] Yu.S.Vakhrameyev. Plasma Physics, V.16, pp.1036-1045 (1990)

# Hydrogen Compression in Cylindrical Targets Driven by a Coaxial Heavy Ion Beam

M. Temporal[1], J. J. Lopez Cela[1], A. R. Piriz[1], N. Grandjouan[2], N. A. Tahir[3] and D. H. H. Hoffmann[4]

1) ETSII, Univ. Castilla-La Mancha, Spain. 2) LULI, UMR, École Polytechnique, CNRS, CEA, Univ. Paris VI, France

3) Institut für Theoretische Physik, Universität Frankfurt, Germany. 4) TU Darmstadt and GSI Darmstadt, Germany.

The compression of a cryogenic hydrogen cylindrical sample contained in a hollow gold target driven by an intense co-axial uranium beam has been studied[1]. The study aims to find a window in the beam-target parameters for which hydrogen metallization is expected.

The target consists of a gold layer with a density $\rho_{Au} = 19.3$ g/cm$^3$ that encloses a cylindrical cryogenic hydrogen sample having a density $\rho_H = 0.0886$ g/cm$^3$, temperature $T_H = 10$ K, radius $r_H$ and target length $L_H$. An intense uranium ion bunch axially irradiates the target as schematically shown in Fig. 1. The bunch is supposed to deliver $N_U$ uranium ions in a pulse which has a particle distribution that is Gaussian in space and parabolic in time.

In Fig. 1 we also shown a cylindrical gold beam stopper with $r_{off} > r_H$ designed to shield completely the inner hydrogen sample from the direct heating of the ions.

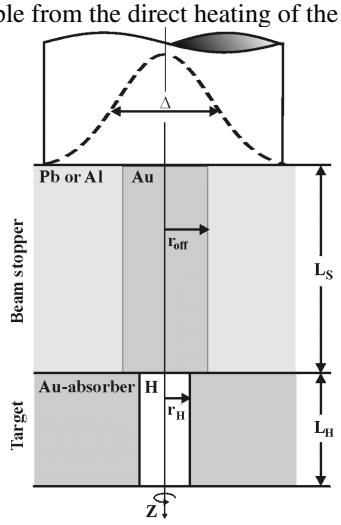


Fig. 1. Sketch of the target with a cylindrical block stopper located between the incoming ion beam and the hydrogen sample. The graph is not in scale.

The hydrodynamics of the target is analysed by means of one-dimensional numerical simulations (MULTI-1D[2]). A parametric study is performed to achieve the maximum average hydrogen density and temperature as a function of the sample radius, total number of ions and spread of the spatial ion distribution.

A first set of simulations has been performed by neglecting the beam stopper. In this way the hydrogen sample is directly heated by the Uranium ions. We optimised the final hydrogen conditions by varying the hydrogen radius as well as the spread of the ions distributions. In Fig. 2 we can see that is not possible to achieve a compression factor of 10 with a temperature below 0.2 eV as expected for hydrogen metallization.

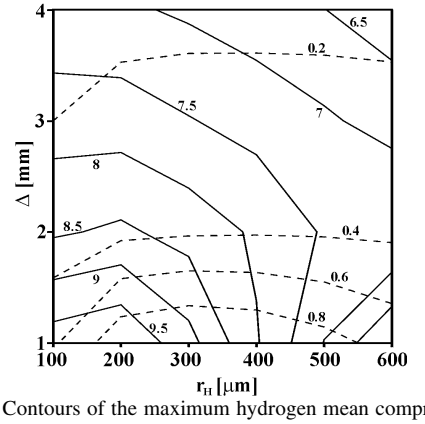


Fig. 2. Contours of the maximum hydrogen mean compression factor $\rho_M/\rho_H$ (solid line) and of the average temperature $T_M$ [eV] (dashed line) as a function of $\Delta$ and $r_H$. The ion beam has a pulse duration $\tau = 100$ ns delivering $N_U = 2\ 10^{11}$ uranium ions.

To avoid the direct hydrogen heating we have considered the beam block-stopper shown in Fig. 1. Another serie of simulations is presented in Fig. 3 as function of $\Delta r = r_{off} - r_H$ and $r_H$.

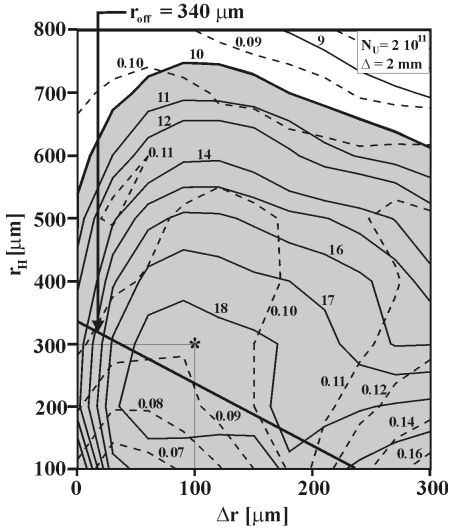


Fig. 3. Contours of the maximum hydrogen compression factor and temperature versus the hydrogen radius, $r_H$, and the parameter $\Delta r$. The shadowed area delimits the window where the compression factor is higher than a factor of 10 and the temperature is smaller than 0.2 eV.

A window in the beam-target parameters for which hydrogen compression is higher than a factor 10 and temperature is below 0.2 eV has been found (see the shadowed area in Fig. 3) by considering a single bunch that contains $2\ 10^{11}$ uranium ions delivered in 100 ns.

References.

[1] M. Temporal et al. submitted to *Phys. Plasmas*.

[2] R. Ramis et al. *Comp. Phys. Com.* **49**, 475-505 (1988).

# MBC-ITFIP: A 3D trajectory numerical simulation of the transport of energetic light beams in complex plasma targets

Manuel D. Barriga-Carrasco and Gilles Maynard

Laboratoire de Physique des Gaz et des Plasmas, bât. 210, CNRS-Université Paris XI, F-91405, Orsay

At Orsay we are currently developing a theoretical modeling and numerical simulations devoted to the problem of transport and energy deposition profile of high current light beams. Our research group has developed a numerical code to follow the trajectories of light atomic or molecular ions with dense and complex plasma targets MBC-ITFIP, which has been used before for solid targets [ 1, 2]. Here it is summed up in a few main points.

Atomic projectiles are supposed to experience two main interactions with the target material: (i) the collisions with the target electrons and (ii) the collisions with the target nuclei. Electronic collisions are the main cause of projectile stopping while nuclear collisions are the main cause of projectile scattering. The electronic stopping force is calculated by the dielectric formalism [3]. The nuclear collisions are taken into account by the classical theory of the dispersion using a Thomas-Fermi Coulomb screened potential with the universal screening distance [4].

Molecular projectiles inside the target first moves non-dissociated and after they dissociate into its constituent fragments. Non-dissociated molecular ions are assumed to experience the same interactions as an atomic projectile, (i) and (ii) [1]. When they dissociate, each fragment is subjected individually to the same type of atomic interactions (i) and (ii), plus other interactions related with the correlated motion of its fragment partners, namely: (iii) the Coulomb repulsion, when both dissociation fragments are charged, and (iv) the vicinage force, due to the electronic excitations induced in the target by the partner fragment. This vicinage forces are calculated using the same dielectric formalism as for the stopping force [2].

The simulation code uses a standard molecular dynamics method to follow the evolution of the particles, using a numerical integration of Newton equations. The timestep used in the computer code, $\Delta t$, is chosen to be less than the characteristic times of the interactions between the projectile and the target or between the projectiles, i.e. $\Delta t < \min(t_e, t_i, t_c, t_v)$.

The electronic stopping force, $S_p$, is obtained from a draw of a Gaussian distribution whose mean value is the electronic stopping $S_{p0}$ and with a variance $\Omega^2/\Delta z$, where $\Omega^2$ is the electronic straggling and $\Delta z = v\Delta t$, being v the velocity of the projectile in the timestep $\Delta t$.

The method used for the nuclear scattering is based on the binary collision model described by Möller et al. [5] and on the Monte Carlo simulation method developed by Zajfman et al. [6]. In order to reduce computer time, only rare events corresponding to large scattering angles are considered by the Monte Carlo draw while multiple scattering small angles are treated as continuum processes.

This numerical code has been applied first to study the fast ignition scenario (FIS) of the inertial fusion targets [7]. Also we have started to use it to plasma radiography. In a recent future it could be used to the plasma diagnostic by proton imaging [8] and to study the isochoric heating of solids to be converted into plasmas [9].

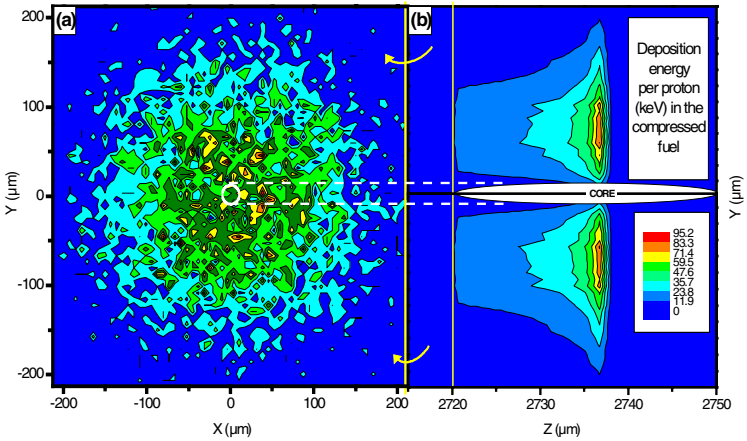


Fig.1 Radial and deposited energy distribution of protons arriving to the compressed fuel in the FIS.

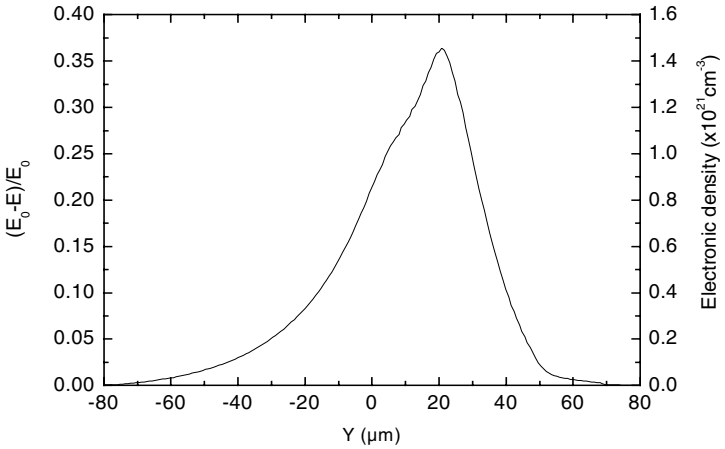


Fig.2 Plasma electron density radiography from proton energy loss.

## References

1. R. Garcia-Molina and M. D. Barriga-Carrasco, Phys. Rev. A 68, 054901 (2003).
2. M. D. Barriga-Carrasco and R. Garcia-Molina, Phys. Rev. A 68, 062902 (2003).
3. I. Abril et al., Phys. Rev. A 58, 357 (1998).
4. M. Nastasi, J. W. Mayer and J. K. Hirvonen, *Ion-Solid Interactions* (Cambridge University Press, 1996).
5. W. Möller, G. Pospiech and G. Schrieder, Nucl. Instr. Meth. 130, 265 (1975).
6. D. Zajfman et al., Phys. Rev. A 41, 2482 (1990).
7. M. Roth et al., Phys. Rev. Lett. 86, 436 (2001).
8. M. Borghesi et al., Plasma Phys. Control. Fusion 43, A267 (2001).
9. P. K. Patel et al., Phys. Rev. Lett. 91, 125004 (2003).

# Simulations of fast electron transport experiments at MPQ

J.J. Honrubia[1], M. Kaluza[2], G.D. Tsakiris[2], and J. Meyer-ter-Vehn[2]
[1]ETSII, Universidad Politécnica, Madrid, Spain; [2]Max-Planck-Institut für Quantenoptik, Garching, Germany

Recent experiments of electron transport and proton acceleration carried out at MPQ involve electron propagation in non-uniform plasmas [1]. These plasmas are generated by a shock wave launched into the target by a long ASE prepulse. When the high-intensity laser pulse interacts with the target, the generated fast electrons pass through a initially high resistivity expanding plasma with densities lower than solid and temperatures of a few eV. The high resistivity is due to the lack of the contribution of ion correlations found in solid conducting media. We have analysed the field generation process and its consequences on electron propagation by means of hybrid PIC simulations [2, 3, 4].

Aluminium targets with initial thickness in the range 5 - 30 $\mu m$ were illuminated by an ASE prepulse of 2.5 ns with an irradiance of $10^{12}$ $W/cm^2$. The prepulse is followed by the high intensity pulse, which delivers an energy of 0.42 J onto a focal spot of 5 $\mu m$ in 150 fs (fwhm), which corresponds to a mean intensity at fwhm of $1.5 \times 10^{19} W/cm^2$. The laser-to-fast electron conversion efficiency has been taken as 25%. The mean and peak kinetic energies of electrons are 800 keV and 950 keV respectively. Electrons with such high kinetic energy interact weakly by collisions with the thin targets used.

We have considered fast electron transport in a region with densities such that an almost perfect neutralisation of the fast electron current can take place, i.e. ratio of fast electron to background electron densities less than $10^{-2}$. An exponential density profile with maximum and minimum densities of $\rho_0$ and $\rho_0/10$, where $\rho_0$ is the density of solid aluminium, and an initial temperature of 5 eV have been assumed. Plasma resistivities are calculated by the model of Lee and More [5].

Collimation and energy loss of electrons in targets at solid density and in targets with the density profile assumed ('expanded targets') have been compared to analyse the effects of density profiles in electron propagation. Both types of targets have the same areal density.

Results depicted in Fig. 1 show a significant enhancement of the energy deposited to the plasma by resistive heating in expanded targets when compared with the energy deposited in solid targets. This enhacement is not accompanied, however, by an increase in the beam collimation. Figure 2 shows the ratio between the diameter of the electron beam at the rear ($d_{rear}$) and front ($d_{front}$) surfaces as a function of the areal density. This ratio is lower and depends more weakly on the thickness for solid targets, which evidences a higher beam collimation in solid targets. This can be explained by the lower resistive heating of the background, which leads to lower plasma temperatures and bigger field generation. Notice that collimation is largely reduced when the injection half-angle is increased from 30 to 40 degrees [6].

Results show that field generation has to be taken into account even in thin targets, where a significant energy

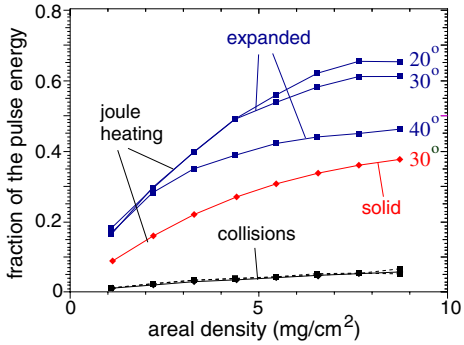


Figure 1: Energy balance of the expanded and solid targets. Electron injection half-angle is taken as a parameter. Areal densities of the expanded targets are computed with the mean density ($1.092\ g/cm^3$).

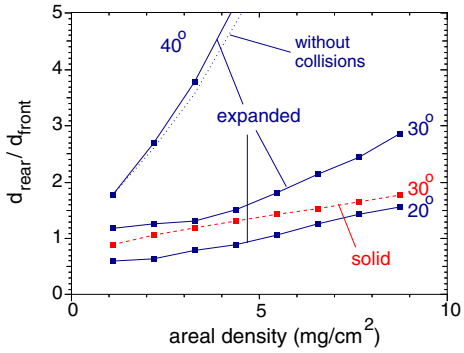


Figure 2: Ratio between diameters of the electron beam at the front and rear surfaces of the solid and expanded targets. Dash-dot line corresponds to solid targets

fraction of electrons ($\approx$ 17%) can be transferred to the plasma by resistive heating. This, together with the collimation of the electron beam, can be useful to intepret experiments on proton acceleration as a diagnostic of fast electron transport. If one assumes that electrons propagate freely through the expanded targets, the spot at the rear surface will be significantly bigger and electrons will carry more energy. The differences are not important in thin targets if electrons are not strongly collimated, which depends on the emission half-angle of fast electrons, as can be seen in Fig. 2.

## References

[1] M. Kaluza et al., accepted in Phys. Rev. Lett.
[2] J.J. Honrubia et al., GSI Annual Report 2002 (2003).
[3] J.J. Honrubia et al., Las. Part. Beams **22**, 137 (2004).
[4] A. Macchi et al., Nuclear Fusion **43**, 362 (2003).
[5] Y.T. Lee and R. More, Phys. Fluids **25**, 1273 (1984).
[6] A.R. Bell and R.J. Kingham, Phys. Rev. Lett. **25**, 035003 (2003).

# Photopumping of XUV Lasers by XFEL Radiation

Ke Lan[1,2], Ernst Fill[1], and Jürgen Meyer-ter-Vehn[1]

[1]MPQ, Garching; Germany, [2]Institute of Applied Physics and Computational Mechanics, Beijing, China

Within the next year the XUV Free-Electron Laser (XFEL) now under construction at DESY is expected to generate highly collimated XUV pulses with $10^{13}$ photons and a duration of 100 fs. Focusing this radiation to a spot some 10 μm in diameter generates intensities of up to $10^{16}$ W/cm$^2$. Such pump intensities make the investigation of photo-pumped XUV lasers feasible. We present simulations taking into account two different mechanisms generating the gain: 1. Photoionization with subsequent three-body recombination which takes advantage of the monochromaticity of the pump radiation to generate cold electrons [1]; 2. innershell ionization in which transient inversion is obtained by generating a hole in an otherwise completely filled shell [2]. The simulations show that under appropriate conditions both mechanisms generate high gain [3]. However, further issues must be considered, such as propagation of the pump pulse in the medium to be pumped.

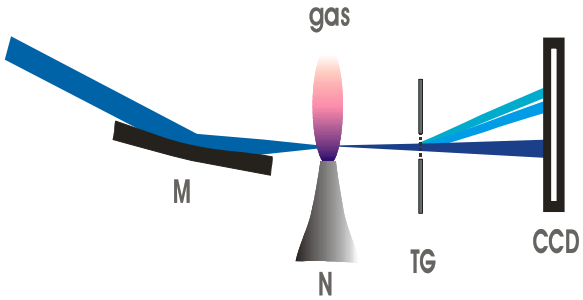


Fig. 1: Layout of the experiment. M: mirror; N: nozzle; TG: transmission grating.

A layout of the proposed experiment is shown in fig. 1. The XFEL pump source is weakly focused by a grazing-incidence elliptical mirror into a helium gas puff. The generated radiation is dispersed in a transmission grating spectrometer (to separate it from the pump radiation) and detected with a soft X-ray CCD. The simulations calculate the electron temperature $T_e$ resulting from photoionization and collisional and radiative processes, with the main contribution being due to three-body recombination. The time-dependent occupation of the levels is calculated by means of a collisional radiative code.

## 1. XUV lasers in He I and He II

The He I laser uses 25 eV pump photons (just above the ionization potential of 24.6 eV) to generate gain on the He-α transition at 58.4 nm. The temporal evolution of the gain is shown in fig. 2 for different densities $N_0$. The shape of the pump pulse is also included. Gains of the order of 100 cm$^{-1}$ are generated.

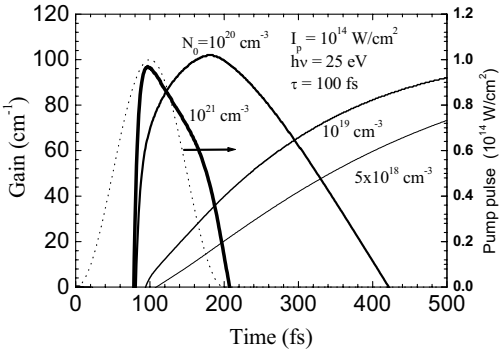


Fig. 2: Temporal evolution of He I laser gain for different densities. The pump pulse is shown dotted.

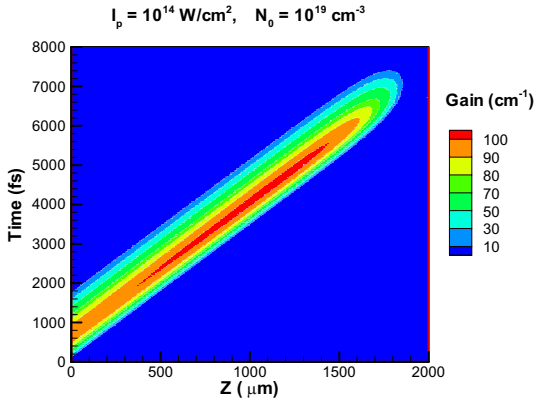


Fig. 3: Contour plot of the gain coefficient of the He I laser.

To attain a high gain length product the pump pulse must propagate through the medium for a sufficiently long distance. Saturation requires $gL > 15$. In fig. 3 we show a contour plot of the gain for a helium density of $10^{19}$ cm$^{-3}$ at a pump intensity of $10^{14}$ W/cm$^2$. In spite of a high absorption coefficient the pump propagates a distance of almost 2 mm into the medium. This can be understood by realizing that the helium ground state is strongly depleted. A gain length product >15 is achieved under this condition.

The He II laser operates on the Lyman-α transition of hydrogenic helium with a wavelength of 30.4 nm. In fig. 4 the time-dependent gain coefficient for the He II Lyman-α transition at different densities is displayed. The pump intensity is $10^{15}$ W/cm$^2$, a factor of 10 higher than that used for He I. Here the gain only slowly rises for $10^{19}$ cm$^{-3}$ and does not reach a high value. This is due to inefficient ionization of helium gas by the 55 eV photon. At higher densities the gain again reaches very high values. The simulations exhibit an intensity window for the gain, i.e. too low an intensity generates only low gain, but an intensity which is too high also results in small gain. This result can be understood by realizing that high intensity leads to high electron temperature by inverse brems-strahlung heating. The gain is further reduced by ionization from the upper laser level.

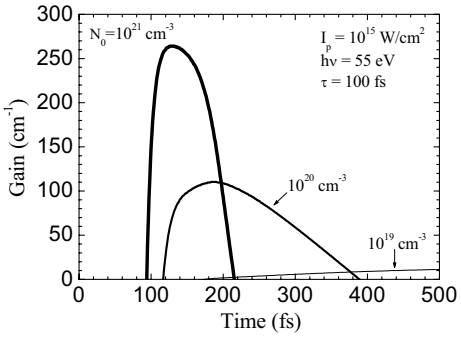


Fig. 4: Temporal evolution of He II gain for different electron densities.

## 2. Li II innershell laser

We present simulation results for the case of an innershell laser [2] pumped by an XFEL. Interest in innershell lasers derives from the fact that the states forming the upper laser level are already occupied and, thus, very high gain should be generated. In general, innershell lasers suffer from a high rate of loss of inversion due to the Auger effect. However, the problem of the Auger transition is not pertinent if the atom contains only a single outer electron, as in Li and Na. Ionization of a 1s electron of neutral lithium generates gain at the He-α line of Li II with a wavelength of 19.9 nm. However, transfer of the 2s electron of the neutral to the 2p level is required. This is possible by means of a visible laser tuned to the 2s – 2p resonance line of atomic lithium at $\lambda = 671$ nm. Figure 5 shows the result of a simulation of the gain on the He-α line of Li II for a pump intensity of $10^{14}$ W/cm$^2$, a pump photon energy of 68 eV and at densities ranging from $10^{18}$ to $10^{21}$ cm$^{-3}$.

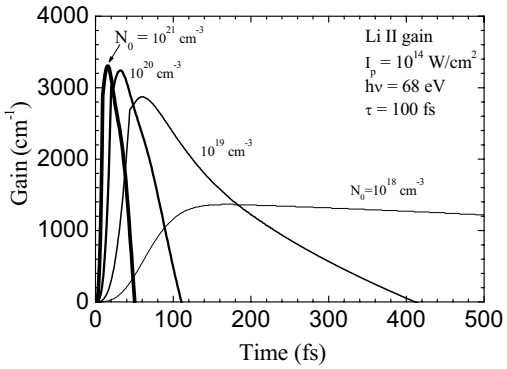


Fig. 5: Time-dependent gain of Li II laser.

The figure shows that very high gain is indeed generated at 19.9 nm. The duration of the gain is limited by collisional ionization of the electron in the n = 2 level. At $10^{20}$ cm$^{-3}$ the gain duration is 60 fs and at the (somewhat hypothetical) density of $10^{21}$ cm$^{-3}$ the gain lasts only for 30 fs. These conditions would thus lead to considerable shortening of the laser pulse compared with the pump pulse, a feature most welcome for many experiments.

[1] D. G. Goodwin and E. E. Fill, J. Appl. Phys. **64**, 1005 (1988).
[2] M. A. Duguay and P. M. Rentzepis, Appl. Phys. Lett. **10**, 350 (1967).
[3] K. Lan, E. E. Fill, and J. Meyer-ter-Vehn, Europhys. Lett. **64**, 454 (2003).

# Giant Enhancement of Inverse Bremstrahlung in Cluster Media

P. Mulser[1], M. Kanapathipillai[2], D. H. H. Hoffmann[2], and T. Schlegel[3]

[1] *Theoretical Quantum Electronics(TQE), Schlossgarten Str.7, Darmstadt University of Technology, D-64289 Darmstadt.*
[2] *Nuclear Physics Institute, Schlossgarten Str.9, Darmstadt University of Technology, D-64289 Darmstadt.*
[3] *Gesselschaft für Schwerionenforschung, Plank Str. 1, D-64291 Darmstadt. Germany.*

Intense laser radiation impinging on clustered media shows: (1) increased degree of ionization, (2) highly stripped energetic ions in the 100 keV range and higher, (3) intensified emission of harmonics of the laser frequency, (4) amplified X-ray emission, both, lines and continuum, (5¿) enhanced neutron production from D-D reactions. Consequence: Clustering leads to enhanced laser beam-plasma coupling [1]. Particle-in-cell (PIC) simulations confirm this[2]; however the underlying physics remains unclear. We show that giant enhancement of collisional heating takes place due to coherent superposition of electron-ion collisions.

Consider a hydrogen gas of uniform particle densities $n_{\rm i} = 10^{18}$ cm$^{-3}$ and $n_{\rm i} = 10^{20}$ cm$^{-3}$. It is assumed that the fraction $\xi$ of atoms forms clusters of radius $R = 1$, $R = 5$, and $R = 10$ nm and the remaining fraction $(1-\xi)$ represents a uniform background gas. The clusters are assumed to be totally ionized by field and collisional ionization in a very short time by the incident laser [3]. The additional free parameters to be fixed are the electron temperature $T_{\rm e}$ and the laser intensity $I$ at Ti:Sa wavelength of $\lambda = 800$ nm ($\omega = 2.35 \times 10^{15}$ s$^{-1}$). We choose $T_{\rm e} =$ 3 keV and 20 keV and $I = 10^{17}$ and $10^{18}$ W cm$^{-2}$. Introducing the "ionization" degree $\eta_C$ of a single cluster by $q_C = \eta_C Z_C e$, $\eta_C \le 1$, and keeping $\hat{v}_{\rm os}/v_{\rm th}$ ($\hat{v}_{\rm os}$ is the amplitude of $v_{\rm os}(t)$-the oscillation velocity, $v_{\rm th}^2 = T_{\rm e}/m_{\rm e}$) the same for both states, gas and clusters, the collision and absorption coefficients can be written as [4]

$$\begin{aligned} \nu_{\rm eC} &= \xi \eta_C^2 \frac{Z_C}{Z_i} \frac{L_C}{\ln \Lambda_{\rm ei}} \nu_{\rm ei}, \\ \alpha_{eC} &= \xi \eta_C^2 \frac{Z_C}{Z_i} \frac{L_C}{\ln \Lambda_{\rm ei}} \alpha_{\rm ei};\ \eta_C, \xi \le 1 \end{aligned} \qquad (1)$$

A picture of the scattering process is given in ref. [4]. $L_C$ is also given as [4],

$$L_{\rm C} = \frac{1}{2}\int_0^{\beta_{\rm c}} (1-\cos\chi)\beta d\beta + \frac{1}{2}\ln\frac{b_\perp^2 + b_{\rm max}^2}{b_\perp^2 + b_{\rm c}^2}. \qquad (2)$$

The cycle averaged cutoff $b_{\rm max}$ due to screening is

$$b_{\rm max} = \frac{(\hat{v}_{\rm os}^2/4 + v_{\rm th}^2)^{1/2}}{\omega_{\rm p}}, \qquad (3)$$

Here $\omega_{\rm p} = (n_{\rm e}e^2/\epsilon_0 m_{\rm e})^{1/2}$ is the plasma frequency associated with unclustered electron density and $b_\perp = \frac{e\eta Z_C}{4\pi\epsilon_0 m_e v^2}$ is the impact parameter for pependicular deflection by a point charge $e\eta_C Z_C$. In nearly all experiments with clusters $b_\perp << b_{\rm max}$ holds (weak coupling). It can be shown that effects due charge distribution inside the cluster are negligible.

Since the neutralizing electrons are quasi-free electrons both absorption coefficients obey the proportionalities $\alpha_{\rm eC} \sim n_e \nu_{\rm eC}$ and $\alpha_{\rm ei} \sim n_e \nu_{\rm ei}$. A lower limit of $\eta_C$ is determined under the assumption that the electrons in which the single cluster is embedded are in thermal equilibrium. The additional effect of $\hat{v}_{\rm os}$ on $\eta_C$ is ignored.

TABLE I: Amplification factors $\nu_{\rm eC}/\nu_{\rm ei}$ for hydrogen. Gas density $n_e = 10^{20}$ cm$^{-3}$; the values in brackets refer to $n_e = 10^{18}$ cm$^{-3}$. Cluster radius $R$ in nm; Laser intensities $I$ in Wcm$^{-3}$; $\eta_C$ ionization degree; $g = L_C/\ln\Lambda_{ei}$.

| $T_e = 1$ keV, $\xi = 1$ | | | | | | $T_e = 20$ keV, $\xi = 1$ | | |
|---|---|---|---|---|---|---|---|---|
| R | $Z_C$ | $\eta_C$ | $I$ | $g$ | $\nu_{\rm eC}/\nu_{\rm ei}$ | $g$ | $\nu_{\rm eC}/\nu_{\rm ei}$ | $\eta_C$ |
| 1.0 | 210 | 1.0 | $\le 10^{15}$ | 0.5 | **95 (112)** | 0.5 | **97** | |
| | | | $10^{17}$ | 0.4 | **93 (107)** | 0.3 | **63** | 1.0 |
| | | | $10^{18}$ | 0.5 | **95 (107)** | 0.2 | **48** | |
| 5.0 | 2.6e4 | 0.7 | $\le 10^{15}$ | 0.2 | **3.2 (3.9)e3** | 0.5 | **1.3e4** | |
| | | | $10^{17}$ | 0.3 | **3.6 (4.8)e3** | 0.3 | **8.7e3** | 1.0 |
| | | | $10^{18}$ | 0.3 | **4.0 (5.1)e3** | 0.3 | **6.6e3** | |
| 10.0 | 2.1e5 | 0.3 | $\le 10^{15}$ | 0.2 | **3.1 (5.9)e3** | 0.5 | **1.0e5** | |
| | | | $10^{17}$ | 0.2 | **4.1 (6.2)e3** | 0.3 | **7.0e4** | 0.99 |
| | | | $10^{18}$ | 0.3 | **5.9 (6.6)e3** | 0.3 | **5.4e4** | |

The resulting amplification factors $\nu_{\rm eC}/\nu_{\rm ei}$ together with the "ionization" degree $\eta_C$ for the cluster sizes $R = 1, 5, 10$ nm, particle numbers $Z_C$, and $g = L_C/\ln\Lambda_{\rm ei}$ are listed in Table I for $\hat{v}_{\rm os}^2 \ll v_{\rm th}^2$ (low laser intensity), $I = 10^{17}$ and $10^{18}$ W·cm$^{-2}$.

Amplification factors up to $10^5$ are achieved, corresponding to half of the ion number $Z_C$ in a cluster. They are lower limits. At low laser fluence $I\lambda^2$ or in very big clusters with resonance frequency $\omega_0^2 = \omega_p^2/3 \gg \omega^2$, the low laser intensity limit applies (first row of each cluster size). In particular this is the case with the high power XFEL.

**Conclusion:**

As calculated in detail enhancement of inverse bremstrahlung by many orders of magnitude may occur due to clustering of gas molecules.

## References

[1] Jan Posthumus (ed.), *Molecules and Clusters in Intense Laser Fields* (Cambridge Univeristy Press 2001, Chaps. 5, 6, 7).

[2] F. Greschik and R.-J.Kull, L & P Beams **18**, 367 (2000).

[3] D. Bauer and P. Mulser, Phys. Rev. A **59**, 569 (1999).
D. Bauer *et al.*, Laser Physics **9**, 58 (1999).

[4] P. Mulser and M. Kanapathipillai, GSI-2003-2.

# Chaos in Laser Beam-Cluster Interaction

M. Kanapathipillai[1] and D. H. H. Hoffmann[2]
[1] *Gesellschaft für Schwerionenforschung, Plankstr. 1, D-64291 Darmstadt.*
[2] *Institut für Kernphysik, Schlossgarten Str.9, Darmstadt University of Technology, D-64289 Darmstadt.*

As shown in [1] collective laser beam absorption by a cluster may be sucessfully described by regarding the cluster as consisting of a relatively massive positively charged ion core and a mobile light electron cloud. Such an assembly essentially constitutes a global dipol. The set of nonlinear equations for the evolution of the global dipol interacting with the laser beam are presented in [1].

When one introduces formally an additional variable which is equal to time so as to make the system autonomous, the number of equations in the set becomes three, and the possibility of chaotic behaviour of the global dipol exists [2]. Indeed the apparently irregular behaviour of the absorption efficiency presented in Fig. 1 of [1] also suggests such a possibility. Therefore it is imperative to verify whether the laser-cluster interaction is chaotic when described within the framework of the global dipol model.

As a first step in this exploration we construct a bifurcation diagram [2]. Fig.1 shows such a bifurcation diagram which also strongly hints at a possible chaos in laser-cluster interaction. A conclusive proof of chaos is the existence of at least one positive Lyapunov exponent of the dynamical system [2]. Therefore we turn our attention to the evaluation of the Lyapunov exponents associated with the global dipol [3].

The equation of motion of the dipol given in [1] can be rewritten as,

$$\frac{dy_0}{d\tau} = \frac{y_1}{(1+y_1^2)^{1/2}} \tag{1}$$

$$\frac{dy_1}{d\tau} = -\nu \sin(\frac{2\pi y_2}{n}) \sin(2\pi y_2) - \delta^2 y_0 \frac{f(x)}{x} \tag{2}$$

$$\frac{dy_2}{d\tau} = 1, \tag{3}$$

where $y_0 = r/\lambda$, $y_1 = u_x/c$, $y_2 = \tau$, $\delta = 2\pi\omega_0/\omega, x = r/R$ and

$$f(x) = \begin{cases} x - \frac{9}{16}x^2 + \frac{1}{32}x^4 & \text{for} \quad x \le 2; \\ \frac{1}{x^2} & \text{otherwise.} \end{cases} \tag{4}$$

The set of linearised equations resulting from (4) is,

$$\frac{d}{d\tau}\begin{pmatrix}\Delta y_0 \\ \Delta y_1 \\ \Delta y_2\end{pmatrix} = \mathbf{D}\begin{pmatrix}\Delta y_0 \\ \Delta y_1 \\ \Delta y_2\end{pmatrix}, \tag{5}$$

with

$$\mathbf{D} = \begin{pmatrix} 0 & 1/(1+y_1^2)^{3/2} & 0 \\ d_{21} & 0 & d_{23} \\ 0 & 0 & 0 \end{pmatrix}, \tag{6}$$

where

$$d_{21} = -\delta^2\Big[f(x)/x + x\frac{d(f(x)/x)}{dx}\Big], \tag{7}$$

and

$$d_{23} = -2\pi\nu\Big[\frac{1}{n}\cos(\frac{2\pi y_2}{n})\sin(2\pi y_2) + \sin(\frac{2\pi y_2}{n})\cos(2\pi y_2)\Big]. \tag{8}$$

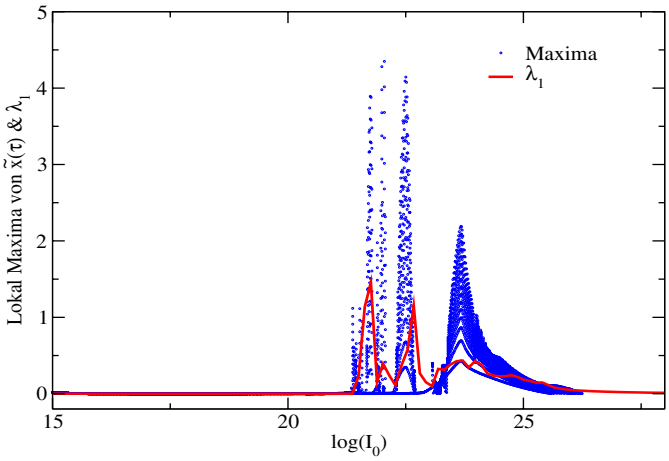


Figure 1: Amplitudes of $\tilde{x}(\tau)$ as a function of $\log(I_0)$ and the associated $\lambda_1$ spectrum for $\omega/\omega_0 = 0.3$ .

The eigenvalues of $\mathbf{D}$ are,

$$\mu_1 = -\mu_2 = (-d_{21}/(1+y_1^2)^{3/2})^{1/2} \tag{9}$$

$$\mu_2 = 0. \tag{10}$$

The Lyapunov exponents are, by definition, the real parts of these eigenvalues. Thus,

$$\lambda_1 = \begin{cases} <(-d_{21})^{1/2}/(1+y_1^2)^{3/4}> & \text{when} \quad d_{21} < 0; \\ 0 & \text{otherwise.} \end{cases} \tag{11}$$

$$\lambda_2 = -\lambda_1 \tag{12}$$

$$\lambda_3 = 0 \tag{13}$$

where <> denotes the averaging along the evolution trajectory in phase space.

The solid line in Fig.1 shows the $\lambda_1$ spectrum superimposed on the bifurcation diagramm. It is obvious that chaos occurs because $\lambda_1 > 0$.

**Conclusion:**

It has been shown that, in the framework of the global dipol model, laser-cluster interaction is chaotic. Not shown here is the fact that expansion of the electron cloud due to heating reduces the degree of chaos, as measured by the value of the largest Lyapunov exponent.

## References

[1] M. Kanapathipillai, *A Simple Model of Nonresonant Laser Absorption in Clusters*, High Energy Density Physics with Intense Laser and Ion Beams, Annual Report 2002, p.42, Gesellschaft für Schwerionenforschung, Darmstadt.

[2] R. C. Hilborn,*Chaos and Nonlinear Dynamics*, Cambridge University Press, Cambridge, 1994.

[3] T. S. Parker and L. O. Chua, *Practical Numerical Algorithms for Chaotic Systems*, Springer Verlag, New York, 1989.

# 4 CONTRIBUTIONS OF SPEAKERS FROM THE WORKSHOP ON THE FUTURE ACCELERATOR FACILITY AT GSI IN OCTOBER 2003

# Challenges and opportunities for collaborations in High Energy Density Physics

T.A. Mehlhorn [1]

[1]Sandia National Laboratories, Albuquerque, New Mexico, USA

According to the National Research Council of the National Academy of Sciences „The time is highly opportune … to develop a fundamental understanding of the physics of high energy density plasmas. Recent advances in extending the energy, power and brightness of lasers, particle beams, and Z-pinch generators make it possible to create matter with extremely high energy density in the laboratory. The collective interaction of this matter with itself, particle beams, and radiation fields is a rich, expanding field of physics called high energy density physics. It is a field characterized by extreme states of matter previously unattainable in laboratory experiments" [1].

High energy density physics (HEDP) is defined as an energy density of $10^{11}$ J/m$^3$ that is equivalent to a pressure of 1 Mbar. HEDP research is a world wide activity utilizing high power lasers, z-pinches and particle beams. An active collaboration in HEDP physics already exists between German and US researchers including Oliver Boine-Frankenheim, Markus Roth, and Mathias Geissel (Sandia National Labs) and Andreas Tauschwitz, Christoph Niemann and Stefan Neff (Lawrence Berkeley Nat. Lab).

Within the next two decades, new facilities will revolutionize both our understanding and use of plasma physics including the National Ignition Facility at LLNL, ITER, the 26 MA ZR at Sandia, the FIREX1 facility at ILE Osaka, and the SIS 100/200 accelerator at GSI. Sandia performs its HEDP research on a combination of Z and ZBL. The "Z Machine", which is located at Sandia is a pulsed-power accelerator that drives z-pinch loads producing x-ray powers of 100-250 TW and 1-1.8 MJ of radiated x-ray energy. The Z-Beamlet laser (ZBL) is operational and is used on about half of all Z experiments delivering >2 kJ (<2 ns) via a 75-m-length transport tube to Z. ZBL is being upgraded to provide a 2-4 kJ, 1-10 psec short pulse laser for high energy radiography and fast ignitor experiments on Sandia's Z facility beginning in 2007. A stand alone 50-200 J, 0.5 - 10 psec prototype laser system will begin operation in 2004.

GSI likewise has both an accelerator and a laser for HEDP research. The SIS 100 will be a valuable HEDP facility with the highest specific ion deposition capability in the world. It is important to note that higher beam intensites and shorter bunches are critical to HEDP all HEDP research at GSI. The PHELIX, Petawatt High Energy Laser for Heavy Ion Experiments is being constructed at GSI. PHELIX utilized a US/German collaboration: "... related to use of Nova laser parts to build a new Petawatt laser facility at GSI ... 5 transportainers of Nova parts were shipped under the auspices of OFES and the LBNL Heavy-Ion Fusion Program to GSI in November, 2002". PHELIX experiments with the UNILAC beam (1 kJ in 0.5 - 10 ns) are planned in 2004, while a petawatt (PW) capability (500J in 500 fs) is planned for 2005. The SIS 100 coupled with PHELIX will greatly increase the capability and flexibility for high energy density physics at GSI.

An Implementing Agreement between the US-DOE and the German-BMBF on Collaboration in the Field of Dense Plasma Physics already exists. Collaboration may include the following: 1) the study of plasma properties in extreme regimes of density and temperature, 2) the study of energy deposition, x-ray conversion and transport of radiation in dense plasmas, 3) the study of the production and spectroscopy of highly charged ions, 4) research on the interaction of intense laser light with overdense plasmas, 5) experiments on heavy ions; and 6) the development of a database on bunch-compression, focusing, and target plasma interaction physics using intense, multi-Giga-electronvolt heavy-ion beams. A new annex on gas desorption and electron cloud effects in high intensity accelerators has been proposed.

New HEDP collaborations are proposed . The US Heavy Ion Fusion program is interested in leveraging the unique capability at GSI to measure ion stopping powers. Sandia is interested in collaborating in obtaining GSI data in EOS, conductivity and critical points. A theoretical collaboration in exact exchange for density function theory is already in place with R. Redmer (U. Rostock). The controversial deterium EOS is important to both ICF and to Jovian/extrasolar planetary science. Heavy Ions from SIS 100 with innovative targets should create diagnosable warm dense matter (WDM) utilizing volume deposition via "slow" cylindrical isentropic implosion to create „shocklessly imploded" hydrogen with a 50 ns dwell time. GSI has already made a first measurement of electrical conductivity in ion beam heated materials [2]. Sandia is also interested in collaborations in the atomic physics & spectroscopy of dense plasmas. Short pulse, high intensity lasers can both heat and diagnose plasmas. Common research areas of interest in PW laser physics and applications include: 1) ion generation, 2) ion sources, 3) isochoric heating, 4) dE/dx in warm dense matter, and 5) proton deflectometry measurements of transient electromagnetic fields.

## References

[1] *Frontiers in High Energy Density Physics*, NRC 2003, National Academies Press.

[2] S. Udrea, Laser and P art. Beams 20 (2002) 399

# Atomic Processes in Dense Plasmas

Valery S. Lisitsa
Nuclear Fusion Institute, Russian Research Center Kurchatov Institute

**Atomic physics in Warm Dense Matter (WDM): background and justification**

There is a strong coupling between atoms and plasmas under WDM conditions [1]. In essence photons are radiated in WDM by a compound system "ATOM + PLASMA". The coupling parameter $\Gamma$ is the ratio of interparticle potential energy to the thermal energy .WDM production is supposed to be done by means of heavy ions beams at GSI. Atomic collisions in dense plasmas are characterized by a collision time $\tau_c \sim \rho_{eff}/v$ and kinetic time $\tau_k \sim [Nv\pi\rho_{eff}^2]^{-1}$. Their ratio is equal to $g=N\rho_{eff}^3$ that is just a number of particles inside the interaction sphere. Binary collisions correspond to $g<<1$ whereas multiparticle collisions in dense plasmas corresponds to $g>>1$. For dipole allowed collision transitions the long range interaction in plasmas can be expressed in terms of plasma electric field F(t). It results in the conception of plasma microfield leading to the atomic state mixing by plasma microfield [2]. Density matrix equations are needed instead of atomic amplitude equations in standard approach [3].

**Effects for observations**

One of the most important effects is the effect of plasma coupling parameter $\Gamma$ on microfield distribution and microfield dynamics. Spectral line shapes are of a special interest for atoms in plasma microfield making it possible to determine ion density, microfield dynamic effects ( field life-time $T_F$) due to ion thermal motion and plasma coupling parameter $\Gamma$. A cut off of atomic energy levels as a function of plasma density can be observable also. Molecular satellites in far wings of spectral lines (observed in laboratory laser plasmas [4] and white dwarf plasma [5]) can be used for a determination of WDM investigations.

**Stopping Power Measurements**

A general idea is to observe space resolved spectra generated by a fast projectile in a dense media. Polarization Radiation (PlR) of fast particles in a dense medium is of a special interest. The PlR can be considered as a scattering of the proper electromagnetic field of the fast charged particles in collisions with target atoms [6]. The PlR from fast electrons have been observed for polycristalline Al target. A sharp increase of PlR intensity is proposed for highly charged ions with a charge Z.

The PlR intensity scales as $Z^2$ that means a sharp increase of the effect. The calculations of PlR for Al and frozen hydrogen targets demonstrate that 1) the quantity of emitted quanta are enough for observation of the effects in experiments with projectile bunches $10^{10}$ particles; 2) spectra are dependent on the projectile energy E that means a new way for stopping power measurements; 3) spectra are sensitive to the medium structure being a way for WDM structure determination. The results of PlR spectra measurements can be compared with X-ray scattering spectra from PHELIX.

**Conclusion**

New possibilities of accelerators facilities make it possible to observe a number of effects connected with exotic WDM state. The hydrogen spectra measurements open new possibilities for investigations of nonideal plasma properties in the first turn – statistical and dynamical properties of plasma microfield in the strongly coupled plasmas. New methods of PlR measurements open new possibilities for stopping power measurements in a dense media as well a structure of WDM itself.

**References**

[1] Kozyreva, A., Basko, M., Rosmej, F.B., Schlegel, T., Tanschwitz, A., Hoffmann, D.H.H., Phys. Rev. E, 056406(2003)
[2] Griem, H.R., Principles of Plasma Spectroscopy, Cambridge University Press, 1997
[3] Lisitsa, V.S., Atoms in Plasmas, Springer, Heildelberg, 1994
[4] Lebuocher-Dalimier, E., Poquerusse, A., Angelo, P., Phys. Rev. E**47**, R1467(1993)
[5] Allard, N.F., Kielkopf, J.F., Drira, I., Eur. Phys.J.D,**12,**263(2000)
[6] Astapenko, V.A., Bureyeva, L.A., Lisitsa, V.S., In Review of Plasma Phys. Ed. by V.D. Shafranov, Kluwer Academic Publisher, v.23, p.1-205(2003)

# X-ray Scattering from PHELIX Plasmas

David Riley [1] Frank B Rosmej [2]

[1]Queen's University of Belfast, University Road, Belfast BT7 1NN, UK

[2]Universite de Provence et CNRS, UMR 6633, Centre de Saint Jerome, case 232, F-13397 Marseille cedex 20, France

Warm dense matter (WDM) is a regime where neither classical plasma physics nor condensed matter models are applicable. In the former this is because of the effects of strong coupling and degeneracy and the breakdown of the statistical averaging necessary for the Debye screening model. In the latter it is because the temperature at solid density is greater than a small fraction of the Fermi temperature. This regime is generally taken to include densities within a factor of ten of solid density and temperatures ranging from about 1-10eV. The study of WDM is currently of great interest due to its relevance to planetary science and the fact that in this regime, equation of state models disagree- especially off the shock Hugoniot.

Making samples of WDM suitable for study in the laboratory is difficult. Laser-plasma generated samples tend to suffer from steep density and temperature gradients and are short lived (~ns). The ion beam facility at GSI offers the chance to make large uniform samples with scale times of ~100ns. We propose to make use of such samples and probe them with 1ns pulses of X-ray line radiation generated by the PHELIX laser. The diagnostic is X-ray Thompson scatter. This techniqe has only recently been developed [1]. We intend to use the ~1kJ available to generate ~$10^{15}$ photons [2] of Ti He-alpha ($1s^2$-$1s2p\ ^1P$) line radiation at 4.75keV. This is generated along with Li-like satellites to form a line array of ~50eV spectral width. Kozyreva *et. al.* [3] have shown that a cylindrical frozen hydrogen sample can be heated with heavy ions to create a uniform plasma with density ~0.05g/cc at ~0.6eV with a length of ~1mm and diameter ~0.6mm. Given that the equation of sate for dense hydrogen continues to be a matter for debate, [4] this presents an interesting potential sample for X-ray scattering. Figure 1, shows a schematic of the proposed experiment. We can consider how many X-rays are likely to be scattered. The X-ray source sample (Ti foil) can be placed within 5mm of the sample. A pinhole system can be used to restrict the probe to a fixed diameter of the target. Assuming this is done and the probe subtends ~0.3mm on the target we can estimate that ~$10^{12}$ photons probe the target. The scatter cross-section depends on the scatter angle chosen but is ~$4x10^{-26}$ $cm^2$/sr. As an aside, we should state that the angle of scatter determines if the scatter is in the collective or non-collective mode. In the former we sample fluctuations on a longer spatial scale than the Debye length and expect to see a plasmon feature in the scatter spectrum, in the latter we probe shorter spatial scales and expect to see a spectrum reflecting the Doppler shifts due to thermal motion of the electrons. Give the size of the plasma we expect to see at least $10^8$ photons/sr scattered. With a spatially resolving imaging crystal we can achieve a throughput of $10^{-4}$ sr and thus capture $10^4$ photons per data shot. Given the high detection efficiency of modern CCD X-ray detectors, this is enough to make a spectrum. The expected spectra should differ from optical spectra in that the Compton shift of scattered photons (0-90eV) is noticeable and the spectrum is not symmetric since the structure factors on either side of the central wavelength are related by $S(-\omega,k)\sim e^{-\hbar\omega/kT}S(\omega,k)$. This is not important, in the optical case ($\hbar\omega<<kT$) but is for X-rays and collective scatter would yield a single plasmon peak shifted by the plasma frequency plus Compton shift from the incident wavelength. Theoretical work on X-ray Thomson scatter spectra, looking at the effects of strong coupling and degeneracy has been started [5] and is expected to be stimulated further by the availability of data from interesting samples such as dense hot hydrogen.

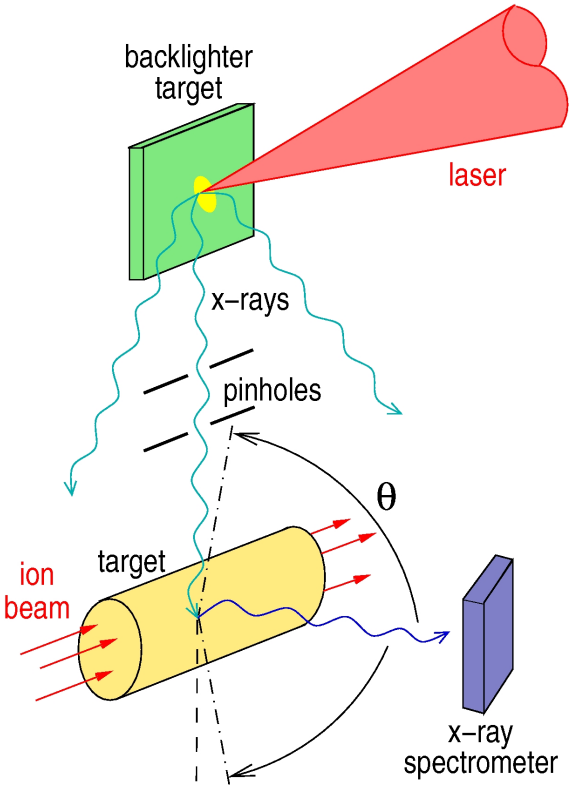


Figure 1. Schematic of the proposed X-ray scattering experiment using ion-beam generated samples and laser-plasma x-rays as a probe.

## References

[1]SH Glenzer *et. al.* Phys. Rev. Lett. **90**, 175002-1, (2003)

[2] D Riley *et. al.* Plasma Sources Sci. Technol. **11**(4) 484-491 (2002)

[3] A Kozyreva, M Bask, FB Rosmej, T Schlegel, A Tauschwitz, DHH Hoffmann, Phys.Rev.E **68**(5)art. no.056406 (2003)

[4] LB Da Silva *et. al.* Phys. Rev. Lett. **78**(3) p483 (1997), MD Knudson *et. al.* Phys. Rev. Lett. **87**(22) art. no. 225501 (2001)

[5] G Gregori *et. al.* Phys. Rev. E **67** art. 026412 (2003)

# APPENDICES

# PARTICIPATING INSTITUTES

Gesellschaft für Schwerionenforschung
Planckstr. 1
D-64291 Darmstadt, Germany

Technische Universität Darmstadt
Institut für Kernphysik
Schloßgartenstr. 9
D-64289 Darmstadt, Germany

Technische Universität Darmstadt
Institut für Angewandte Physik
Schloßgartenstr. 7
D-64289 Darmstadt, Germany

Technische Universität Darmstadt
Inst. für Theoret. Quantenelektronik
Hochschulstr. 4
D-64289 Darmstadt, Germany

Johann-Wolfgang-Goethe-Universität
Institut für Angewandte Physik
Robert-Mayer-Str. 2-4
D-60325 Frankfurt am Main, Germany

Johann-Wolfgang-Goethe-Universität
Institut für Theoretische Physik
Robert-Mayer-Str. 8-10
D-60325 Frankfurt am Main, Germany

Justus-Liebig-Universität Gießen
Inst. für Kernphysik (Strahlenzentrum)
Leihgesterner Weg 217
D-35392 Gießen, Germany

Universität Erlangen
Institut für Theoretische Physik II
Staudtstr. 7
D-91058 Erlangen, Germany

Max-Planck-Institut für Quantenoptik
Hans-Kopfermann-Str. 1
D-85748 Garching, Germany

Ernst-Moritz-Arndt-Universität
Fachbereich Physik
Domstr. 10a
D-17489 Greifswald, Germany

Universität Rostock
Fachbereich Physik
Universitätsplatz 3
D-18051 Rostock, Germany

L.P.G.P., Bat. 212
Universite Paris Sud
F-91405 Orsay Cedex, France

LULI
Ecole Polytechnique
F-91128 Palaiseau, Cedex, France

PIIMA
Université de Provence
F-13397 Marseille, Cedex 20, France

ENEA
Via E. Fermi 27
I-00044 Frascati RM, Italy

E.T.S.I. Aeronautics
P. Cardenal Cisneros 3
Universidad Politecnica, Madrid
E-28040 Madrid, Spain

E.T.S.I. Industriales
Universidad de Castillia La Mancha,
E-13071 Ciudad Real, Spain

Institute for Theoretical and
Experimental Physics
Cheremushkinskaya Avenue 25
Ru-117259 Moscow, Russia

Institute of Problems of Chemical
Physics
Ru-142432 Chernogolovka, Russia

RFNC-VNIIEF
37 Mir-Avenue
Ru-607200 Sarov, Russia

Weizman Institute of Science
P.O. Box 26
Rehovot 76100, Israel

Lawrence Berkeley National Laboratory
(LBNL)
1 Cyclotron Road
Berkeley, CA 94550, USA

Lawrence Livermore National Laboratory
(LLNL)
P.O. Box 808
Livermore, CA 94550, USA

# PUBLICATIONS

Intense, High-Quality Ion Beams Generated by Ultra-Intense Lasers
M. Roth, T.E. Cowan, J.-C. Gauthier, J. Meyer-ter-Vehn, M. Allen, P. Audebert, A. Blazevic, E. Brambrink, J. Fuchs, M. Geissel, M. Hegelich, S. Karsch, A. Pukhov, H. Ruhl, T. Schlegel
AIP Conf. Proceedings: 14ht Int. Conferece on High Power Beams and 5th Int. Conference on Dense Z-Pinches, Albuquerque, NM, 2002, AIP Conference Proceedings, 650p. 485-490 (2003)

Strongly Coupled Laser Produced Plasmas: Investigation of Hollow Ion Formation and Line shape Analysis
F. Rosmej, A. Calisti, R. Stamm, B. Talin, C. Moss, S. Ferri, M. Geissel, D.H.H. Hoffmann, A. Faenov, T. Pikuz
Journal of Quantitative Spectroscopy & Radiative Transfer 81, 395-409 (2003)

High Power Production Target Calculations for a Fast Extraction Scheme
N.A. Tahir, M. Winkler, J. Kojouharova, P. Roussel-Chomaz, V. Chiskin, H. Geissel, D.H.H. Hoffmann, B. Kindler, F. Landre-Pellmoine, B. Lommel, W. Mittig, G. Münzen-berg, A. Shutov, H. Weick, M. Yavor
Nucl. Intr. Meth. B204, 282, (2003)

Influence of the Equation of State on the Compression and Heating of Hydrogen
N.A. Tahir, H. Juranek, A. Shutov, R. Redmer, A.R. Piriz, M. Temporal, D. Varentsov, S. Udrea, D.H.H. Hoffmann, C. Deutsch, I. Lomonosov, V.E. Fortov
Phys. Rev. B 67, 184101(1-7) (2003)

Influence of the Equation of State of Matter and Ion Beam Characteristics on Target Heating and Compression
N.A. Tahir, A. Shutov, D. Varentsov, P. Spiller, S. Udrea, D.H.H. Hoffmann, I.V. Lomo-nossov, J. Wieser, M. Kirk, R. Piriz, V.E. Fortov, R. Bock
Phys. Rev. Spec. Top. 6, 020101, 1 (2003)

The Creation of Strongly Coupled Plasmas Using an Intense Heavy Ion Beam: Low-Entropy Compression of Hydrogen and the Problem of Hydrogen Metallization
N. A. Tahir, A.R. Piriz, A. Shutov, D. Varentsov, S. Udrea, D.H.H. Hoffmann, H. Juranek, R. Redmer, R.F. Portugues, I. Lomonosov, V.E. Fortov
J. Phys.A.: Math. Gen. 36, 6129 (2003)

Intense Heavy Ion Beams as a Tool to Induce High-Energy-Density States in Matter
N.A. Tahir, C. Deutsch, V.E. Fortov, V. Gryaznov, D.H.H. Hoffmann, H. Juranek, I.V. Lomonosov, A.R. Piriz, R. Redmer, A. Shutov, P. Spiller, M. Temporal, S. Udrea, D. Varentsov
Contribu. Plasma Phys. 43, 373 (2003)

Generation of Hollow Ion Beam: Calculation of the Rotation Frequency Required to Accommodate Symmetry Constraints
A.R. Piriz, N.A. Tahir, D.H.H. Hoffmann, M. Temporal
Phys. Rev. E 67, 017501 (2003)

Symmetry Analysis of Cylindrical Implosions Driven by a High-Frequency Rotating Intense Heavy Ion Beam
A.R. Piriz, M. Temporal, J.J. Lopez Cela, N.A. Tahir, D.H.H. Hoffmann
Plasma Phys. Controlled Fusion 45, 1733 (2003)

Fundamental Studies of Intense Heavy-ion-beam Interaction with Solid Targets
E. Dewald, C. Constantin, C. Niemann, S. Udrea, J. Jacoby, J. Wieser, D. Varentsov, N.A. Tahir, A. Kozyreva, A. Shutov, T. Schlegel, A. Tauschwitz, D.H.H. Hoffmann, R. Bock
IEEE Trans. Plasma Sc. 31, 221 (2003)

Solid Neon for Equation of State Studies
D. Varentsov, N.A. Tahir, I.V. Lomonosov, D.H.H. Hoffmann, J. Wieser, V.E. Fortov
Energy Loss Dynamics of an Intense Uranium Beam Interacting with
Europhys. Lett. 61, 57 (2003)

Effect of the Target Density on the Cross Section of Charge Exchange between fast Ions and Atoms
O. Rosmej, I.Yu. Tolstichina, V.P. Shevelko
JTP Vol. 48, N9, 1110 (2003)

Gas Density Measurements with Heavy Ion Beams
S. Neff, A. Tauschwitz, C. Niemann, D. Penache, D.H.H. Hoffmann, S.S. Yu, W. M. Sharp,
J. Appl. Phys., 93, 3079 (2003)

Laser-guided, Intersecting Discharge Channels for the Final Transport in Heavy-ion Fusion
C. Niemann, S. Neff, A. Tauschwitz, D. Penache, R. Birkner, C. Constantin, R. Knobloch,
R. Presura, F.B. Rosmej, D.H.H. Hoffmann, S.S. Yu,
J. Appl. Phys., 93, 9470 (2003)

Diagnostics of Discharge Channels for Neutralized Chamber Transport in Heavy Ion Fusion
C. Niemann, D. Penache, A. Tauschwitz, F.B. Rosmej, S. Neff, R. Birkner, C. Constantin, R. Knobloch, R. Presura, S.S. Yu, W.M. Sharp, D.M. Ponce, D.H.H. Hoffmann,
Laser and Particle Beams 21, 13 (2003)

Visible Light Spectroscopy of $Ar^{6+}$ Ions in High Rydberg States Produced with a Micro-capillary Target
Y. Morischita, Y. Kanai, K. Ando, R. Hutton, T. Brage, H.A. Tori, K. Komaki, Y. Yama-zaki, H. Masuda, K. Ishii, F.B. Rosmej
Nucl. Instr. Meth. B 205, 758 (2003)

Gravitational Lensing by the Sun of Non Relativistic Penetrating Particles
D.H.H. Hoffmann, J. Jacoby, and K. Zioutas
Astropart. Phys. 20, 73 (2003)

Research into the Advanced Experimental Methods for Precission Ion Stopping Range Measurements in Matter
I. Bakhmetjev, A. Fertman, A Golubev, A. Kantsyrev, B. Sharkov, V. Turtikov, V. Kunin, V. Vatulin, N. Zhidkov, E. Baldina, U, Neuner, J. Wieser, J. Jacoby, D.H.H. Hoffmann
Laser and Particle Beams 21, 1 (2003)

Numerical Study of K-alpha Emission from Partially Ionized Chlorine
T. Kawamura, T. Schlegel, H. Nishimura, K. Koike, Y. Ochi, R. Matsui, S. Okihara, S. Sakabe, T. Johzaki, H. Nagatomo, K. Mima, I. Uschmann, E. Foster, D.H.H. Hoffmann
Journal of Quantitative Spectroscopy & Radiative Transfer 81, 237 (2003)

The Frankfurt Funneling Experiment
J. Thibus, I. Mueller, N. Mueller, A. Schempp, H. Zimmermann
Proc. PAC 2003, IEEE03CH37423, Piscataway, Vol. 4, pp. 2823-2825 (2003)

High Current Ion Beam RF Acceleration and Perspectives for an Inertial Fusion Driver
U. Ratzinger, H. Liebermann, O. Meusel, H. Podlech, R. Tiede, W. Barth, W. Vinzenz
Laser and Particle Beams 21(4), 621 (2003)

Energy Loss of Ions in a Magnetized Plasma: Conformity between Linear Response and Binary Collision Treatments
H. B. Nersisyan, G. Zwicknagel, C. Toepffer,
Phys. Rev. E 67 (026411), 1 (2003)

Ion Stopping in a Magnetized Anisotropic Electron Plasma
B. Möllers, C. Toepffer, M. Walter, G. Zwicknagel
Nucl. Instr. Meth. in Phys. Res. B 205, 285 (2003)

Scaling Law for Recombination in Electron Coolers
C. Heerlein, G. Zwicknagel, C. Toepffer,
Nucl. Instr. Meth. in Phys. Res. B 205, 395 (2003)

Drag Force on Ions in Magnetized Electron Plasmas
B. Möllers, M. Walter, G. Zwicknagel, C. Carli, C. Toepffer
Nucl. Instr. Meth. in Phys. Res. B 207, 462 (2003)

Wave Packet Molecular Dynamics Simulations of Warm Dense Hydrogen
M. Knaup, P.-G. Reinhard, C. Toepffer, G. Zwicknagel
J. Phys. A: Math. Gen. 36, 6165 (2003)

Recombination Enhancement in Electron Coolers
C. Heerlein, C. Toepffer
Hyperfine Interactions 146/147 , 19 (2003)

Signatures of Chaos in Channeling Radiation Spectra
M. Weber, C. Toepffer, H. Genz, P. Hoffmann-Stascheck, A. Richter, C. Rangacharyulu, J.P.F. Sellshop
Proc. Symp. Channeling - Bent Crystals - Radiation Processes, 85 (2003)

Interpolation Formula for the Electrical Conductivity of Nonideal Plasmas
A. Esser, R. Redmer, G. Röpke
Contrib. Plasma Phys. 43, 33 (2003)

Scattering Processes and Electrical Conductivity of Partially Ionized Hydrogen Plasma
T.S. Ramazanov, K.Zh. Galiyev, D.N. Dzhumagulova, G. Röpke, R. Redmer
Contrib. Plasma Phys. 43, 39 (2003)

Electrical Conductivity in Dense Aluminum Fluid
S. Kuhlbrodt, R. Redmer
J. Phys. A: Math. Gen. 36, 6027 (2003)

Transport Properties of Partially Ionized Hydrogen Plasma
T.S. Ramazanov, K.Zh. Galiyev, D.N. Dzhumagulova, G. Röpke, R. Redmer
J. Phys. A: Math. Gen. 36, 6173 (2003)

Equation of State for Hydrogen in the Chemical Picture: Possible Application in Astrophysics
H. Juranek, V. Schwarz, R. Redmer
J. Phys. A: Math. Gen. 36, 6181 (2003)

Equation of State and Electrical Conductivity of Dense Fluid Hydrogen and Helium
R. Redmer, H. Juranek, S. Kuhlbrodt, V. Schwarz
Z. Phys. Chem. 217, 783 (2003)

Equation of State for Dense Plasmas
S. Kuhlbrodt, H. Juranek, V. Schwarz, R. Redmer
Contrib. Plasma Phys. 43, 342 (2003)

# CONFERENCE CONTRIBUTIONS

**Hamburg, Germany: Research Courses on New X-Ray Sciences at Hasylab/DESY, March 5-7, 2003**

R. Redmer
Warm Dense Matter in Astrophysics: Giant Planets

**Valencia, Spain: 11th International Workshop on the Physics of Non-ideal Plasmas (PNP11), March 20-25, 2003**

D.H.H. Hoffmann
High Intensity Particle and Laser Beams Interacting with Ionized Matter

D. Varentsov
Intense Heavy Ion Beams for Experimental Investigation of High Energy Density Matter

P. Mulser, M. Kanapathipillai
Giant Enhancement of Collisional Absorption in Extended Cluster Media

G. Zwicknagel, M. Knaup, P.-G. Reinhard and C. Toepffer
Wave Packet Molecular Dynamics Simulations of Warm Dense Hydrogen

G. Zwicknagel and T. Pschiwul
Dynamic Response of Two-Component Model Plasma

R. Redmer, H. Juranek, S. Kuhlbrodt, V. Schwarz
EOS and Conductivity in Warm Dense Matter

**Portland, USA, 2003 Particle Accelerator Conference, May 12-16, 2003**

J. Thibus, I. Mueller, N. Mueller, A. Schempp, H. Zimmermann
The Frankfurt Funneling Experiment

**Yamanashi, Japan: COOL 03, Int. Workshop on Beam Cooling and Related Topics, May 19-23, 2003**

C. Toepffer, B. Moellers, M. Walter, G. Zwicknagel
Cooling of Ions and Antiprotons with Magnetized Electrons

**Rostock, Germany: Workshop on the Dynamical Conductivity in Strongly Coupled Plasmas, June 13, 2003**

G. Zwicknagel, T. Pschiwul, B. Jakob
MD-simulations of the Conductivity of Model Plasmas

**Lyon, France: CECAM Workshop on Quantum Molecular Dynamics, June 30 – July 2, 2003**

R. Redmer
Behaviour of Dense Hydrogen

**St.-Petersburg, Russia: 30th EPS Conference on Controlled Fusion and Plasma Physics, July 7-11, 2003**

D. Varentsov
Experimental Investigation of High Energy Density Matter by Intense Heavy Ion Beams

O. Rosmej
X-ray Projectile and Target Radiation for Investigation of Ion Stopping Process

**Varenna, Italy, Int. Conference on Ultrashort High Energy Radiation and Matter, September 7-10, 2003**

M. Roth
X-Ray and Particle Diagnostics for Warm Dense Matter Research

**Monterey, Ca, USA, Int. Conf. on Inertial Science and Fusion Applications, September 8-12, 2003**

D.H.H. Hoffmann
High Energy Density Physics with Intense Ion and Laser Beams at GSI

**Parma, Italy: LXXXIX Congresso Nazionale della Societa` Italiana di Fisica, September 17-22, 2003**

P. Mulser, M. Kanapathipillai
Giant Enhancement of Collisional Absorption in Extended Cluster Media

**Copenhagen, Denmark: Workshop on Phase Transitions in Nuclear Collisions (PT03), October 9-10, 2003**

D. Varentsov
Intense Heavy Ion Beams as a Tool to Study Warm Dense Matter

**Greifswald, Germany: WE-Heraeus-Ferienschule zur Plasmaphysik, October 6-17, 2003**

R. Redmer
Stark korrelierte Plasmen
Plasmen in großen Planeten

**Gyeongju, Korea: IX International Conference on Accelerator and Large Physics Control System (ICALEPCS), October 13-17, 2003**

H. Brand, D. Beck, E. Gaul, W. Geithner, T. Kühl, K. Poppensieker, M. Roth, U. Thiemer
The PHELIX Control System Based on UML Design Level Programming in LabView

**Wien, Austria: IAEA Coordinated Research Projects, November 4–7, 2003**

D.H.H. Hoffmann
Basic Physics for Inertial Fusion Energy - Present and Future Prospects of High Energy Density in Matter Research at GSI

# DIPLOMA AND PHD-THESES

A. Kozyreva
Creation of High Energy Density in Matter with Heavy Ion Beams for Equation of State Studies
PhD-Thesis, TU Darmstadt, December 2003

M. Kanapathipillai
Erhöhte Laserabsorption in ausgedehnten Clustermedien
PhD-Thesis, TU Darmstadt, December 2003

M. Walter
Dielektrische lineare Antworttheorie magnetisierter Elektronenplasmen
PhD-Thesis, Universität Erlangen, February 2003

J. Marten
Einfluss von Mikrofeldern auf Strahlungsübergänge in Plasmen
PhD-Thesis, Universität Erlangen, May 2003

A. Kietzmann
Molekulardynamiksimulationen dichter Fluide
Diploma-Thesis, Universität Rostock, July 2003

V. Schwarz
Thermodynamik von Wasserstoff-Helium-Gemischen und Modellierung von großen Planeten
Diploma-Thesis, Universität Rostock, August 2003

S. Kuhlbrodt
Transporteigenschaften dichter Plasmen
PhD-Thesis, Universität Rostock, April 2003

## AUTHOR INDEX